

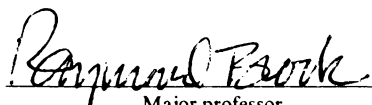
This is to certify that the
dissertation entitled
INCLUSION OF TEVATRON Z DATA INTO GLOBAL
NON-PERTURBATIVE QCD FITTING

presented by

Freddie J. Landry

has been accepted towards fulfillment
of the requirements for

Ph.D degree in Physics


Major professor

Date 5-1-2001



PLACE IN RETURN BOX to remove this checkout from your record.
TO AVOID FINES return on or before date due.
MAY BE RECALLED with earlier due date if requested.

DATE DUE	DATE DUE	DATE DUE

INCLUSION OF TEVATRON Z DATA INTO GLOBAL
NON-PERTURBATIVE QCD FITTING

By

Freddie J. Landry

A DISSERTATION

Submitted to
Michigan State University
in partial fulfillment of the requirements
for the degree of

DOCTOR OF PHILOSOPHY

Department of Physics and Astronomy

2001

ABSTRACT

INCLUSION OF TEVATRON Z DATA INTO GLOBAL NON-PERTURBATIVE QCD FITTING

By

Freddie J. Landry

Fits are performed to transverse momentum distributions of Drell-Yan data sets with non-perturbative functions in the Collins-Soper-Sterman (CSS) resummation formalism. Fits are made to various global sets of data containing results from both fixed target and collider experiments. Several functional forms in impact parameter space (b) of the non-perturbative function are also tested and compared. The best fit to the data is achieved with the form, $-g_1 b^2 - g_2 b^2 \ln\left(\frac{Q}{2Q_0}\right) - g_1 g_3 b^2 \ln(100x_a x_b)$ with the values for the parameters, $g_1 = 0.21^{+0.01}_{-0.01}$, $g_2 = 0.68^{+0.02}_{-0.02}$, $g_3 = -0.60^{+0.05}_{-0.04}$.

To my Mom and Dad

ACKNOWLEDGMENTS

There are many people I would like to thank for helping me throughout my graduate career. First, I would like to thank my advisor Chip for seeing me through this. He was helpful at finding solutions when I reached a roadblock and he was always willing to make time for me out of his busy life as chairman and physicist.

Thanks are also due to Dylan for letting me work with him on the final pieces of his analysis. He was also a good sounding board for our fitting work on more than one occasion.

The members of the fitting gang, C.-P., Chip, and Glenn are a good group of guys to work with and were always willing to help this greenhorn understand the theory, no matter how many times I asked.

From my DØ days, my trailermates Ashutosh, Ian, Eric, and Rich stand out for helping me learn the ropes there.

While on the TRGMON project, Philippe taught me all about triggering and how to really program.

Working with Sandor on the ZCD was always interesting and good for a few laughs. He showed me the part of high energy physics outside of the cubicle and away from the computer screen. In the process we got our hands dirty and played with a lot of interesting toys.

My companions at MSU, Remo, Mike, and Narlock, also get a thanks. I learned a lot about computers, beer, and presweetened cereal. And they learned to fear my shotguns.

Finally, I'd like to thank my family, or *la familia*, those living and those we won't forget, for the support and for the good times we've had.

TABLE OF CONTENTS

1 Theory	2
1.1 The Standard Model.....	2
1.2 The Drell-Yan Process.....	5
1.2.1 The Naive Process.....	5
1.2.2 The Lowest Order Nonzero	11
1.2.3 Higher Order Processes.....	18
1.2.4 Resummation Calculation.....	23
2 Fermilab and the DØ Detector.....	28
2.1 The Accelerator at Fermilab	28
2.2 The DØ Detector.....	31
2.2.1 Central Detectors.....	34
2.2.2 Calorimeter.....	38
2.2.3 Muon Detector	41
2.2.4 Triggering System.....	42
3 Refinement of DØ Z Data	44
3.1 Introduction.....	44
3.2 Studies With Fast Monte Carlo.....	44
3.2.1 Examination of Kinematic Variables.....	45

3.2.2	Studying Contributions to Smearing Resolution	50
3.3	Development of Fast Smearing Program	55
4	Non-Perturbative QCD Fits	60
4.1	Method of Fitting	60
4.2	Experiments Included in Fits	61
4.2.1	R209	62
4.2.2	CDF	63
4.2.3	E288	64
4.2.4	E605	64
4.3	Choice of Non-Perturbative Functions	65
4.4	Preliminary Fits	66
4.4.1	Duplication of Original LY Fitting	66
4.4.2	Simultaneous Fitting of All Parameters	68
4.5	Inclusion of Tevatron Run 1 Z Data	76
4.5.1	Gauss 1 Fit	77
4.5.2	LY and DWS Parameterization Fits	78
4.5.3	Gauss 3 Fit	78
4.6	Reintroduction of Drell-Yan Data	80
4.6.1	Fitting with Higher Mass E605	80
4.6.2	Bringing E288 Back into Fits	83
5	Conclusion	90
A	The Level 1 Trigger Monitor Program	93
A.1	Introduction	93
A.2	Method of Information Gathering and Computing	94

A.3	Implementing User Defined Integration Times	95
A.3.1	Method Of Calculating Over Larger Integration Times	95
A.3.2	User Interface	95
A.3.3	Behavior Under Special Conditions.....	95
A.4	Testing and Implementation of New TRGMON	96
B	The Z Calibration Detector.....	97
B.1	Introduction	97
B.2	Design of Detector.....	98
B.3	Acquisition and Selection of Data.....	100
B.4	Calibration Method.....	101
B.5	Results	106
C	Reprint of Preliminary Fits Paper	109
	Bibliography.....	121

LIST OF TABLES

Table 1.2: The quarks. The electric charge is given in units of the charge of the electron.	3
Table 1.3: The four known forces and their particle mediators.....	4
Table 4.1: Experiments included in global fits with some properties for the data used in the fits.....	62
Table 4.2: Fit C values using experimental data from R209, E288, and CDF Z.....	68
Table 4.3: Values for Fit D for three parameterizations.	69
Table 4.4: Data set of fit including extended E605 data set, Fit E.....	70
Table 4.5: Fit results for Fit E.....	70
Table 4.6: Fit for LY parameterization excluding E288, Fit F.....	71
Table 4.7: Fit for DWS parameterization excluding E288, Fit F.....	72
Table 4.8: Results for global fit including	76
Table 4.9: Fit H results.....	81
Table 4.10: Data set for Fit I.....	84
Table 4.11: Fit I results.	84
Table 4.12: Summary of fit results.....	87
Table B.1: Slopes from linear fits to Z_{fiber} vs Z_{ext} distributions of module pairs.	107
Table B.2: Intercepts from linear fits to Z_{fiber} vs Z_{ext} distributions of module pairs.	108



LIST OF FIGURES

Figure 1.1: Feynman diagram of virtual photon decaying into a lepton pair.....	6
Figure 1.2: A typical example of a quark antiquark collision producing a photon with a nonzero p_T through the radiation of a gluon	11
Figure 1.3: Feynman diagrams showing typical processes which produce p_T . The upper diagram is an initial radiation or “Annihilation” process and the lower diagram shows a “Compton” process.	13
Figure 1.4: Some higher order Feynman diagrams of Drell Yan production.	19
Figure 1.5: Decay of a photon into a quark antiquark pair with a subsequent gluon emission.....	20
Figure 2.1: The system of accelerators at Fermilab used to accelerate protons and antiprotons.....	29
Figure 2.2: The DØ Detector showing each subdetector.....	32
Figure 2.3: Representation of the DØ coordinate system.....	33
Figure 2.4: Cutaway view of the Central Detectors.....	34
Figure 2.5: The VTX chamber with the layout of its wires.	35
Figure 2.6: Cross section of a TRD chamber.....	36
Figure 2.7: Cutaway view of the CDC showing the wire placement in each cell.	37
Figure 2.8: The three modules which make up each of the Forward Drift Chambers.....	38
Figure 2.9: Cutaway view of the calorimeter.....	39
Figure 2.10: Representation of a typical calorimeter cell.	39
Figure 2.11: A portion of the calorimeter with pseudo-projective towers at different η	40



Figure 2.12: Schematic view of the different trigger levels.....	42
Figure 3.1: Dependence of the absolute resolution on the Z mass and rapidity.	47
Figure 3.2: Absolute resolution dependence on the Z p_T and the z of the interaction vertex.....	48
Figure 3.3: Absolute resolution dependence on the energy and pseudorapidity of the highest p_T electron	49
Figure 3.4: Absolute resolution dependence on the p_T of the highest p_T electron.....	50
Figure 3.5: Effect of EM calorimeter energy and position resolutions on the Z p_T absolute resolution. The absolute resolution is plotted as a function of Z p_T	53
Figure 3.6: Z p_T absolute resolution dependence on track resolution and the underlying event contribution. The absolute resolution is plotted as a function of Z p_T	54
Figure 3.7: Effect of z vertex resolution on Z p_T absolute resolution. The absolute resolution is plotted as a function of Z p_T	55
Figure 3.8: Special input distribution to CMS.	57
Figure 3.9: Fit parameters plotted versus p_T	58
Figure 3.10: CMS smeared and SMEAR_PT smeared distributions.....	59
Figure 4.1: Contour of χ^2+1 for 2 parameter fit, Fit F	73
Figure 4.2: Contours for determining uncertainties for Fit F with the LY parameterization. These plots were made with fixed g_3 , g_2 , and g_1 respectively at their values at the minimum.....	74
Figure 4.3: Plots of LY and DWS parameterization curves superimposed with data. Note that the NORM values given here are applied to the theoretical curves and are therefore reciprocals of the values given in Table 4.6 and Table 4.7	75
Figure 4.4: Gauss 1 fit distribution for E605.	77

Figure 4.5: LY function and 2 parameter Fit G compared to each other. Note that the NORM values given here are applied to the theoretical curves and are therefore reciprocals of the values given in Table 4.8.	79
Figure 4.6: Plots of Fit H results compared to Data.....	82
Figure 4.7: Fit I Plots compared to Data.....	85
Figure 4.8: Fit I Plot of E288 compared to fit curves.	86
Figure 5.1: Uncertainty contour and two dimensional projections for the Fit I result with the Gauss 1 parameterization.	91
Figure B.1: A Muon Detector track extrapolated to the CDC does not align with the z positions of the delay line hits.....	98
Figure B.2: Diagram of a ZCD module and two connecting modules.	99
Figure B.3: A representation of the placement of one of the ZCD modules over a CDC sector.	100
Figure B.4: Placement of the ZCD module pairs in relation to the CDC sectors. The numbering of the module pairs is shown as well as the CDC sectors covered by the ZCD.	102
Figure B.5: Extrapolation of CDC track out to the ZCD module to obtain Z_{ext}	103
Figure B.6: Typical Fits to ΔZ for four fibers.	104
Figure B.7: Examples of linear fits to Z_{fiber} vs. Z_{ext} for modules 1-4.	105

INTRODUCTION

This analysis is centered on achieving the best prediction of transverse momentum distributions of Drell-Yan (DY) type events, particularly in the low p_T region ($p_T \ll Q$). Here, DY type events are defined as the production of W , Z , or photons resulting directly from hadron-hadron collisions. The theoretical prediction is made through the use of a non-perturbative QCD formalism, which includes a parameterized function. The parameters for this function are set by a fit to data. This analysis seeks to improve the prediction of DY type distributions by both increasing the data available for fitting through supplemental analysis of Tevatron Z data, and by performing global fits.

There are several benefits to finding which non-perturbative function or functions provide a good fit to p_T distributions of DY type events. Finding such a match will verify the concept of universality, the idea that one non-perturbative function can give an accurate prediction of the cross section distribution for the production of any mediator boson, at any center of mass energy. A benefit to producing more accurate theoretical W and $Z p_T$ distributions is increasing the precision of the W mass measurement. Finally, gaining a better measurement of the low p_T region will provide a comparison tool for any future theory which seeks to predict non-perturbative QCD.

The discussion begins in Chapter 1 with an overview of the current status of particle physics. Then the history of the calculation of Drell-Yan type events will be presented with some detail. Chapter 2 discusses the Fermilab accelerator which was used by several experiments included in the fitting. Also included is a description of the DØ detector which produced the $Z p_T$ data analyzed in Chapter 3. A description of the numerous fits to global data sets and their results are given in Chapter 4. The conclusion is presented in Chapter 5.



Chapter 1

Theory

1.1 The Standard Model

Elementary particle physics deals with the fundamental particles and forces which make up everything in the universe. Some properties of these particles are listed in tables on the following pages and were obtained from the Particle Data Group [1]. All forms of matter are made of two classes of spin $\frac{1}{2}$ particles, leptons and quarks. These two classes of particles are listed in Table 1.1 and Table 1.2.

In addition to the above classes of particles there are the mediators of the four fundamental forces. Leptons and quarks interact with each other through the exchange of these mediator particles, which is the mechanism by which particles exert forces on each other. All of these mediators are spin 1 except for the graviton, which is expected to have spin 2. Table 1.3 lists the forces and their mediator bosons.



Particle	Mass (MeV/c ²)	Charge (e)
electron, e	0.511	-1
electron neutrino, ν_e	0.0	0
muon, μ	105.7	-1
muon neutrino, ν_μ	0.0	0
tau, τ	1777.1	-1
tau neutrino, ν_τ	0.0	0

Table 1.1: The leptons. The electric charge is given in units of the charge of the electron.

Particle	Mass (MeV/c ²)	Charge (e)
down, d	3-9	-1/3
up, u	1.5-5	+2/3
strange, s	60-170	-1/3
charm, c	(1.1-1.4)x10 ³	+2/3
bottom, b	(4.1-4.4)x10 ³	-1/3
top, t	174.3x10 ³	+2/3

Table 1.2: The quarks. The electric charge is given in units of the charge of the electron.



Force	Particle	Mass (GeV/c²)
Strong	gluon	0
Electromagnetic	photon	$< 2 \times 10^{-25}$
Weak	W,Z	80.33,91.187
Gravity	graviton	0?

Table 1.3: The four known forces and their particle mediators.

With the exception of gravity, quantum theories have been developed since the early part of the 20th century which describe how each of these forces act on elementary particles. These theories taken together comprise the Standard Model, which to the best of our present knowledge, describes most of the behavior of the particles in their interactions through three of the four forces. Quantum Chromodynamics, or QCD, is the theory which describes processes involving the strong force. Quantum Electrodynamics, QED, describes interactions involving the electromagnetic force. The formalism of Glashow, Weinberg, and Salam [2] combines the electromagnetic and weak processes as different aspects of the same force, the electroweak force.

The Standard Model describes many of the processes observed in high energy physics. However, there are some fundamental questions which it leaves unanswered. For example it doesn't explain why the elementary particles have the particular mass values that they do. It also doesn't provide a quantum theory for gravity. There is also reason to believe that at high enough energies that all four forces are unified into one force, an idea bolstered by the verification of electroweak theory [3][4]. This hypothesis however, is outside the predictive power of the Standard Model. Finally, as will be shown in the next section, there are also kinematic regions in which the Standard Model can't give us a complete calculation of particle dynamics.



1.2 The Drell-Yan Process

In high energy experiments involving collisions between quarks and antiquarks, the final state sometimes includes a photon, W , or Z in a process called a Drell-Yan process. This section, based on [5], [6], and [7], will step through the various techniques used to calculate cross sections for such processes. Although the derivations are shown for only the photon, the calculations are essentially the same for the W and Z with a change of some constants.

1.2.1 The Naive Process

As a first step, the cross section calculation will be shown for what is known as the naive Drell-Yan process for the production of virtual photons. The cross section for such a process was first calculated by Drell and Yan [8]. It's called "naive" because the assumption is made that the initial partons, (the quarks, antiquarks, and gluons which constitute hadrons), involved in the reaction have no momentum transverse to the momentum vectors of the hadrons in the center of mass frame of the initial hadrons. This of course means that the photon would then have no transverse momentum in this frame either. This process was recognized experimentally when the photon decayed into lepton pairs [9]. A Feynman diagram for such a process is shown in Figure 1.1.

Before calculating the cross section, it is helpful to introduce some commonly used kinematic variables. Here, the values for these variables are defined in the center of mass frame of the hadrons with the z axis along the hadron momentum vectors. The four vector momenta of the hadrons are written below where the masses have been neglected because the virtual photon's mass is much larger:

$$\begin{aligned} P_A^\mu &= (P, \vec{0}, P) \\ P_B^\mu &= (P, \vec{0}, -P). \end{aligned} \tag{1.1}$$

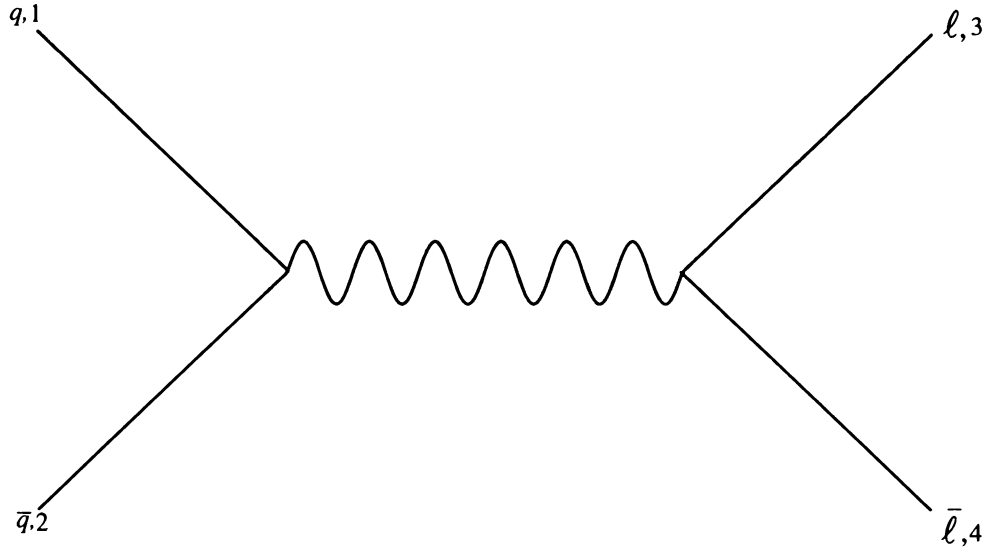


Figure 1.1: Feynman diagram of virtual photon decaying into a lepton pair.

The four vector momenta for the initial partons have a similar form:

$$p_a^\mu = (p_a^z, \vec{0}, p_a^z)$$

$$p_b^\mu = (p_b^z, \vec{0}, -p_b^z).$$

The parton momenta can be expressed in terms of their parent hadrons also:

$$p_a^\mu = x_a P_A^\mu$$

$$p_b^\mu = x_b P_B^\mu.$$

The x variables represent for each parton its fraction of the parent hadron's momentum.

Therefore, x can range in value from 0 to 1. The photon's momentum four vector is

$$P_V^\mu = (E_V, \vec{0}, P_V^z).$$



The difference in the longitudinal momenta of the partons is an important quantity in this process and leads to the definition of the Feynman x , x_F :

$$p_L = p_a^z - p_b^z = P(x_a - x_b)$$

$$x_F \equiv \frac{p_L}{P} = x_a - x_b.$$

In addition there are three invariants referred to as the Mandelstam variables. For the hadron level process they are

$$s \equiv (P_A^\mu + P_B^\mu)^2 = 4P^2$$

$$t \equiv (P_V^\mu - P_A^\mu)^2 = Q^2 - x_b s$$

$$u \equiv (P_V^\mu - P_B^\mu)^2 = Q^2 - x_a s.$$

Here Q is the photon mass. The corresponding variables at the parton level are given by

$$\hat{s} \equiv (p_a^\mu + p_b^\mu)^2 = x_a x_b s$$

$$\hat{t} \equiv (P_V^\mu - p_a^\mu)^2 = Q^2 - x_a x_b s$$

$$\hat{u} \equiv (P_V^\mu - p_b^\mu)^2 = Q^2 - x_a x_b s.$$

Another often used kinematic variable is defined below,

$$\tau \equiv \frac{Q^2}{s}.$$

Using the relation, $Q^2 = x_a x_b s$, it becomes

$$\tau = x_a x_b.$$

Rapidity, defined below, is also an important invariant:

$$y \equiv \frac{1}{2} \ln \frac{E + p_z}{E - p_z}. \quad (1.2)$$

For the photon in this process, the rapidity is given by

$$y = \frac{1}{2} \ln \left(\frac{x_a}{x_b} \right). \quad (1.3)$$

When Drell and Yan calculated the cross section, they considered the calculation in two parts as given by:

$$\sigma(p\bar{p} \rightarrow \gamma^* \rightarrow \ell^+ \ell^-) = \iint dx_a dx_b f(x_a) f(x_b) \hat{\sigma}(q\bar{q} \rightarrow \gamma^* \rightarrow \ell^+ \ell^-). \quad (1.4)$$

One part, the integration of the $f(x)$ functions, takes into account that the partons are constituents of hadrons. The functions, $f(x)$, are called parton distribution functions (PDF). They give the probability for a parton to have the momentum fraction x . The integration is over all possible values of the x 's. The other part, the $\hat{\sigma}$ factor, is the cross section for the Drell-Yan process at the parton level. This elementary process is calculated using the following equation where T is the matrix element calculated using the Feynman calculus:

$$d\hat{\sigma} = \frac{|T|^2}{(\text{initial flux})} \cdot (\text{phase space of final states}). \quad (1.5)$$

It is usually of more interest to calculate and observe differential cross sections, such as $\frac{d\sigma}{d\Omega_3}$, where Ω_3 is the solid angle of the lepton labeled 3 in Figure 1.1. In order to calculate $\frac{d\sigma}{d\Omega_3}$, the same calculation of Equation 1.5 is used and then the kinematic quantities for all final state particles are integrated over with the exception of Ω_3 .

The phase space for the final state particles are:

$$\rho(\vec{p}_3, \vec{p}_4) = \frac{(2\pi)^4}{(2\pi)^6} \delta^4(p_1 + p_2 - p_3 - p_4) \frac{d^3 p_3}{2E_3} \frac{d^3 p_4}{2E_4} \quad (1.6)$$



$$= \frac{1}{(2\pi)^2} \frac{p_3^2 dp_3 d\Omega_3}{4E_3 E_4} \delta^3(\vec{p}_1 + \vec{p}_2 - \vec{p}_3 - \vec{p}_4) \delta(E_1 + E_2 - E_3 - E_4) d^3 p_4.$$

Next, the phase space is integrated over all kinematic quantities except Ω_3 . The integration over $d^3 p_4$ leads to the constraint, $\vec{p}_4 = \vec{p}_1 + \vec{p}_2 - \vec{p}_3$, and therefore $E_4 = \sqrt{(\vec{p}_1 + \vec{p}_2 - \vec{p}_3)^2 + m_4^2}$. The phase space factor is now

$$\rho(\vec{p}_3) = \frac{1}{(2\pi)^2} \frac{p_3^2 dp_3 d\Omega_3}{4E_3 E_4} \delta(E_1 + E_2 - E_3 - E_4).$$

Integrating this over dp_3 gives the density of states in terms of the initial total momentum and energy, \vec{p}_i and E_i respectively, as

$$\rho(\Omega_3) = \frac{1}{16\pi^2} \left. \frac{p_3^3 d\Omega_3}{|E_i p_3^2 - \vec{p}_i \cdot \vec{p}_3 E_3|} \right|_{E_3 = E_i - E_4}.$$

In the center of mass frame, $\vec{p}_i = 0$, and the phase space factor simplifies to

$$\frac{1}{16\pi^2} \frac{p_3}{E_i} d\Omega_3. \quad (1.7)$$

The matrix element factor for $d\hat{\sigma}$ is given by Equation 1.8. e_q is the electric charge of the quark, e is the charge of the electron and m_ℓ is the mass of each final state lepton.

$$|T|^2 = \frac{e_q^2 e^4}{4(p_1^\mu + p_2^\mu)^4} \cdot 32 \left[(p_1 \cdot p_3)(p_2 \cdot p_4) + (p_1 \cdot p_4)(p_2 \cdot p_3) + m_\ell^2 (p_1 \cdot p_2) \right] \quad (1.8)$$

This equation is greatly simplified in the center of mass frame and when conservation of energy and momentum are taken into account. Under these requirements the following relations hold true and Equation 1.9 gives the simplified matrix element:

$$|T|^2 = \frac{e_q^2 e^4}{4(p_1 + p_2)^4} \cdot 32 \left[2(E^2 E'^2 + p^2 p'^2 \cos^2 \theta + m_i^2 E^2) \right]. \quad (1.9)$$

$$\begin{aligned} \vec{p} &\equiv \vec{p}_1 = -\vec{p}_2 \\ \vec{p}' &\equiv \vec{p}_3 = -\vec{p}_4 \\ E &\equiv E_1 = E_2 \quad (\text{since } m_1 = m_2) \\ E' &\equiv E_3 = E_4 \quad (\text{since } m_3 = m_4) \end{aligned}$$

The initial flux factor from Equation 1.5 is $4\sqrt{(p_1 \cdot p_2)^2 - m_1^2 m_2^2}$, which in the center of mass frame simplifies to $p_1 \cdot p_2 = E^2 + p^2$. Also, in the approximation that the masses of the initial quarks can be neglected relative to the energy, E , the flux factor simplifies to $8E^2$.

Combining all three factors and simplifying leads to the following:

$$\frac{d\hat{\sigma}}{d\Omega_3} = \frac{e_q^2 e^4}{64\pi^2 \hat{s}} \frac{p_3}{E_3} \left[1 + \cos^2 \theta + \left(1 - \left(\frac{p_3}{E_3} \right)^2 \right) \sin^2 \theta \right]. \quad (1.10)$$

Where \hat{s} is defined as E_i^2 . Using the relation, $m_3^2 = E_3^2 - p_3^2$, the differential cross section can be written in terms of the mass:

$$\frac{d\hat{\sigma}}{d\Omega_3} = \frac{e_q^2 e^4}{64\pi^2 \hat{s}} \sqrt{1 - \frac{m_3^2}{E_3^2}} \left[1 + \cos^2 \theta + \left(\frac{m_3}{E_3} \right)^2 \sin^2 \theta \right]. \quad (1.11)$$

In the limit where the mass of particle 3 is much smaller than its energy, the cross section simplifies to:

$$\frac{d\hat{\sigma}}{d\Omega_3} = \frac{e_q^2 e^4}{64\pi^2 \hat{s}} [1 + \cos^2 \theta]. \quad (1.12)$$

The term in brackets is characteristic of processes involving spin $\frac{1}{2}$ initial and final state particles mediated by a spin 1 particle.

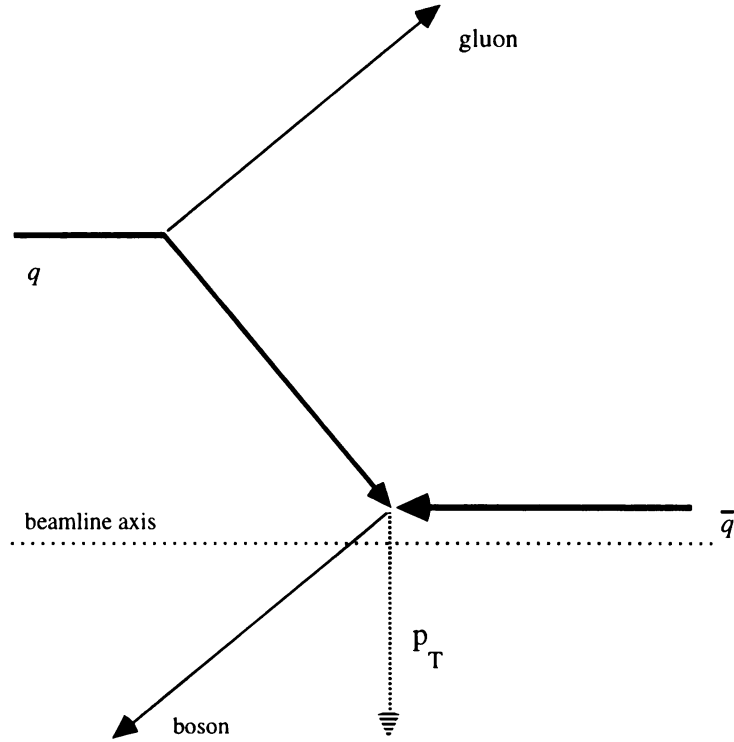


Figure 1.2: A typical example of a quark antiquark collision producing a photon with a nonzero p_T through the radiation of a gluon.

1.2.2 The Lowest Order Nonzero p_T Process

With the initial partons travelling along the beamline in opposite directions it would be expected that the resulting photon would not have any p_T , that is, a momentum transverse to the beamline. But measurements show a significant number with a nonzero p_T . This is due to gluon radiation from the initial partons, which is not taken into account by the process shown in Figure 1.1. The differential p_T cross section for this process can be calculated perturbatively as a series in increasing powers of α_s . Here, the differential cross section will be derived to order α_s , or in other words to first order in the series.

Figure 1.2 gives an example of a process in which p_T is generated by the emission of a single gluon resulting in the photon having an equal, but opposite p_T to the gluon. This process is an example of one of the lowest order processes which produce photons

with transverse momenta. The example of Figure 1.2, often called the “Annihilation” process and another such process of the same order, the “Compton” process, are shown as Feynman diagrams in Figure 1.3. In calculating cross sections to first order in α_s , both types of processes must be included.

For the first order processes, it is interesting to examine the kinematic variables and note the differences from the naive process. In order to simplify calculations, the center of mass frame of the colliding hadrons is used. The four momenta of the initial hadrons and partons remain identical to the naive Drell-Yan process. The general four momentum for any of the final state particles can be written as

$$k_i^\mu = (E_i, \vec{k}_{Ti}, k_{\parallel i}).$$

Here, the momentum vector is represented by a component transverse to the initial hadrons, \vec{k}_{Ti} , and parallel to them, $k_{\parallel i}$. The Mandelstam invariants with respect to any of the final state particles can be calculated in terms of the four momenta. The s invariant is straightforward and is the same value as in the naive model.

$$s = 4P^2$$

The other variables are calculated below:

$$\begin{aligned} t &= (k^\mu - P_A^\mu)^2 = m^2 - 2k \cdot P_A = m^2 - 2P(E - k_{\parallel}) \\ u &= (k^\mu - P_B^\mu)^2 = m^2 - 2k \cdot P_B = m^2 - 2P(E + k_{\parallel}). \end{aligned}$$

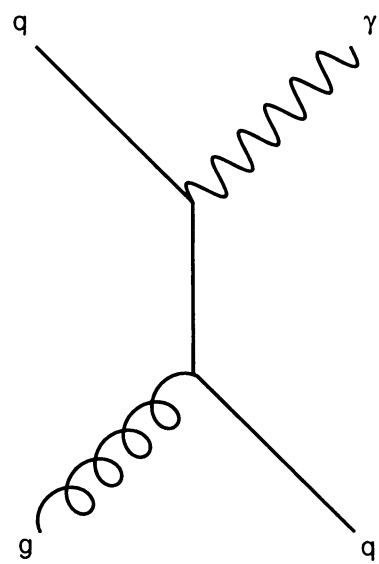
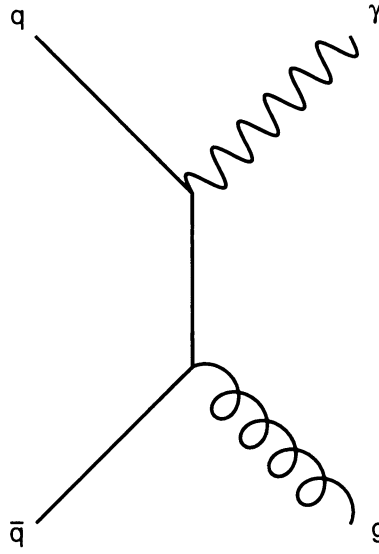


Figure 1.3: Feynman diagrams showing typical processes which produce p_T . The upper diagram is an initial radiation or "Annihilation" process and the lower diagram shows a "Compton" process.

The equations for t and u can be subtracted from each other to solve for k_{\parallel} ,

$$k_{\parallel} = \left[\left(\frac{m^2 - u}{4P^2} \right) - \left(\frac{m^2 - t}{4P^2} \right) \right] P = (x_1 - x_2)P. \quad (1.13)$$

Where x_1 and x_2 have been defined as

$$x_1 = \frac{m^2 - u}{4P^2} = \frac{E + k_{\parallel}}{\sqrt{s}}$$

$$x_2 = \frac{m^2 - t}{4P^2} = \frac{E - k_{\parallel}}{\sqrt{s}}.$$

Notice that instead of the longitudinal momentum of the photon being represented by $(x_a - x_b)P$ as in the naive picture, it is now equal to Equation 1.13. There are other relations that bear the same form as their naive counterparts, yet reveal the differences between the naive model and first order p_T process. For instance, a variable called the transverse mass is defined by

$$m_T^2 \equiv x_1 x_2 s = m^2 + k_T^2,$$

whereas $m^2 = x_a x_b s$ in the naive model. Also, instead of rapidity following the relation of Equation 1.3, the rapidity is now

$$y = \frac{1}{2} \ln \left(\frac{x_1}{x_2} \right).$$

A commonly used quantity defined below is x_T ,

$$x_T = \frac{2k_T}{\sqrt{s}}.$$

Finally, from the relation, $\hat{s} + \hat{t} + \hat{u} = Q^2$, the x variables can be related to each other by

$$x_a = \frac{x_b x_1 - \tau}{x_b - x_2} \quad x_b = \frac{x_a x_2 - \tau}{x_a - x_1}.$$

With these kinematic variables and the relations between them, the cross section can now be calculated.

The differential cross section for each of the two processes is given by the following equation:

$$\frac{d^3\sigma}{d\tau dp_T^2 dy} = \sum_{i,j} \int dx_a dx_b f(x_a) f(x_b) \frac{d^3\hat{\sigma}(ij \rightarrow \gamma^* X \rightarrow \ell^+ \ell^- X)}{d\tau dp_T^2 dy}. \quad (1.14)$$

Here, $\frac{d^3\hat{\sigma}}{d\tau dp_T^2 dy}$ is the differential cross section for the production of a lepton pair mediated by a virtual photon, with partons of flavors i and j . The sum is over the different quark flavors. x and $f(x)$ are the same momentum fractions and PDF's used in Equation 1.4. The cross sections for the Compton and Annihilation processes will be calculated separately and then added together to get the total first order differential cross section.

Labeling the Compton process $ab \rightarrow Vd$, the cross section for the intrinsic process can be written as

$$d\hat{\sigma} = \frac{\sum_i \sum_f |T|^2 d\rho(\vec{p}_V, \vec{p}_d)}{4E_a \sqrt{s}}$$

where d is the final state quark and V is the photon. The phase space for this reaction is

$$d\rho = (2\pi)^4 \delta^4(p_a + p_b - p_V - p_d) \frac{d^3 p_V}{(2\pi)^3 2E_V} \frac{d^3 p_d}{(2\pi)^3 2E_d}.$$

Since it is the distribution of V that is of interest and not quark d , the cross section can be integrated over all values of p_d to give

$$d\sigma = \iint dx_a dx_b f(x_a) f(x_b) \frac{\sum_i \sum_f |T|^2}{64\pi^2 E_a E_b} \delta(p_d^2) \frac{d^3 p_V}{E_V} \bigg|_{\mathbf{p}_d = \mathbf{p}_a + \mathbf{p}_b - \mathbf{p}_V} . \quad (1.15)$$

The remaining delta function can be handled by first transforming it into a function of x_a and x_b . From the relation

$$p_d^2 = \hat{s} + \hat{t} + \hat{u} - Q^2 = (x_a x_b - x_a x_1 - x_b x_2 - \tau)s, \quad (1.16)$$

the delta function can now be expressed as $\delta(f(x_a))$ which allows for the following property to be used:

$$\int \delta(f(x)) dx = \sum_i \delta(x - x_i) \left| \frac{\partial f}{\partial x} \right|_{x=x_i}^{-1} \text{ where } f(x_i) = 0.$$

Now Equation 1.15 can be written in the following way:

$$E_V \frac{d\hat{\sigma}}{d^3 p_V} = \iint dx_a dx_b f(x_a) f(x_b) \frac{\sum_i \sum_f |T|^2 \delta(x_a - x_a^R)}{64\pi^2 E_a E_b s(x_b - x_1)}.$$

Where x_a^R is the root of Equation 1.16. Using the general cross section for two to two body interactions,

$$\frac{d\hat{\sigma}}{d\hat{t}} = \frac{1}{16\pi\hat{s}^2} |T|^2,$$

and the relation

$$E \frac{d^3 \sigma}{dp^3} = \frac{1}{2\pi p_T} \frac{d\sigma}{dp_T dy} = \frac{1}{\pi} \frac{d\sigma}{dp_T^2 dy}, \quad (1.17)$$

and integrating over x_a yields

$$\frac{d\hat{\sigma}}{dQ^2 dp_T^2 dy} = \frac{1}{\pi} \int dx_b f(x_a^R) f(x_b) \frac{x_a^R x_b}{(x_b - x_1)} \frac{d\hat{\sigma}}{d\hat{t} dQ^2}.$$

$\frac{d\hat{\sigma}}{d\hat{t}}$ can be calculated by using the result from the well-known original Compton scattering [7], with the substitution of a photon with mass as a final particle

$$(\gamma + e \rightarrow \gamma^* + e),$$

$$\frac{d\hat{\sigma}}{d\hat{t}} = \frac{2\pi\alpha^2}{\hat{s}^2} \left[-\frac{\hat{t}}{\hat{s}} - \frac{\hat{s}}{\hat{t}} - \frac{2\hat{u}Q^2}{\hat{s}\hat{t}} \right].$$

Converting this expression to the $q + g \rightarrow \gamma^* + q \rightarrow \ell^+ \ell^- + q$ reaction gives

$$\frac{d\hat{\sigma}_C}{d\hat{t} dQ^2} = \frac{\alpha^2 \alpha_s e_q^2}{9Q^2 \hat{s}^2} \left[\frac{-\hat{t}^2 - \hat{s}^2 + 2\hat{u}Q^2}{\hat{s}\hat{t}} \right].$$

This result can also be used in obtaining the same differential cross section for the Annihilation process using crossing symmetry,

$$\frac{d\hat{\sigma}_A}{d\hat{t} dQ^2} = \frac{8}{27} \frac{\alpha^3 \alpha_s e_q^2}{Q^2 \hat{s}^2} \left[\frac{\hat{t}^2 + \hat{u}^2 + 2\hat{s}Q^2}{\hat{u}\hat{t}} \right].$$

These two results can then be inserted into the expression for the total cross section,

$$\begin{aligned} \frac{d\sigma(AB \rightarrow \ell^+ \ell^- X)}{dQ^2 dp_T^2 dy} &= \frac{1}{\pi} \int dx_b f(x_a^R) f(x_b) \frac{x_a^R x_b}{(x_b - x_1)} \frac{d\hat{\sigma}_A}{d\hat{t} dQ^2} \\ &+ \frac{1}{\pi} \int dx_b \left[f_{q/A}(x_a^R) f_{g/B}(x_b) + f_{g/A}(x_a^R) f_{q/B}(x_b) \right] \frac{x_a^R x_b}{(x_b - x_1)} \frac{d\hat{\sigma}_C}{d\hat{t} dQ^2}. \end{aligned}$$

The behavior of this cross section at low p_T can be studied by changing the cross section expressions through the relation

$$\frac{\hat{u}\hat{t}}{\hat{s}} = p_T^2.$$

For instance, the Annihilation result becomes

$$\frac{d\sigma_A}{dQ^2 dp_T^2 dy} = \frac{8}{27} \frac{\alpha^2 \alpha_s e_q^2}{\pi Q^2} \frac{1}{p_T^2} \int dx_b f(x_a^R) f(x_b) \frac{1}{(x_b - x_1)} \left[1 + \frac{\tau^2}{(x_a^R x_b)^2} - \frac{x_T^2}{2x_a^R x_b} \right],$$

and taking this result in the limit $p_T^2 \rightarrow 0$ gives

$$\frac{d\sigma}{dQ^2 dp_T^2 dy} \propto \frac{4\alpha_s}{3\pi} \frac{1}{p_T^2} \ln\left(\frac{Q^2}{p_T^2}\right). \quad (1.18)$$

So this result diverges in the limit that p_T becomes zero, which is obviously an unphysical result.

1.2.3 Higher Order Processes

As stated earlier, the above calculation takes into account only the most simple of processes resulting in p_T for the photon. In general, much more complicated processes, multiple gluon emission for example, can occur in vector boson production. Figure 1.4 shows two examples of higher order processes.

The perturbative calculation for the cross section of the multiple gluon emission process can be done by first looking at the decay, $\gamma^* \rightarrow q\bar{q}g$, Figure 1.5. Notice that this process is related to both the Annihilation and Compton processes through crossing symmetry.



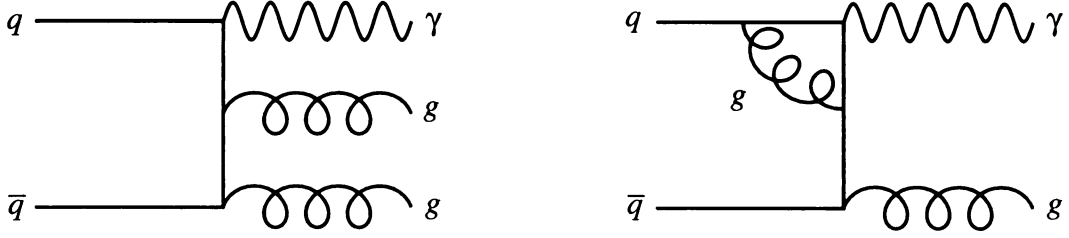


Figure 1.4: Some higher order Feynman diagrams of Drell Yan production.

The photon decay cross section can be analyzed by first defining the function S as the probability that the quark is diverted by an angle less than θ from its initial direction due to the gluon emission. T is then defined as the probability that the quark is diverted by an angle greater than θ . S and T are then related by the following equation:

$$S + T = 1. \quad (1.19)$$

It is convenient to define some kinematic variables for the process before performing any calculations. Let x_1 and x_2 be the fractions of the photon's four momentum carried by the antiquark and quark respectively. Note that x_2 is the momentum fraction carried by the quark after it has emitted the gluon. The momentum fraction carried by the gluon, x_3 , is then equal to $1 - x_1 - x_2$. The quantity z is the ratio of the quark's energy before and after the gluon emission and the variable j is just the ratio of the invariant mass of the quark and the gluon to the photon mass:

$$z = \frac{E_a}{E_b}$$

$$j = \frac{(p_2^\mu + p_3^\mu)^2}{Q^2} = \frac{Q^2(1 - 2x_1)}{Q^2} = 1 - 2x_1.$$

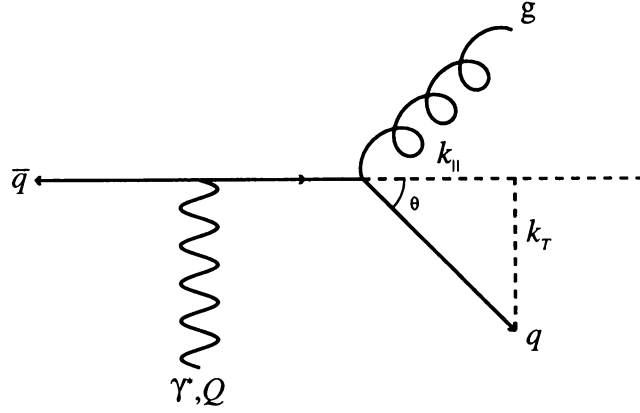


Figure 1.5: Decay of a photon into a quark antiquark pair with a subsequent gluon emission.

If θ is taken to be small, then the following approximation can be made:

$$\theta \cong \tan \theta = \frac{k_T}{k_{\parallel}} \cong \frac{2k_T}{Q}. \quad (1.20)$$

k_T represents the quark's transverse momentum needed to achieve the angle θ and k_{\parallel} is the momentum in the direction of the initial quark's trajectory. The approximation, $k_{\parallel} \cong \frac{Q}{2}$, is only good if the gluon's momentum component in that direction is small and if k_T is small. The small angle approximation used above also requires that k_T be small.

T can be related to the cross section as a differential of the quark's p_T ,

$$T(k_T^2) = \int_{k_T^2}^{\frac{Q^2}{4}} \frac{1}{\sigma_0} \frac{d\sigma}{dk_T'^2} dk_T'^2 \quad \text{where } \sigma_0 = 3\alpha e_q^2 Q.$$

This equation can be solved for the differential cross section by differentiating by k_T^2 :

$$\frac{1}{\sigma_0} \frac{d\sigma}{dk_T^2} = -\frac{dT}{dk_T^2} = \frac{dS}{dk_T^2}. \quad (1.21)$$

So by calculating T and differentiating as above, the p_T differential cross section can be obtained.



T can be calculated using the double differential cross section for the $\gamma^* \rightarrow q\bar{q}g$ process. This is given by

$$\frac{d\sigma}{dx_1 dx_2} = 3\alpha e_q^2 Q \frac{32\alpha_s}{3\pi} \frac{x_1^2 + x_2^2}{(1-2x_1)(1-2x_2)}.$$

Or rewriting this in terms of the kinematic variables relating to the quark, j and z , the cross section becomes

$$\frac{d\sigma}{dj dz} = \frac{4Q^3 \alpha e_q^2 \alpha_s}{\pi} \left[\frac{j}{1-z} + \frac{1+z^2}{j(1-z)} + \frac{16}{1-z} \right].$$

From the restrictions imposed by the approximation in Equation 1.20, the gluon energy must be small and therefore $z \sim 1$. By definition, j is ≤ 1 and is therefore also small. The middle term in the cross section then should dominate and the cross section then can be approximated by

$$\frac{1}{\sigma_0} \frac{d\sigma}{dj dz}_{LPA} = \frac{2\alpha_s}{3\pi} \frac{1+z^2}{j(1-z)}.$$

This is called the Leading Pole Approximation (LPA). Equation 1.20 can be rewritten as

$$k_T^2 = \frac{\theta^2 Q^2}{4}.$$

Defining a new variable, \bar{z} to be $1-z$, and using the relationship

$$\frac{p_T^2}{Q^2} = z(1-z)j$$

for the p_T of the quark, enables one to put limits on the allowable values for j and \bar{z} in the integration of T :

$$\frac{p_T^2}{Q^2} = z(1-z)j \equiv \bar{z}j > \frac{\theta^2}{4}.$$

T can now be written as

$$T(\theta)_{LPA} = \frac{2\alpha_s}{3\pi} \iint \frac{1+z^2}{(1-z)j} dzdj = \frac{2\alpha_s}{3\pi} \int_{\frac{\theta^2}{4}}^1 \frac{dj}{j} \int_{\frac{\theta^2}{4j}}^1 \frac{2d\bar{z}}{\bar{z}}.$$

The solution for T is then

$$T_1(\theta) = -\frac{4\alpha_s}{3\pi} \int_{\frac{\theta^2}{4}}^1 \frac{dj}{j} \ln\left(\frac{\theta^2}{4j}\right)$$

$$T_1(\theta)_{LDLA} = \frac{2\alpha_s}{3\pi} \ln^2\left(\frac{\theta^2}{4}\right).$$

The “LDLA” subscript refers to the fact that this result is the “Leading Double Log Approximation.” The solution for S then follows from Equation 1.19:

$$S_1(\theta)_{LDLA} = 1 - \frac{2\alpha_s}{3\pi} \ln^2\left(\frac{\theta^2}{4}\right).$$

Now, either S or T can be inserted into Equation 1.21 to obtain the differential cross section,

$$\frac{1}{\sigma_0} \frac{d\sigma}{dk_T^2} = \frac{4\alpha_s}{3\pi} \frac{1}{k_T^2} \ln\left(\frac{Q^2}{k_T^2}\right).$$

Note that it matches the form of the first order Drell-Yan calculation for the triple differential cross section of the photon in Equation 1.18. The “1” subscript has been added to S and T to point out the fact that the calculation is for a single gluon emission and therefore the cross section calculation is only to first order in α_s .

This cross section can be generalized to include multiple gluon emissions. Let S_n be the probability of the quark being diverted by n independent gluon emissions by an angle less than θ from its initial trajectory. The “initial trajectory” in this instance means the quark’s trajectory prior to any gluon emissions. Then S_n is given by

$$S_n = \frac{1}{n!} \left[-\frac{2\alpha_s}{3\pi} \ln^2 \left(\frac{k_T^2}{Q^2} \right) \right]^n.$$

This can be summed over n to take into account all possible number of emissions to give

$$S = \sum_{n=0}^{\infty} S_n = \exp \left[-\frac{2\alpha_s}{3\pi} \ln^2 \left(\frac{k_T^2}{Q^2} \right) \right].$$

S can be used again to solve for the differential cross section. Since k_T is an arbitrary value though, p_T can be substituted for k_T to arrive at

$$\frac{1}{\sigma_0} \frac{d\sigma}{dp_T^2} = \frac{dS}{dp_T^2} = \frac{4\alpha_s}{3\pi} \frac{1}{p_T^2} \ln \left(\frac{Q^2}{p_T^2} \right) \exp \left[-\frac{2\alpha_s}{3\pi} \ln^2 \left(\frac{p_T^2}{Q^2} \right) \right]. \quad (1.22)$$

This relation is the same as for the single gluon case, except for the exponential factor. This exponential factor, called a Sudakov Form Factor, represents the multiple gluon processes in the calculation. Note that it eliminates the divergence as $p_T \rightarrow 0$ that was present in the first order result.

1.2.4 Resummation Calculation

The cross section calculation of the previous subsection is an example of resummation, a technique of summing the contributions from processes of all orders of α_s to obtain a finite cross section. This technique was pioneered by [10]. However, the derivation in the previous subsection is not a complete solution. The approximations made only take into account soft gluon emissions, (gluon $p_T \ll$ photon p_T).



As a result, instances in which gluons are emitted with a p_T on the order of the photon's p_T are not properly considered, and vector momentum conservation is not handled properly.

To properly take into account all of these factors and yield a more accurate cross section, refinements to the resummation technique were developed [11][12]. This calculation begins by looking at the differential cross section as a perturbative series. The expression below shows the dominant contributions to the series,

$$\frac{d\sigma}{dp_T^2} \propto \frac{\alpha_s}{p_T^2} \ln\left(\frac{Q^2}{p_T^2}\right) \left[v_1 + v_2 \alpha_s \ln^2\left(\frac{Q^2}{p_T^2}\right) + v_3 \alpha_s^2 \ln^4\left(\frac{Q^2}{p_T^2}\right) + \dots \right]. \quad (1.23)$$

There is a practical problem with this series in that as $p_T \rightarrow 0$ the series does not converge due to the overall factor of $\frac{1}{p_T^2}$ and the logarithmic terms. Because this is a series in $\alpha_s \ln^2\left(\frac{Q^2}{p_T^2}\right)$, the series as is cannot converge at small p_T , ($p_T \ll Q$) even if α_s is small. This divergence can be cured by reordering the terms that are at least as singular as $\frac{1}{p_T^2}$ to produce a converging series. After the resummed part of the perturbative series is calculated, the remaining terms of the perturbative series can be calculated and added to the resummed part to obtain the full cross section calculation.

The resummation calculation begins by writing the singular terms of the perturbative series as

$$\frac{d\sigma}{dp_T^2} \sim \frac{\alpha}{p_T^2} \sum_{n=1}^{\infty} \sum_{m=0}^{2n-1} v_{nm} \alpha_s^n \ln^m\left(\frac{Q^2}{p_T^2}\right).$$

This series can be written the following way (suppressing the coefficients):

$$\frac{\alpha}{p_T^2} \left[\alpha_s (L+1) + \alpha_s^2 (L^3 + L^2 + L + 1) + \alpha_s^3 (L^5 + \dots) + \dots \right]. \quad (1.24)$$



The L term is shorthand for $\ln\left(\frac{Q^2}{p_T^2}\right)$. The series can be rearranged into the form:

$$\frac{d\sigma}{dp_T^2 dy} \sim \frac{\alpha}{p_T^2} (\alpha_s Z_1 + \alpha_s^2 Z_2 + \dots). \quad (1.25)$$

Where the terms have the following form:

$$\begin{aligned} \alpha_s Z_1 &\sim \alpha_s (L+1) + \alpha_s^2 (L^3 + L^2) + \alpha_s^3 (L^5 + L^4) + \dots \\ \alpha_s^2 Z_2 &\sim \alpha_s^2 (L+1) + \alpha_s^3 (L^3 + L^2) + \dots \\ \alpha_s^3 Z_3 &\sim \alpha_s^3 (L+1) + \dots \end{aligned} \quad (1.26)$$

Now instead of a series increasing by a factor of $\alpha_s L^2$ for each succeeding term, there is a series in α_s . This means that the convergence of the series depends only on α_s . Note that the highest power logs for each power of α_s in $\alpha_s Z_1$, $\alpha_s L + \alpha_s^2 L^3 + \alpha_s^3 L^5 + \dots$, are just terms of the LDLA result, Equation 1.22, in series form.

There are several formalisms for doing such resummings [13][14]. However the one used in this analysis is given by Collins, Soper, and Sterman (CSS) [12]. This formalism has been used to study the production of single [15][16][17][18] and double [19] weak gauge bosons as well as Higgs bosons [20]. The formalism describes the triple differential cross section as

$$\frac{d\sigma}{dQ^2 dp_T^2 dy} \propto \int_0^\infty d^2 b e^{i\vec{p}_T \cdot \vec{b}} W(b, Q, x_a, x_b)_b + Y(p_T, Q, x_a, x_b). \quad (1.27)$$

Here, the resummed piece is the integral over the W function. The Y function is comprised of the terms of the perturbative series not included by the resummed piece. Specifically, it is evaluated as the full perturbative series (non-resummed) minus the terms as singular as $\frac{1}{p_T^2}$, the “asymptotic piece.” The integration variable, b is the impact parameter and the Fourier conjugate to p_T . Small b values mean large p_T values.



The W function is explicitly written as

$$W(b, Q, x_a, x_b) \propto \sum_i \int \frac{dx_a}{x_a} \int \frac{dx_b}{x_b} f_{\frac{q_i}{A}}(x_a, Q^2) f_{\frac{q_i}{B}}(x_b, Q^2) e^{-S(b)},$$

where S has the form,

$$S = \int \frac{d\mu}{\mu} \left[A \ln \left(\frac{Q^2}{\mu} \right) + B \right],$$

and A and B are series with constants A_j and B_j respectively,

$$A = \sum_j \alpha_s^j A_j \quad B = \sum_j \alpha_s^j B_j.$$

These constants can be determined by expanding S order by order in α_s and comparing to the corresponding terms in the perturbative calculation. At present, the A_j and B_j coefficients have been calculated up to $j=2$ by Davies, Webber, and Stirling (DWS) [21].

A correction must be applied to Equation 1.27 though because α_s blows up when $b > \frac{1}{\Lambda_{QCD}}$ and therefore the integration over the full integration range from 0 to ∞ cannot be performed. In order to make a smooth limit on the integration, a quantity labelled b_* is defined as

$$b_* = \frac{b}{\sqrt{1 + (b/b_{\max})^2}}$$

and is substituted for b into W .

Now however, something must recover the range not integrated over by using b_* . This is done phenomenologically by the substitution,

$$W(b) = W(b_*) W^{NP}(b), \tag{1.28}$$



where $W^{NP}(b)$ is a function that covers the non-perturbative range. CSS [12] showed that this non-perturbative function has the generic form

$$W^{NP} = \exp\left[-h_1(x_a, b) - h_1(x_b, b) - h_2(b) \ln(Q^2)\right], \quad (1.29)$$

where the h 's are to be measured.

A simplified form for W^{NP} was first tested by DWS [21] using the Duke and Owens PDF [22],

$$W^{NP} = \exp\left[-g_1 b^2 - g_2 b^2 \ln\left(\frac{Q}{2Q_0}\right)\right], \quad (1.30)$$

where the g parameters were constants determined by a fit to data. Their results were combined with a next-to-leading-order calculation [23] by Arnold and Kauffman [15] providing the first complete prediction for hadron collider DY data with the CSS formalism.

Another specific form for the function was given by Ladinsky and Yuan in 1994 [24] and also fit to data. This non-perturbative function differs from the DWS function in that it has three g parameters and a dependence on τ ,

$$W^{NP} = \exp\left[-g_1 b^2 - g_2 b^2 \ln\left(\frac{Q}{2Q_0}\right) - g_1 g_3 b \ln(100 x_a x_b)\right]. \quad (1.31)$$



Chapter 2

Fermilab and the DØ Detector

2.1 The Accelerator at Fermilab

The accelerator located at Fermi National Laboratory in Batavia, Illinois is a facility which accelerates protons and antiprotons to near light speed. The accelerator can operate in two modes. In one mode beams of protons and antiprotons are collided. The other operating mode extracts a beam of protons to external stationary targets. The analysis in the next chapter was done for data produced from proton-antiproton collisions and therefore the collider mode of the accelerator will be described.

The Fermilab accelerator is actually a system of separate accelerators [25]. The beam is accelerated in stages, analogous to an automobile engine with gears, with a different accelerator handling each stage. Figure 2.1 shows a diagram of the location of the accelerators relative to each other.

The process of creating high energy beams of protons and antiprotons begins in a Cockcroft-Walton accelerator. Here, electrons are added to hydrogen atoms to produce singly charged negative ions. These ions are accelerated to an energy of 750,000 electron volts (eV) by applying a positive voltage.



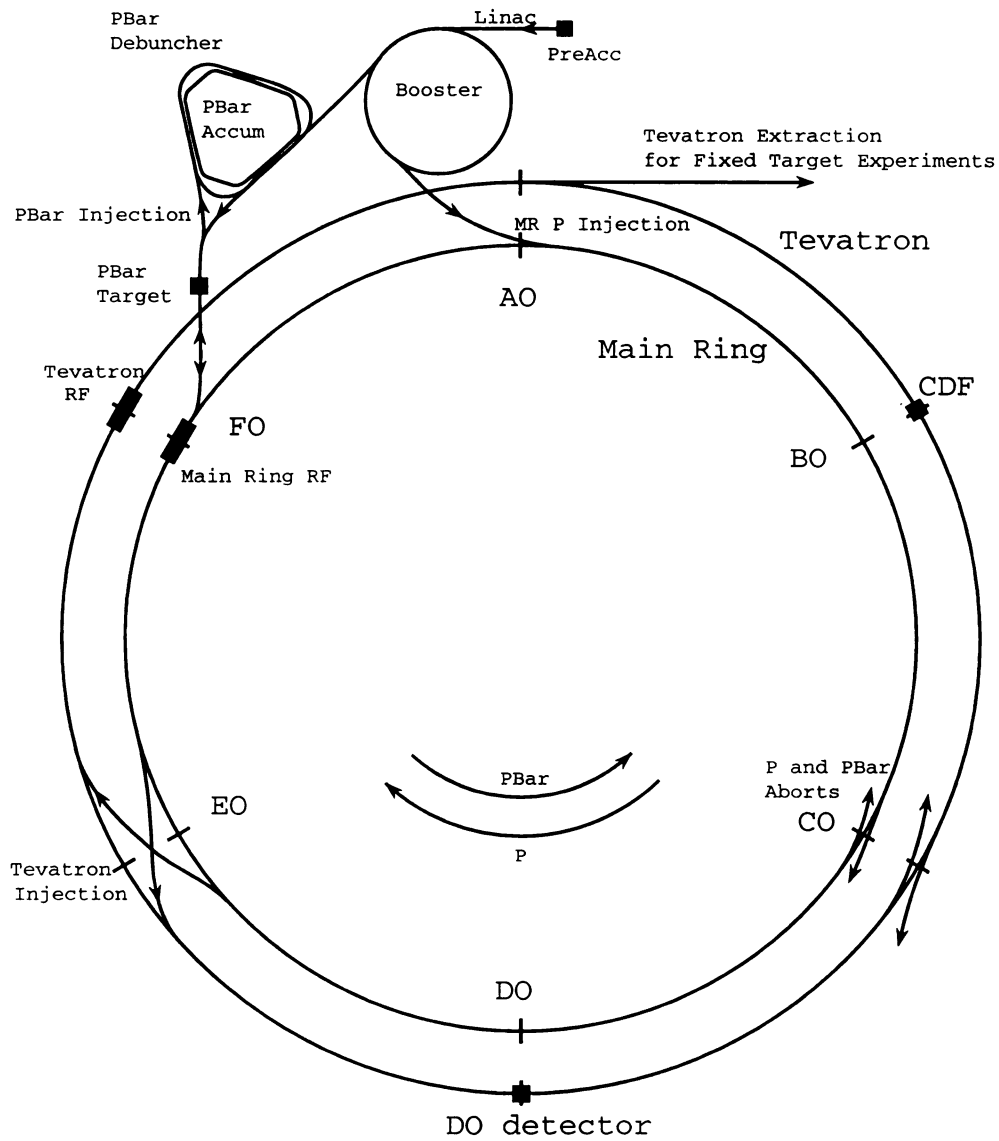
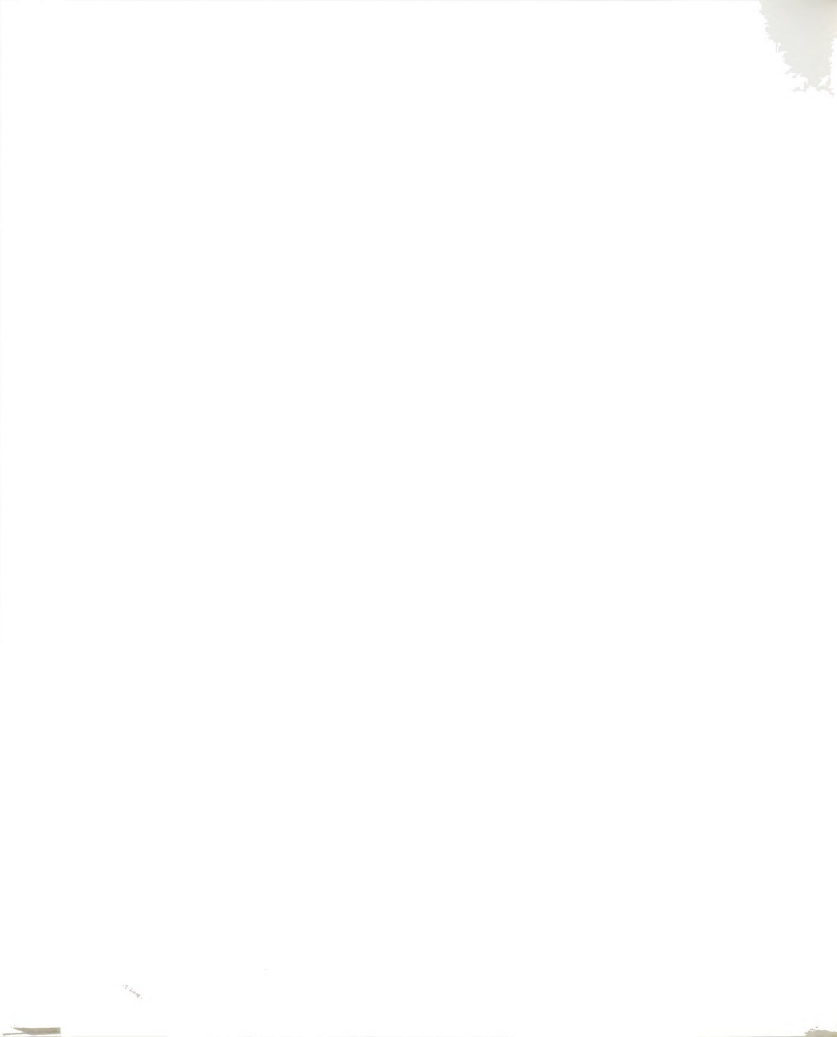


Figure 2.1: The system of accelerators at Fermilab used to accelerate protons and antiprotons.



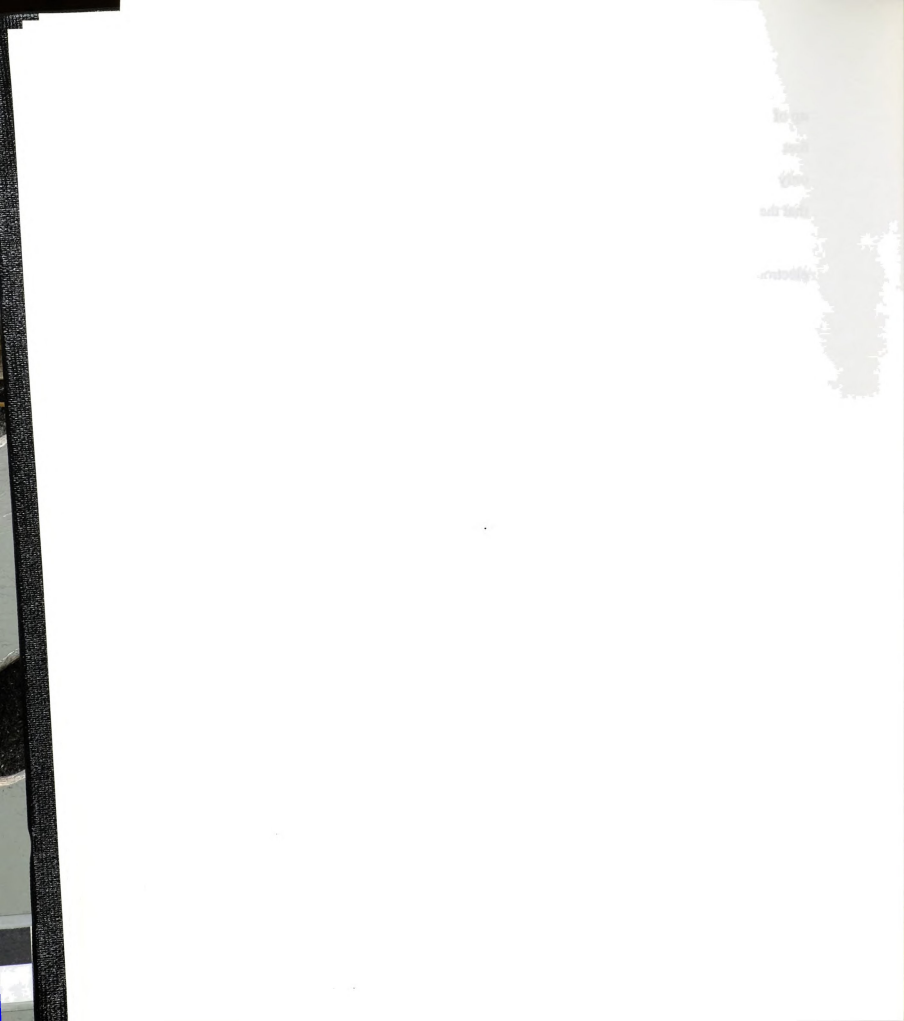
The accelerated ions then pass into a linear accelerator or linac. The linac is made up of five tanks containing drift tubes connected end to end in a line approximately 500 feet long. The ions are accelerated through the tubes by an oscillating electric field which only acts on the ions when they are in the gaps between the tubes. The system is timed so that the ions are in the gaps only when the electric field is pointing in the direction to accelerate the ions toward the next stage. The linac accelerates the ions to 400 million electron volts (MeV) which are then passed through a carbon foil. The foil strips away all the electrons leaving only bare protons to pass on to the next stage.

The next accelerator, the Booster, is a synchrotron. Synchrotrons are ring-shaped accelerators in which charged particles are kept travelling in the ring with dipole bending magnets. The acceleration is done by cavity electric fields, which increase the particle's energy with each revolution. The Booster is 500 feet in diameter and 20 feet below ground. The protons travel around the Booster about 20,000 times until they attain an energy of 8 GeV. When the protons leave the Booster they are injected into the Main Ring in bunches.

The Main Ring, like the Booster, is a synchrotron. However, the Main Ring is four miles in circumference and contains a thousand dipole, quadrupole, and higher order magnets for bending and focusing. The beam in the Main Ring is made up of bunches because the acceleration is provided by RF cavities.

From the Main Ring, the protons will take one of two paths. They are either sent into the Tevatron accelerator or extracted from the Main Ring to produce antiprotons. Protons bound for the Tevatron make revolutions in the Main Ring until accelerated to 150 GeV in energy. Those to be used to produce antiprotons are raised to an energy of 120 GeV.

To make antiprotons, protons are extracted from the Main Ring and sent to collide into a nickel target. Among the products of the collisions are antiprotons, which are produced in bunches since the protons arrive at the target in bunches.



It takes about a million protons colliding with the target to produce twenty antiprotons. These antiprotons are magnetically selected and sent to the Debuncher Ring which has a rounded, triangular shape. When the antiprotons come out of the target, their energy distribution is too widely spread. The Debuncher makes the energy distribution more compact by a process of stochastic cooling. The process involves analyzing the antiprotons for deviations from an ideal orbit and applying a corrective “kick” to minimize these deviations. The roughly triangular shape more easily allows the signal for the kick to arrive before the beam. After this step, the antiprotons are sent to the Accumulator Ring for storage until enough antiprotons have accumulated. Once enough of them are produced, they are injected into the Main Ring and passed into the Tevatron.

The final acceleration stage is the Tevatron where the collisions between protons and antiprotons take place. The Tevatron is a synchrotron ring located directly under the Main Ring in the same tunnel. The Tevatron uses magnets with superconducting coils to accelerate protons and antiprotons to 0.9 TeV, thus its name. Both protons and antiprotons are simultaneously accelerated in the ring, traveling in opposite directions until they attain maximum energy and then continue to travel through the ring at that energy. The proton and antiproton beams consist of six bunches each. Once both beams are at maximum energy, the counter rotating bunches are focused to produce collisions in the centers of two detectors, one of which is the DØ Detector.

2.2 The DØ Detector

The DØ Detector is one of two collider detectors in the Tevatron ring. The detector was designed to be nearly hermetic in detecting almost all particles resulting from a collision, (neutrinos being the notable exception.). It was also designed to measure three important properties of detected particles. The three properties are the energy, the trajectory vector, and the particle’s identity.



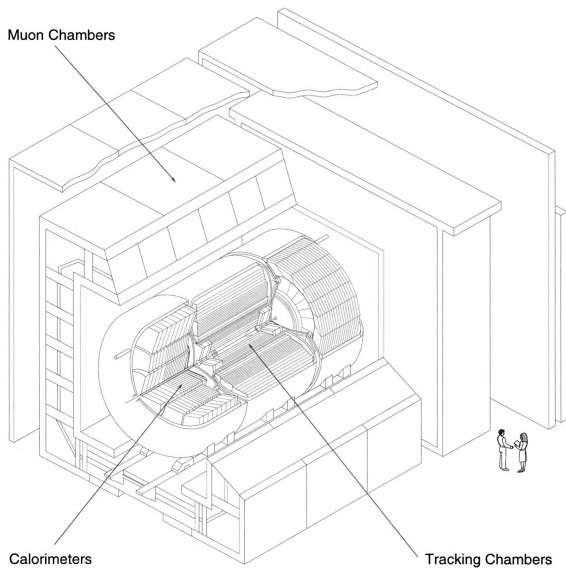


Figure 2.2: The DØ Detector showing each subdetector.



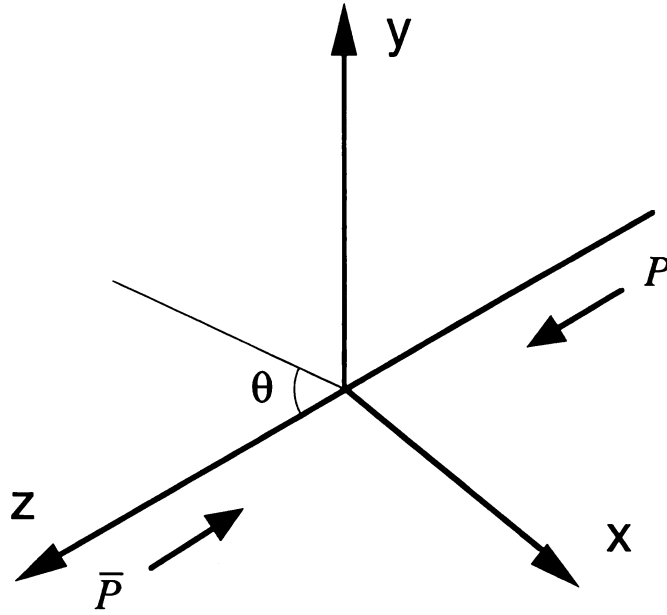
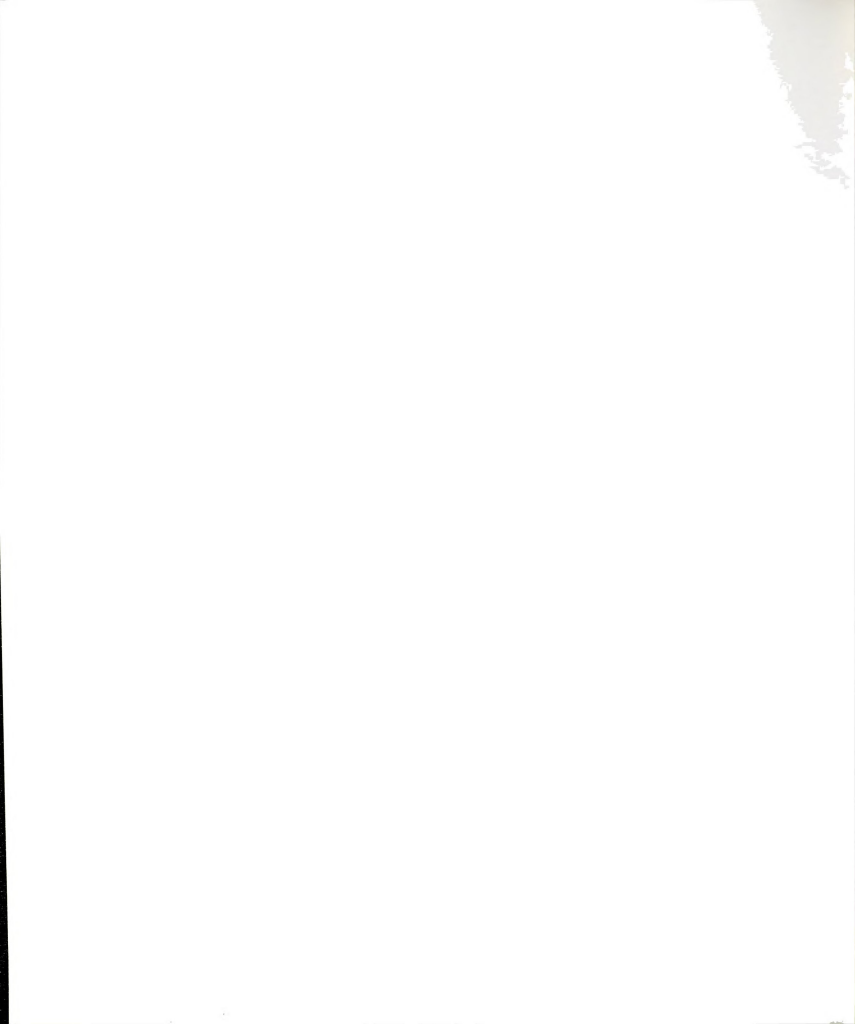


Figure 2.3: Representation of the DØ coordinate system.

In order to fulfill these separate but equally important goals the DØ Detector is made up of several components, each of which is optimized to measure a certain aspect of a particle. These subdetectors are described separately in the following sections where [26] has been used as the main reference.

DØ uses a coordinate system which has its origin at the nominal beam collision point. The z axis is aligned along the central axis of the beam pipe with z increasing in the direction of the proton beam. The y axis points straight up. With θ defining the usual azimuthal angle, it is often more convenient instead to use pseudorapidity, η , defined in Equation 2.1. In the limit that a particle's mass is much less than its total energy, η approaches the rapidity given in Equation 1.2.

$$\eta = -\ln \tan \frac{\theta}{2} \quad (2.1)$$



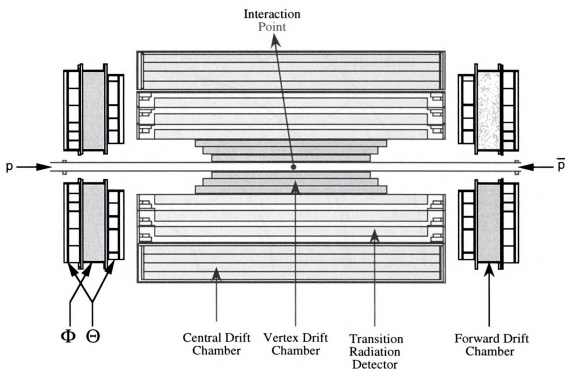


Figure 2.4: Cutaway view of the Central Detectors.

2.2.1 Central Detectors

The primary task of the central detectors is to accurately measure a particle's track, which is the path of a particle leaving the collision. The central detectors are the Vertex Drift Chamber (VTX), the Transition Radiation Detector (TRD), the Central Drift Chamber (CDC), and the Forward Drift Chambers (FDC). The VTX, TRD, and CDC are contained within a cylinder with the beamline at the central axis as shown by Figure 2.4. The two FDC detectors are at each end of this cylinder.

The VTX chamber is contained within a cylinder of outer radius 16.2 cm and has the beam pipe as its central axis. The inner radius of the VTX is 3.7 cm, which is just outside the beam pipe. The VTX actually consists of three separate independent layers concentric in radial distance, r . Each layer is also divided in equal sections, or cells, in ϕ with the innermost layer containing 16 cells and the outer two partitioned into 32 cells.



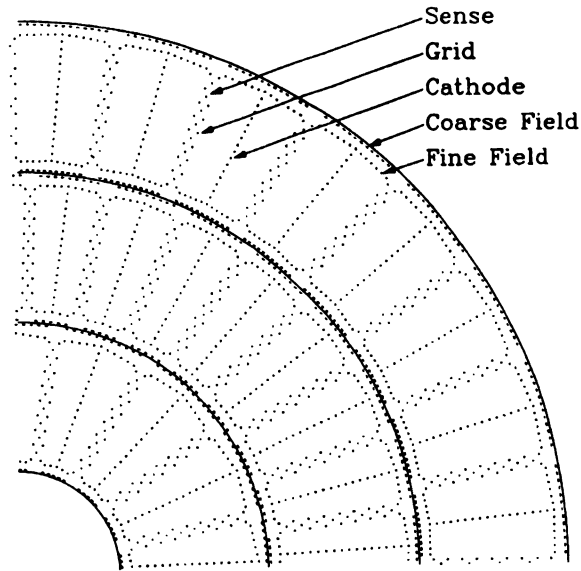


Figure 2.5: The VTX chamber with the layout of its wires.

The VTX chamber was designed to measure the tracks of charged particles. The cells in the VTX accomplish this by measuring the charge on sense wires resulting from the passage of charged particles ionizing the gas inside the cell. The ionized gas drifts to the sense wires due to electric fields shaped by other wires in the cell. Figure 2.5 shows the layout of the various wires in the VTX.

The Transition Radiation Detector (TRD) lies between the VTX and CDC detectors. It was designed to help identify whether a particle is an electron. The TRD uses the principle that highly relativistic particles emit photons when they pass through a boundary between materials with different dielectric constants. The energy of the photons is dependent on the mass of the particle and therefore the much lighter electron can be distinguished from a hadron.

The TRD consists of three concentric layers. Each layer has a radiator and an X-ray detector. The radiator is a collection of 393 layers of $18\text{ }\mu\text{m}$ thick polypropylene foil spaced an average $150\text{ }\mu\text{m}$ apart. X-rays are detected through the use of a charge



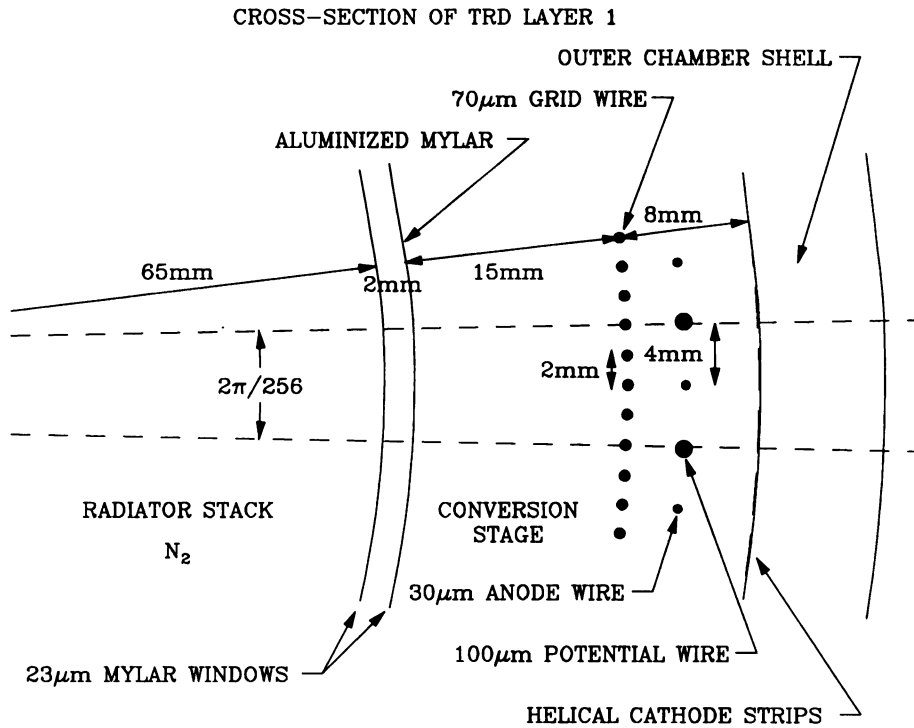


Figure 2.6: Cross section of a TRD chamber.

drift chamber. When charged particle pairs from converted X-rays and other charged particles pass through the chamber, they will produce an avalanche of charge that drifts to sense wires. The setup is shown in Figure 2.6.

Outside of the TRD is the Central Drift Chamber, or the CDC. Like the VTX it is also a drift chamber detector and its purpose is also to measure the tracks of charged particles. The CDC is a 184 cm long cylindrical shell surrounding the TRD with an inner radius of 49.5 cm and an outer radius of 74.5 cm. The CDC is constructed of four layers with each layer sectioned into 32 cells with equal ϕ coverage.

The ϕ positioning of the cells between adjacent layers is staggered by a half cell. This is to insure that a particle will travel through cells on at least two layers. Each of the cells contains seven sense wires and two delay lines. The delay lines are placed between the cell walls and the two outermost sense wires. Charged particles passing through a cell will ionize the gas with the charge drifting to the seven sense wires.

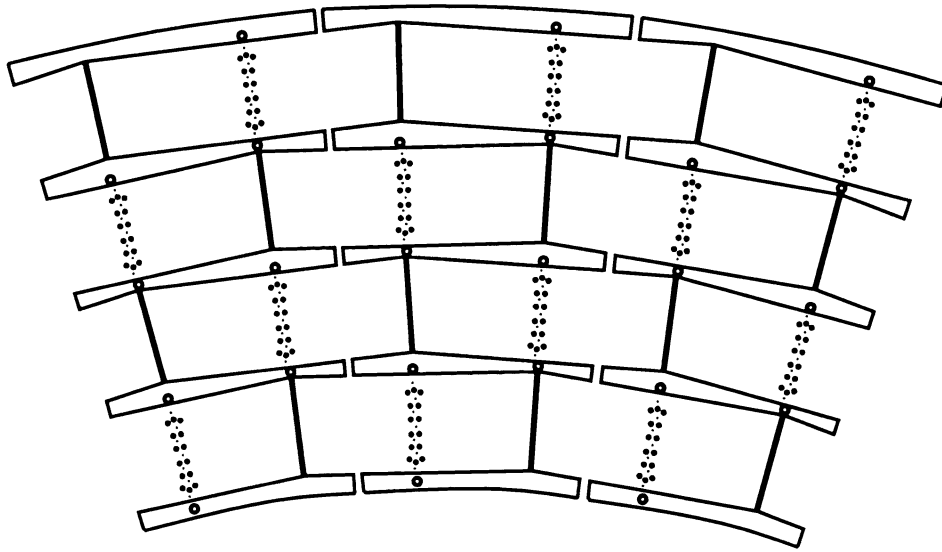


Figure 2.7: Cutaway view of the CDC showing the wire placement in each cell.

The drift time to the sense wires gives r and ϕ information on the track. Accumulated charge on the sense wire adjacent to a delay line will induce a charge on the delay line. This charge will travel down the delay line in two pulses traveling to opposite ends of the line. The time of arrival of both pulses gives a z position for that portion of the track nearest the delay line. Appendix B details a project to recalibrate this z measurement.

Unlike the other central detectors, the Forward Drift Chambers (FDC) are not cylindrical shells encompassing the beam line, but are, as Figure 2.4 shows, two roughly disk shaped detectors placed on both ends of the other central detectors. The purpose of the FDC is to measure tracks for particles with rapidity outside the range of the CDC and it does this with the use of drift chambers. Each detector is made up of three modules. There are two Θ modules and a Φ module sandwiched between them as Figure 2.8 illustrates. As the figure shows, the Θ modules are rotated by 45° relative to each other. As the names suggest, the Θ modules measure the θ coordinate and the Φ module measures the ϕ coordinate.



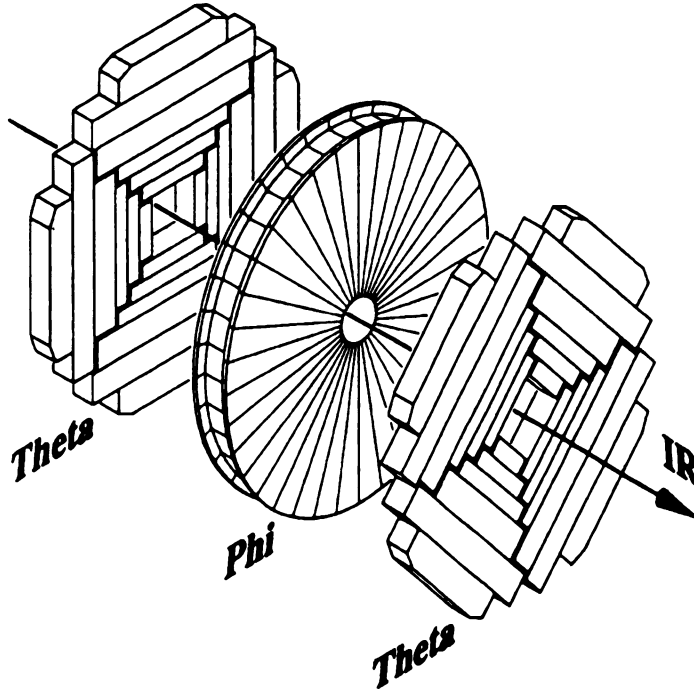
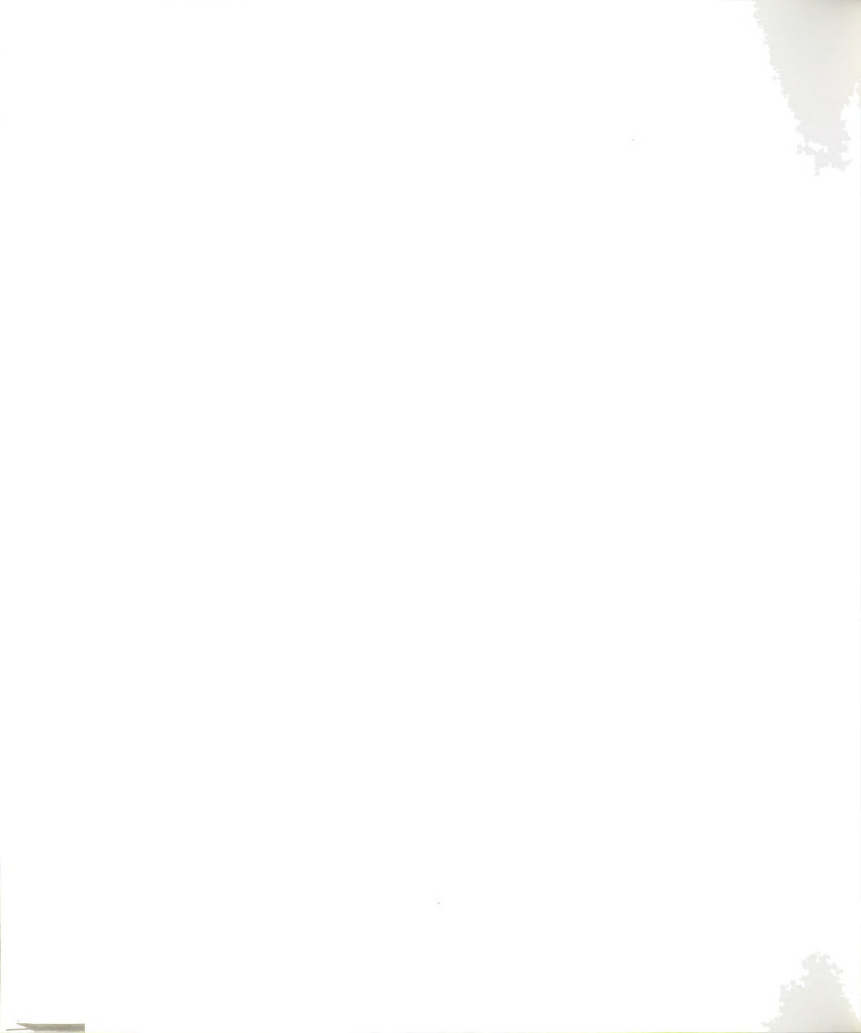


Figure 2.8: The three modules which make up each of the Forward Drift Chambers.

2.2.2 Calorimeter

The calorimeter for DØ is designed to measure the energy of particles from collisions and also to provide for identification for some of those particles. The calorimeter is made up of three main sections, the central calorimeter and two end calorimeters as shown by Figure 2.9. The central calorimeter covers the region $|\eta| \leq 1$, the end calorimeter south covers $1 \leq \eta \leq 4$, and the end calorimeter north, the range $-4 \leq \eta \leq -1$.

Each of the three calorimeters is made up of box shaped cells. Figure 2.10 shows that a cell consists of an absorber and a signal readout board with liquid Argon in the gap between them. When a particle hits the absorber plate, it produces secondary particles which then ionize the liquid Argon. The signal readout board is kept at 2 to 2.5 kV potential relative to the absorber plate so that charge will drift to the signal readout board.



LIQUID ARGON CALORIMETER

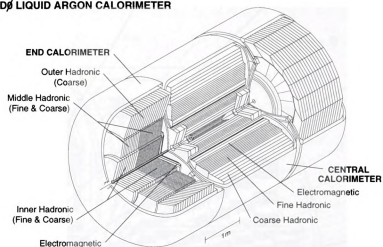


Figure 2.9: Cutaway view of the calorimeter.

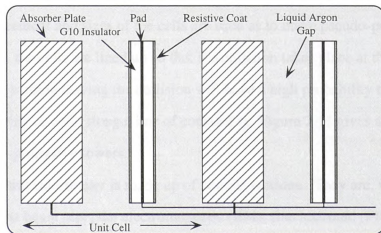


Figure 2.10: Representation of a typical calorimeter cell.

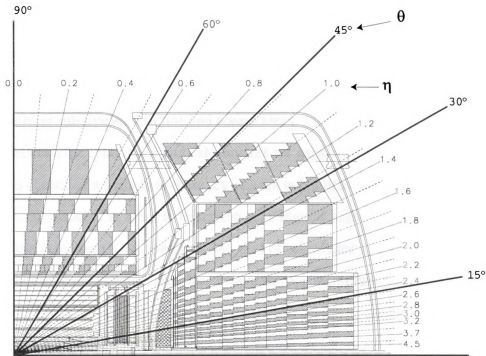


Figure 2.11: A portion of the calorimeter with pseudo-projective towers at different η .

The placement and sizes of the cells are such as to make pseudo-projective towers. That is, the cells are lined up so that if a collision takes place at the center of the DØ Detector, a particle leaving the collision will have a high probability to pass through a continuous string of cells along a line of constant η . Figure 2.11 gives a representation of these pseudo-projective towers.

The central calorimeter is made up of several sections. They are, with increasing distance from the beam pipe, the electromagnetic (EM), fine hadronic (FH), and coarse hadronic (CH) sections. There are 32 EM cells in ϕ and 16 FH and CH cells. The EM section uses 3 mm thick depleted uranium absorbers, and has a total radiation length (X_0) and interaction length (λ_A) of 20.5 and 0.76 respectively. A 6 mm thick uranium-niobium alloy is the absorber material for the FH cells. The total radiation length and interaction

length for the FH section is 96.0 and 3.2 respectively. The CH cells use 46.5 mm thick copper for their cell's absorbers. The CH section has 32.9 and 3.2 for its radiation length and interaction length.

The end calorimeters also have different sections. They are the EM, inner hadronic (IH), middle hadronic (MH), and outer hadronic (OH) sections. The IH and MH are further subdivided into fine and coarse areas.

Between the central and end calorimeters are gaps covering $0.8 \leq |\eta| \leq 1.4$. To reduce the chance of a particle in these regions not being detected, arrays of scintillating counters were installed in order to lessen the dead regions in the gaps. These intercryostat detectors (ICD) consist of 384 tiles of scintillator material. Each tile has three or four grooves in which are placed wave shifting scintillating fiber. These scintillating fibers are fed into photomultiplier tubes.

2.2.3 Muon Detector

Encasing the calorimeter is a detector to identify and measure muons. It is made up of inner proportional drift tube chambers (PDT's), iron toroids, and outer PDT's. One layer of PDT's lie just inside the iron toroids. The iron toroids generate a magnetic field which bends muons as they pass through. Two outer layers PDT's then measure a muon's track after it passes through a toroid. By comparing a muon's track from the inner PDT's to the track from the outer PDT's the extent of the bending of the muon's trajectory can be measured. The amount the muon bends provides a measurement of its momentum.

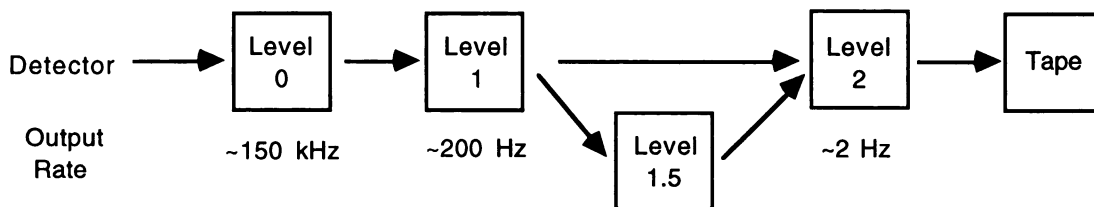


Figure 2.12: Schematic view of the different trigger levels.

2.2.4 Triggering System

The goal of the trigger system is to maximize the interesting physics events recorded. The trigger does this by making preliminary calculations of certain quantities of a beam crossing and deciding whether it constitutes an interesting event. This prevents uninteresting physics from being recorded to tape. Not only does this keep the DØ data sample clean, but it also leaves the detector free to examine succeeding beam crossings rather than wasting time calculating quantities for an uninteresting beam crossing. The trigger system consists of 4 levels, named level 0, 1, 1.5, and 2. For an event to be recorded as DØ data, it must pass the criteria set by at least three of these levels, with level 1.5 being required for only a subset of events. Therefore the path an event takes to tape is to first pass through level 0, then level 1, possibly level 1.5, and finally level 2. Figure 2.12 illustrates this path.

The central piece in the level 0 trigger is the level 0 detector. This detector consists of two square arrays of scintillator counters each mounted on the forward face of one of the end calorimeters and having partial coverage in the $1.9 \leq |\eta| \leq 4.3$ range. The scintillator counters are read out into photomultiplier tubes. This detector basically determines whether an inelastic collision has taken place, and if so, makes a rough calculation of the z position of the interaction vertex. It determines whether a beam crossing resulted in an inelastic collision by the criteria that both scintillator arrays must register a signal within a certain time period of each other. The z coordinate of the vertex of an inelastic collision is calculated from the time difference between the two signals.



With the time between beam crossings at $3.5 \mu\text{s}$, the level 0 trigger passes events at the rate of about 150 kHz.

The level 1 trigger uses quick calculations made from the muon detector and calorimeter level 1 triggers to decide whether a collision is interesting physics. This decision is made by the level 1 framework.

The level 1 calorimeter trigger makes calculations of the component transverse to the beam line of several energies such as the total transverse energy, E_T , the hadronic E_T , the electromagnetic E_T , the missing E_T , and the E_T of the trigger towers. The trigger towers consist of the pseudo-projective towers in the calorimeter described on page 40.

The trigger framework makes its decisions using 256 bits called AND-OR terms. Each of these bits are flags indicating whether a certain condition has, or has not been met by an event. An example of such a condition is testing whether an event had a minimum amount of hadronic energy. The framework also contains 32 programmable specific triggers which contain sets of these AND-OR terms. An event passes a specific trigger only if all of the AND-OR terms match the state required by the specific trigger. But in order to pass the level 1 trigger an event has to meet the conditions of only one specific trigger. The level 1 trigger passes events at a rate of about 200 Hz.

Some of the specific triggers are flagged for the level 1.5 trigger. If an event passes the criteria for one of these specific triggers, then they are passed on to the level 1.5 trigger where several quantities are measured more accurately than was done at level 1. Appendix A describes a program that monitors Levels 1 and 1.5 operations.

The level 2 trigger is comprised of a network of DEC VAX 4000's running filtering software. Here, the filtering software uses quantities calculated more accurately than at levels 1 and 1.5 which is allowed due to the smaller event input rate. A specific example of a level 2 filter is the one for obtaining Z events. This filter requires the presence of two clusters of deposited energy resembling electrons with $E_T > 20 \text{ GeV}$ and $E_T > 16 \text{ GeV}$. Events at level 2 are filtered so that events pass only at a rate of 2 Hz.

Chapter 3

Refinement of DØ Z Data

3.1 Introduction

Prior to the publication of the DØ $Z p_T$ distribution it was felt that some further studies could possibly refine the already completed analysis [27]. Some of these additional studies involved the use of a Monte Carlo which was used to simulate Z events in the DØ detector. Another project was the development and use of a specialized program to produce properly smeared $Z p_T$ distributions for studies in the high p_T region.

3.2 Studies With Fast Monte Carlo

A fast Monte Carlo, named the CMS Monte Carlo, was used in the $Z p_T$ analysis in order to measure the acceptance and as a model for the detector smearing. This Monte Carlo was first devised for the W mass measurement at DØ [28] [29]. This section describes studies which were performed in order to better understand the behavior of this Monte Carlo and to learn if there are kinematic regions in which the measured $Z p_T$ differs greatly from the true p_T .

Chapter
Outline

Page
Number

3.2.1 Examination of Kinematic Variables

The aim of the first study was to learn from the simulator if there is a range for one or more kinematic quantities in which the smeared, or measured, Zp_T is far off in value from the unsmeared, or true p_T . If such a region was found, then it might have to be removed through a cut on the data sample. The Z kinematic quantities studied were the transverse momentum, rapidity, and mass. The z of the interaction vertex and some properties of the most energetic electron were also included in the study. All of the kinematic variables considered were the smeared values, because these would be the only values available for measurement in an actual data sample.

In order to examine the effect of these kinematic quantities on the smearing of the Zp_T , profile histograms were made of the absolute value of the resolution as a function of each of the kinematic quantities. The absolute resolution is defined as

$\left| \frac{Zp_T^{\text{smeared}} - Zp_T^{\text{unsmeared}}}{Zp_T^{\text{unsmeared}}} \right|$. A profile histogram plots the average y value and its σ in each bin of x . One advantage of a profile histogram over a two dimensional scatter plot is that it is easier to notice any trends as a variable changes. Also if the population of events is heavily concentrated in one region of values in x , then it can appear in a scatter plot that the Zp_T smearing is greater in that region simply because there are more points to plot in that region. This problem is avoided with the profile histogram.

It should be noted that with one exception, the requirement, unsmeared $Zp_T > 0.5$ GeV, was used in making the profile plots shown in this subsection. This cut was made because the denominator in the resolution function blows up as $p_T \rightarrow 0$, giving large resolution values for what are actually insignificant amounts of smearing. The exception to this cut is the plot of the resolution versus the Zp_T , which was kept as is in order to illustrate this problem with the low p_T area. This cut only eliminates 0.85% of the total sample and still leaves enough low p_T events to accurately represent this region in the plots.



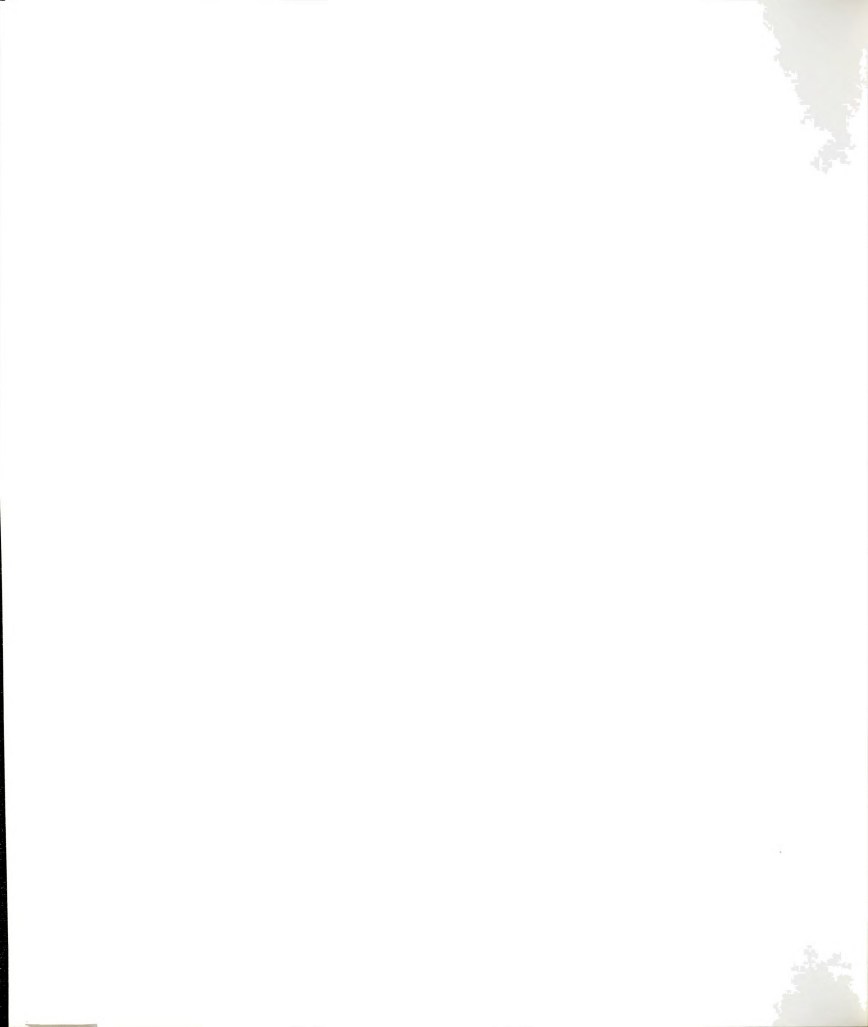
Experimentally, the mass of the Z is arrived at by measuring the invariant mass of the electron pair. From the plot of the resolution versus the Z mass in Figure 3.1, it is apparent there is no dependence on the mass. The data sample used for the $Z p_T$ distribution actually only includes events with a measured Z mass between 75 and 105 GeV in order to minimize the contamination of photon Drell-Yan events. In this mass range of the profile plot, the average resolution is about 20%.

There also is little dependence of the p_T resolution on the Z rapidity as seen from the plot in the same figure. There is only a 0.5% difference in the resolution between small absolute y and large absolute y events.

The plot showing the change in p_T smearing as a function of p_T in Figure 3.2, shows a steady resolution less than 5% except at the lowest p_T . This jump at smallest p_T , as explained earlier, can be attributed to the denominator of the resolution going to zero in this region. Finally, the plot of the vertex z versus the p_T resolution shows there is no systematic dependence on this variable.

The second set of plots in Figure 3.3 and Figure 3.4 shows several kinematic variables for the highest p_T electron in an event. The resolution in $Z p_T$ does show a tendency to get larger as the electron energy becomes smaller, with the peak resolution near 20%. When the $Z p_T$ resolution is plotted against the pseudorapidity of the electron it can be seen that the resolution is fairly constant at or below 20% over the entire range. Finally, in examining the effect of the p_T of the electron on the resolution, there is a sharp peak to the resolution of 22.5% at a p_T of 40 GeV, though this is within an acceptable level.

Overall, while the $Z p_T$ resolution does show a functional dependence on some of these kinematic variables, the resolution never reaches an unacceptably large level which would require any additional cutting on the data.



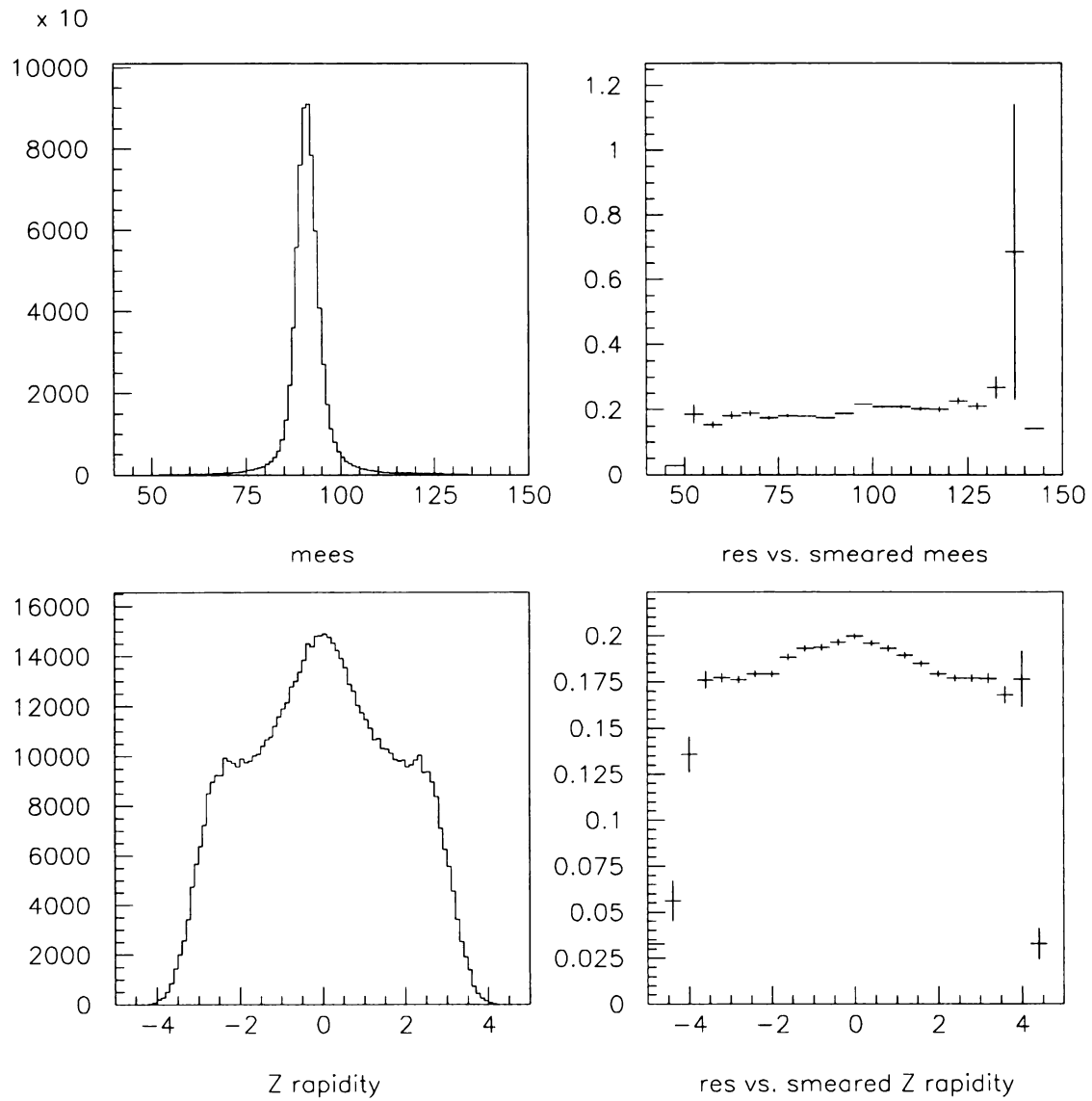


Figure 3.1: Dependence of the absolute resolution on the Z mass and rapidity.



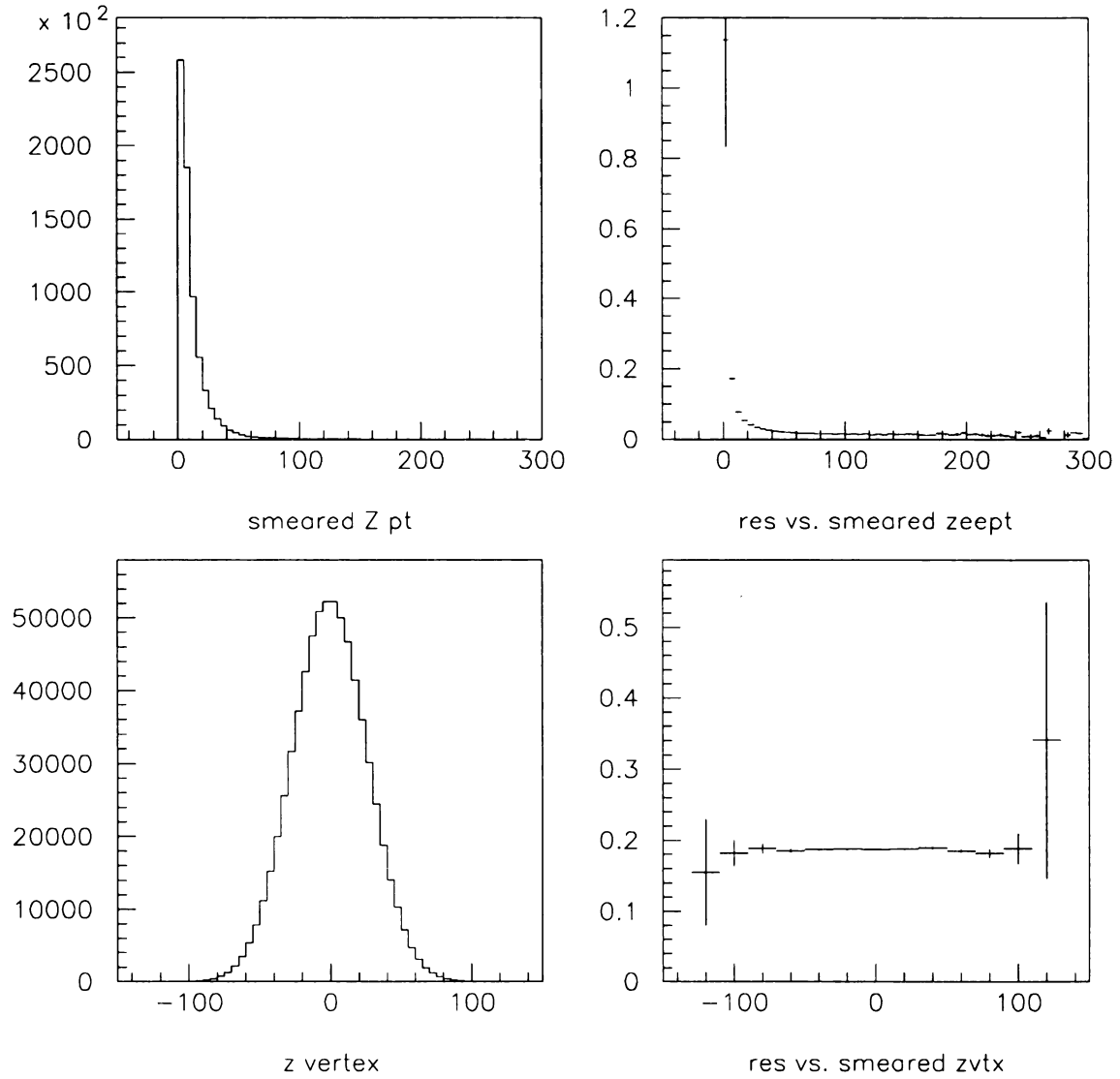


Figure 3.2: Absolute resolution dependence on the $Z p_T$ and the z of the interaction vertex.



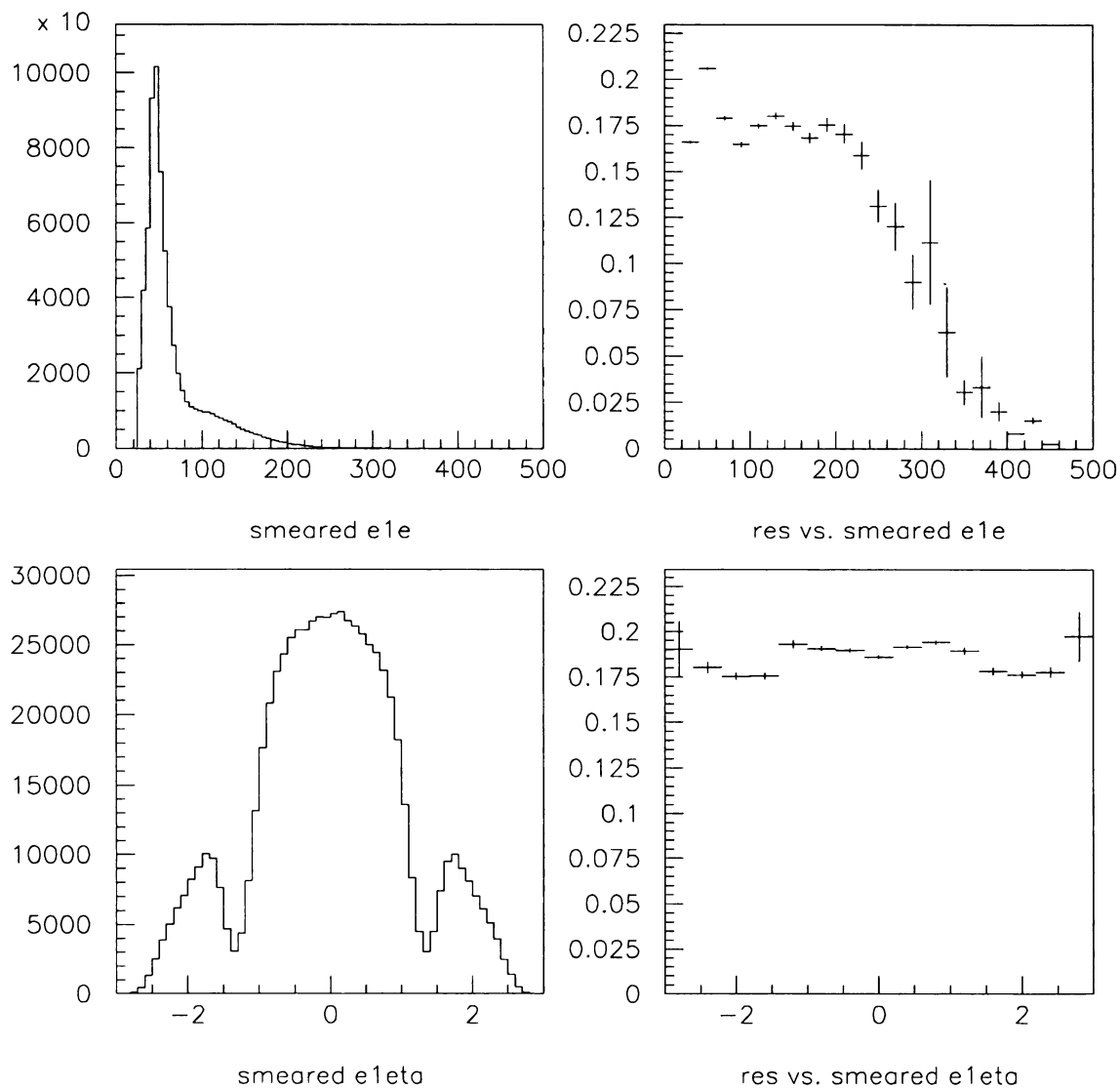


Figure 3.3: Absolute resolution dependence on the energy and pseudorapidity of the highest p_T electron.



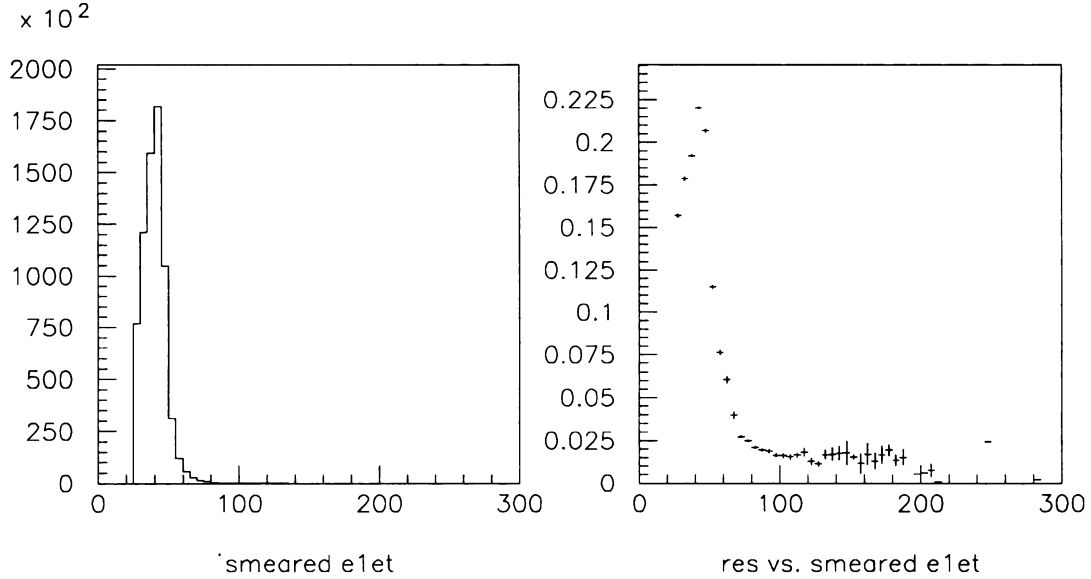


Figure 3.4: Absolute resolution dependence on the p_T of the highest p_T electron.

3.2.2 Studying Contributions to Smearing Resolution

The purpose of the next study was to discover the contribution to the $Z p_T$ absolute resolution (as defined in the last subsection) from the various detector effects. This was accomplished by independently turning on smearing for each kinematic quantity one at a time and analyzing the effects on the resolution. These studies were performed separately for events which had both electrons in the central calorimeter, “CCCC” events, and for events with one electron in the CC and the other in the EC, or “CCEC” events.

The detector effects against which the resolution was compared were the EM calorimeter position resolution, the EM calorimeter energy resolution, the track resolution, the underlying event contribution to the electron energy, and the resolution in the z coordinate of the interaction vertex. The EM calorimeter position resolution quantifies how well the calorimeter is able to determine the trajectory of an electron from its energy deposition in the calorimeter. The EM calorimeter energy resolution is the accuracy of the EM calorimeter in measuring the energy of the electron. The track resolution is the detector’s accuracy in determining the angle and position of tracks in the

CDC and FDC. The underlying event is the product of the noninteracting partons from the initial proton and antiproton. In real events, these “leftover” partons decay into particles in which the momentum vectors sum to zero. However, when any of these particles deposits energy in the same portion of the calorimeter as an electron, this extra energy will inflate the p_T of that electron beyond its true value, which will introduce an error in a $Z p_T$ measurement. The resolution on the z coordinate of the interaction vertex is self explanatory.

The figures of $Z p_T$ vs. absolute resolution on the following pages show the contribution of each of these quantities on the total resolution of the $Z p_T$. The jump in the resolution at the lowest p_T bin for these plots has the same explanation given in the last subsection and the same cut was made, $Z p_T > 0.5$ GeV.

For the EM calorimeter resolution, the $Z p_T$ resolution for CCCC events is a near constant 2% above p_T of 20 GeV. The resolution peaks at 33.5% for the 0-5 p_T bin, which only amounts to a maximum, average smearing of 1.7 GeV. The CCEC events have a similar distribution, with the resolution peaking at a smaller 24% at the low p_T end. Thus the EM calorimeter resolution should introduce only small errors to the measured $Z p_T$ distribution. The accuracy of the EM calorimeter position measurement shows itself to have even a smaller effect on the overall resolution. The $Z p_T$ resolution has a value less than 1% for all p_T less than 20 GeV with the CCCC events. Here, the low p_T peak is under 9.5% which gives a maximum average smearing of under 0.5 GeV for that lowest bin. The smearing of the $Z p_T$ is somewhat less for the CCEC events, with the resolution under 1% for nearly all p_T .

The track resolution is a negligible contribution to the $Z p_T$ resolution when compared to the resolutions from the calorimeter measurements. For CCCC events it is also fairly constant in p_T and its value remains below 0.5% for all $p_T > 20$ GeV. A somewhat improved distribution is seen for the CCEC events, especially for the lower end of the p_T range.

The next resolution effect studied, the underlying event contribution, repeats the pattern of being under 1% for both CCCC and CCEC events for all but the lowest p_T . However unlike in the other cases, the distribution for the CCEC events shows a higher overall smearing than the CCCC distribution. The z vertex resolution has the smallest contribution to the Z resolution with values less than $10^{-5}\%$.

All of these contributions to the Z resolution are small, with each averaging less than a few percent in the smearing of the $Z p_T$ with the largest contribution coming from the EM calorimeter resolution. Even when the absolute resolution peaks above 30% as it does in some plots, it amounts to 1.7 GeV in average smearing at most.



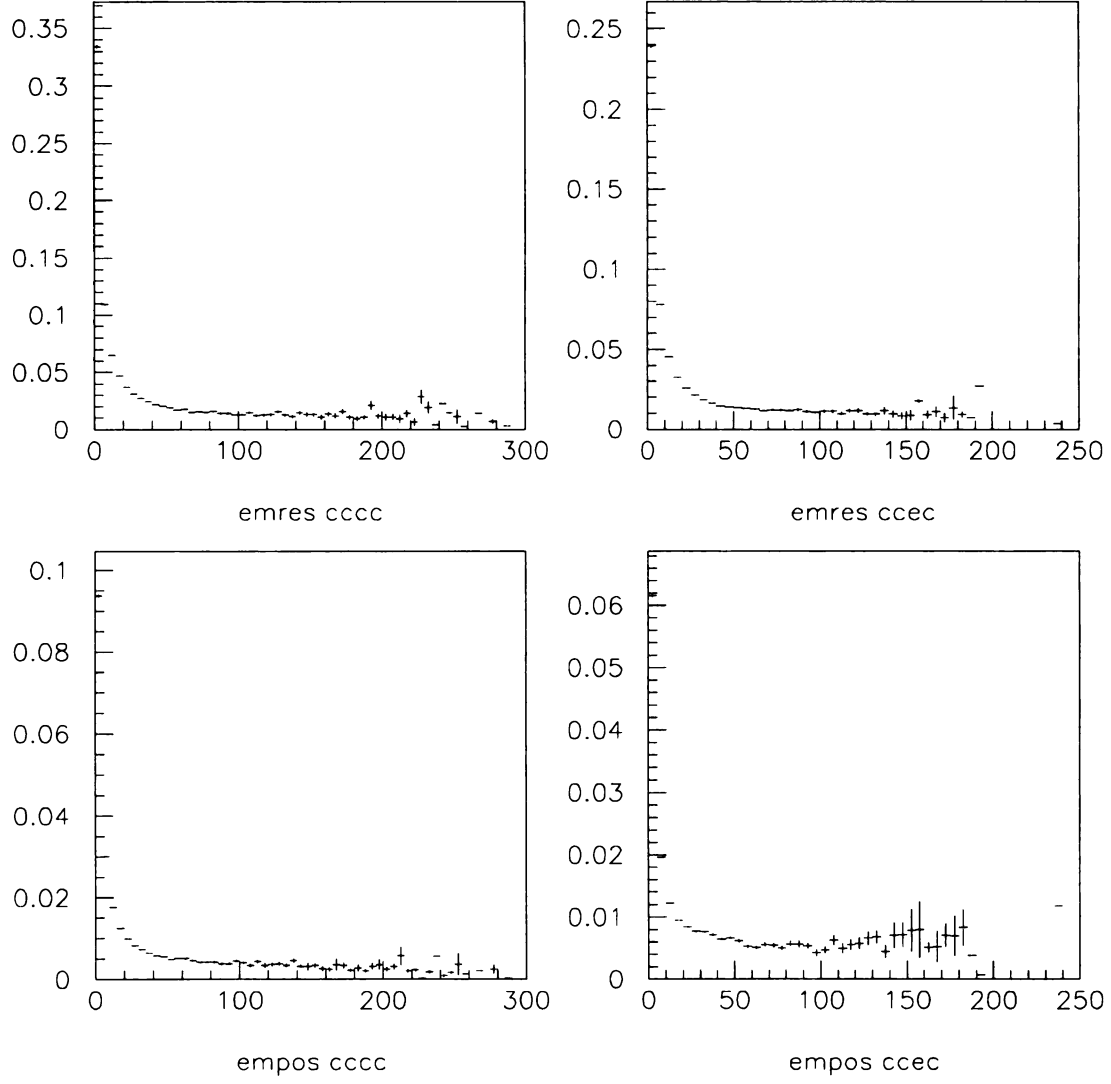


Figure 3.5: Effect of EM calorimeter energy and position resolutions on the $Z p_T$ absolute resolution. The absolute resolution is plotted as a function of $Z p_T$.



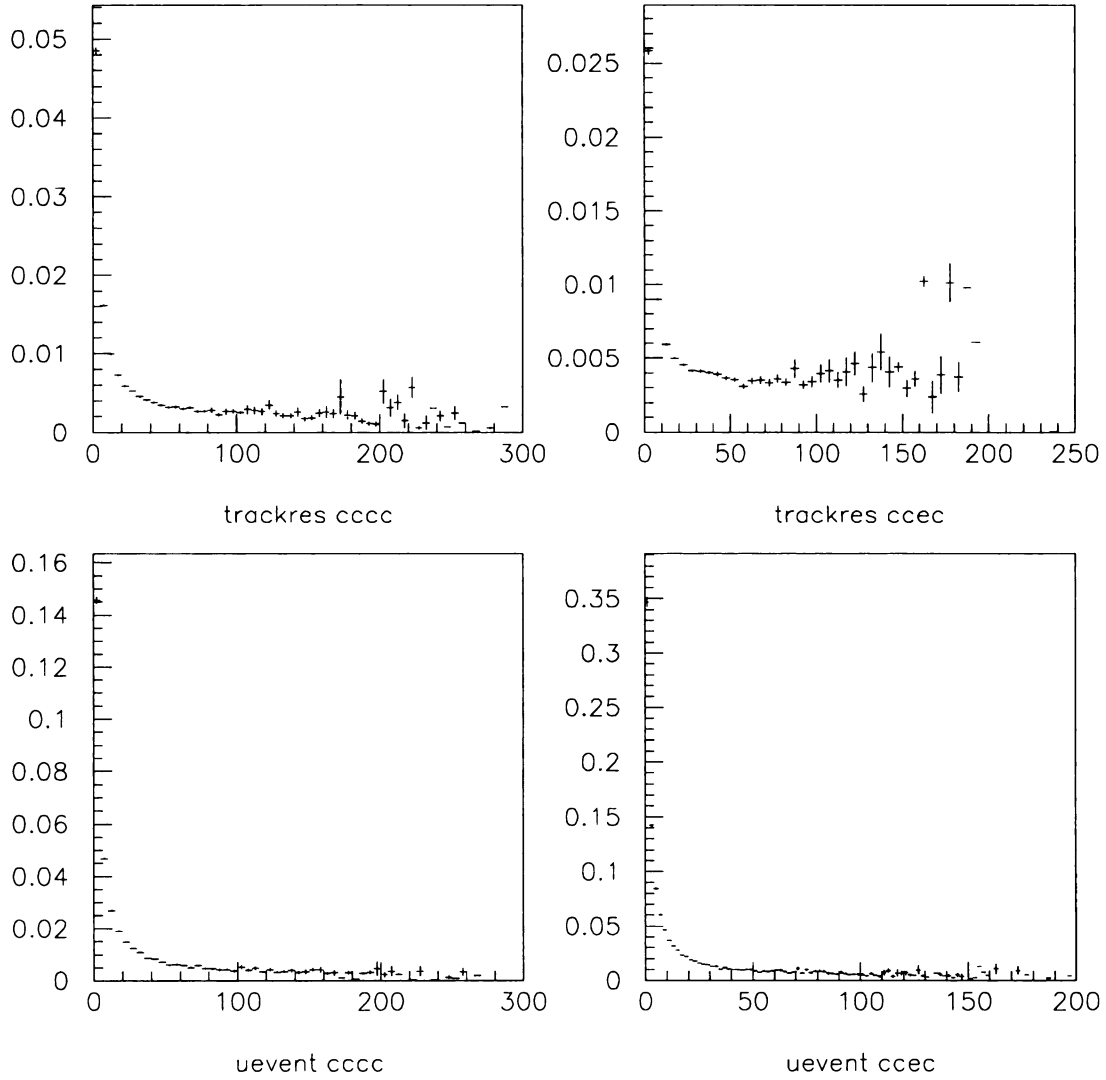


Figure 3.6: $Z p_T$ absolute resolution dependence on track resolution and the underlying event contribution. The absolute resolution is plotted as a function of $Z p_T$.



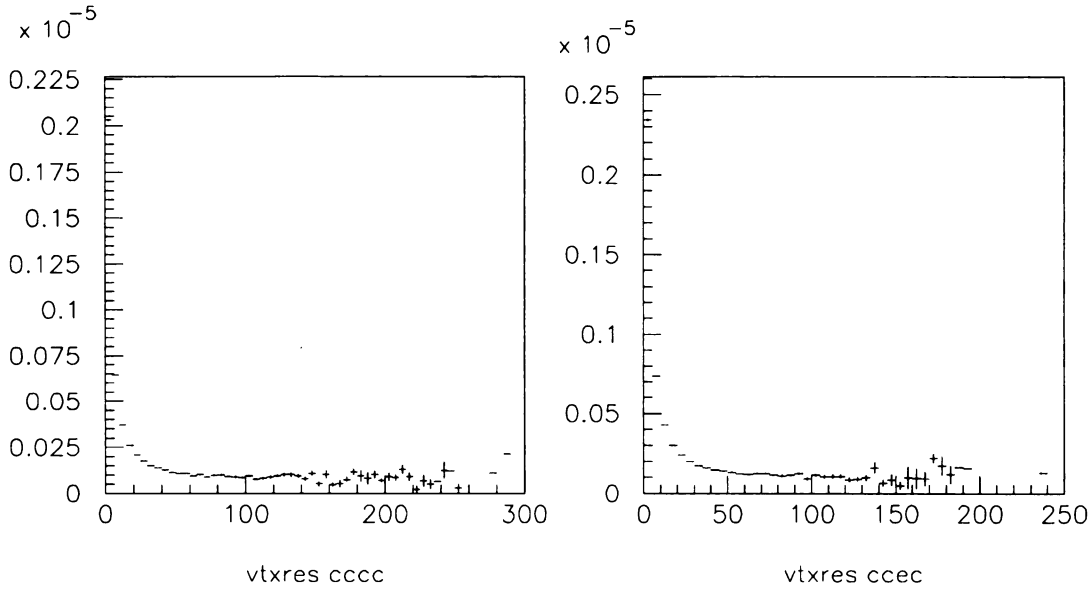


Figure 3.7: Effect of z vertex resolution on $Z p_T$ absolute resolution. The absolute resolution is plotted as a function of $Z p_T$.

3.3 Development of Fast Smearing Program

One final piece needed for the $Z p_T$ analysis was to study the smearing effects at the high p_T range of the distribution. In order to do this, it was necessary to see the difference in smeared distributions from different input theoretical distributions with various parameter values. This study was not feasible with the CMS Monte Carlo used in the previous studies because it could not produce the necessary statistics in a timely fashion as this is a region of very small cross section. Therefore, a new specialized smearing program was developed. The aim of this code was to smear the $Z p_T$ distribution alone and do it much faster than the CMS Monte Carlo, but also to produce a smeared distribution consistent with the more sophisticated CMS.

It was decided that the best way to produce a faster smearing code consistent with CMS would be to parameterize the smeared output from CMS. A distribution of (smeared p_T - unsmeared p_T) vs. unsmeared p_T from CMS was made. This distribution

100
90
80
70
60
50
40
30
20
10
0

00

00

000000

was separated into slices of the unsmeared p_T . Then each slice was fit to a double Gaussian shape. Since a $Z p_T$ distribution has high statistics only at low p_T , CMS could never achieve enough high p_T statistics needed for fitting with the computing power available. As an alternative, a fake distribution of p_T vs. y , shown in Figure 3.8, was devised as an input to CMS. It consists of bands spaced over the p_T axis, each band having the same area and shaped to have the correct rapidity distribution for a Z particle. The bands are spaced 1 GeV apart in the range 0 to 20 GeV p_T , and then are spaced 20 GeV apart thereafter. The finer spacing at low p_T was used because it was previously found that the fit parameters change more in that range. Once this distribution was used as the input distribution to CMS, it was found that the smeared distribution indeed had enough statistics to be fit to double Gaussians.

After the double Gaussian fits were performed, the fit parameters: normalization, sigma, and mean were plotted versus p_T (Figure 3.9). It was noticed that the mean values were negligible over all p_T values and were subsequently taken to be 0. Plotting also revealed that one of the Gaussians (labeled “2” in the plots) became insignificant compared to the other Gaussian above 200 GeV p_T . The values for the Gaussian widths were fit to lines and the relative normalization was fit to a constant.

The fast smearing program, SMEAR_PT, was designed to pick a random p_T value based on an input $Z p_T$ distribution, then to choose a random offset and add this to the p_T value to produce a smeared p_T value. The random offset was calculated by picking a random number from a double Gaussian distribution (single Gaussian if p_T was greater than 200 GeV). The parameters for the double or single Gaussian were chosen by using the fit values to the CMS smeared distribution.

The smeared distribution from SMEAR_PT compared to CMS is shown in Figure 3.10. Although the peak for the distribution from SMEAR_PT is somewhat higher, the two histograms match up well at higher p_T .



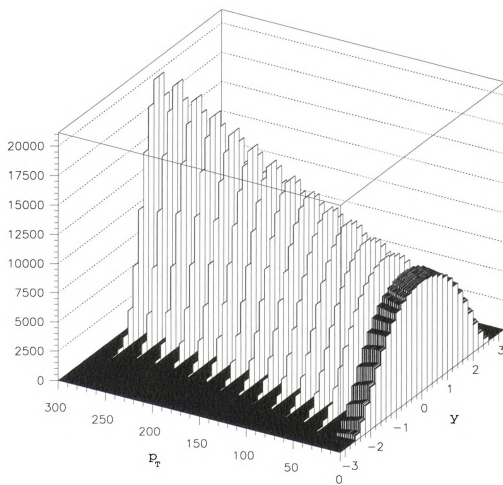


Figure 3.8: Special input distribution to CMS.



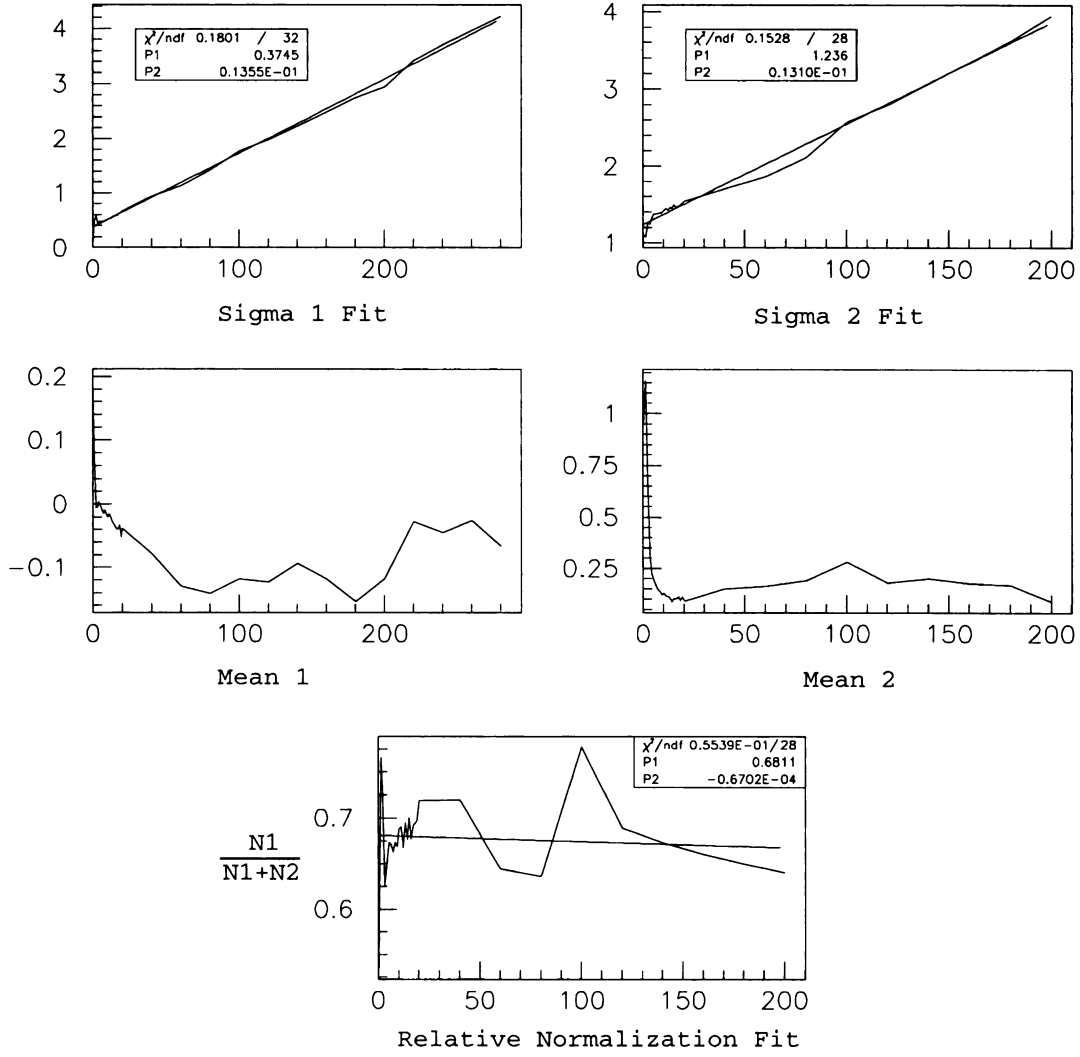


Figure 3.9: Fit parameters plotted versus p_T .



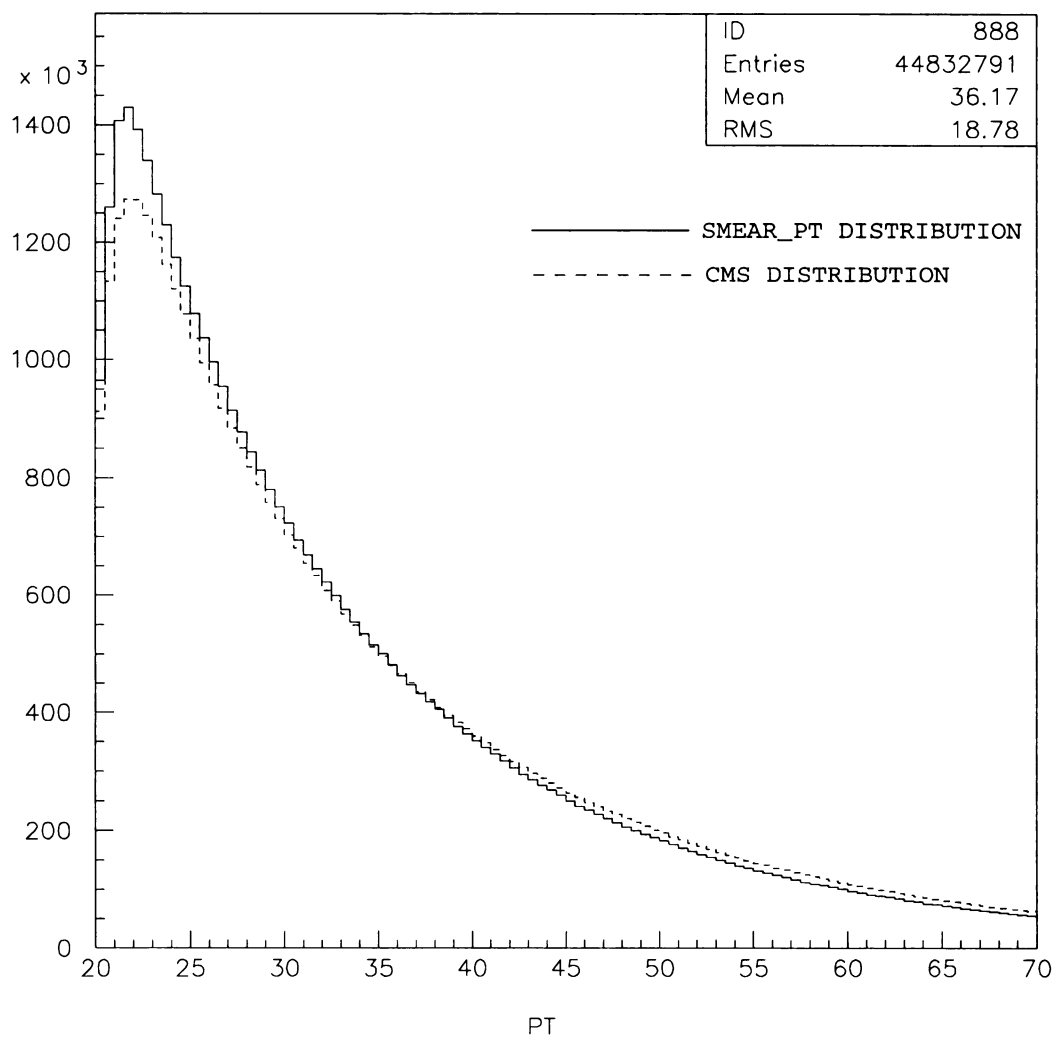


Figure 3.10: CMS smeared and SMEAR_PT smeared distributions.



Chapter 4

Non-Perturbative QCD Fits

4.1 Method of Fitting

In order to perform fits to the non-perturbative parameters a method was needed to calculate the theoretical cross section distributions by the non-perturbative + resummed method described in subsection 1.2.4. This calculation was made using the LEGACY program written at MSU. LEGACY is able to generate triple differential cross sections in the form $\frac{\partial\sigma}{\partial p_T \partial y \partial Q^2}$ for W 's, Z 's, photons, and Higgs particles for both fixed target and collider experiments. It can make this calculation for any input p_T , rapidity, and center of mass energy, E_{CM} . In addition, the calculation can be made with any choice of PDF and non-perturbative function.

The first step in the fitting process was to produce tables, or grids, of these cross sections for a range in p_T values and g parameter values of the non-perturbative function. Such grids were made for each experiment to be included in the fitting. After these grids were produced by LEGACY, a Jacobian transformation would be performed on the grids if the experimental data was not in the same form as the LEGACY cross section.

Once these grids were made, a fit could be performed for the non-perturbative parameters. This was done by a χ^2 minimization with a FORTRAN program linked to the CERNLIB routine MINUIT [30]. The grids provided the theoretical calculation.

Since MINUIT requires the function it fits to be continuous in the fit parameters, interpolations were made between grid points using another CERNLIB routine, DIVDIF [31].

Initially, it was important to fit over the largest feasible g parameter space in order to find the best possible minimum. The limitations on this coverage were due to finite computational speed and the fact that the non-perturbative function only produces physically reasonable cross section values in a limited region of the g parameter space. Producing a set of grids for a global fit could take 6+ hours of running on several VAX 4000 workstations. Therefore the initial fit would be with grids coarsely spaced in g space. The coarse grids, unless stated otherwise, ranged from 0.03 to 0.93 for g_1 , 0.05 to 1.0 for g_2 , and where applicable, -2.0 to 3.0 for g_3 . In some cases after a minimum was found with coarse grids, finer spaced grids were produced which were centered around the minimum found with the coarse grids and the fit was repeated. This was done to reduce any potential error due to interpolation. In some cases this step was repeated with yet a third set of grids with finer spacings than the second grid set. The spacings for all finer spaced grids varied on a fit-by-fit basis.

4.2 Experiments Included in Fits

In order to test that a model is truly universal for all Drell-Yan type processes, it was important to choose a set of data from a variety of experiments with different values of τ , center of mass energies, and different boson masses. Of the data used in the fits, three were from collider experiments and two from fixed target experiments. The collider experiments included the R209 [32], CDF Z [33][34] and the DØ Z [27] data. Fixed target data were used from both the E288 [35] and E605 [36] experiments. The p_T bins used from each experiment were chosen to be in the range that the non-perturbative functions have an effect on the cross section, $p_T < Q$, and to provide enough data points for fitting.

1911

1912

1913

1914

1915

1916

1917

1918

1919

1920

1921

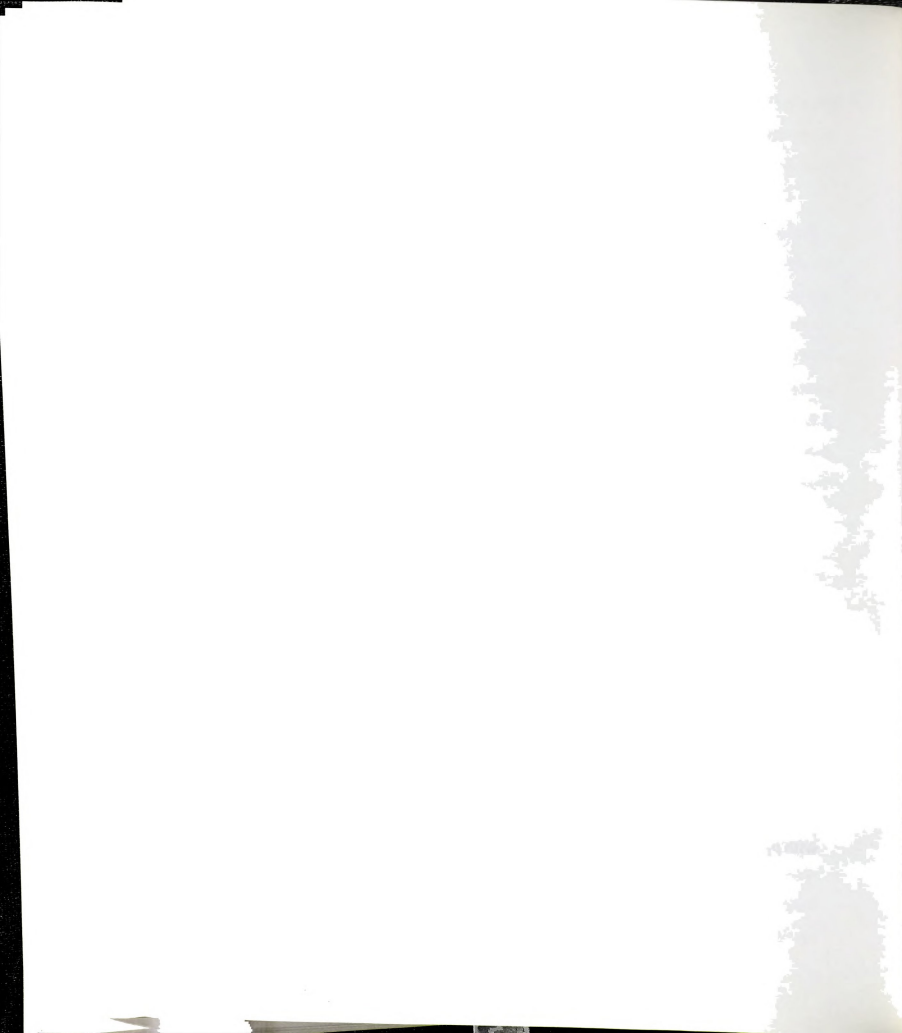
Experiment	CM ENERGY (GeV)	τ Range	Boson Mass (GeV)	PROCESS
R209	62.0	0.007-0.031	5-11	$p+p \rightarrow \mu^+\mu^-+X$
CDF Z	1800.0	0.003	91.19	$p+pbar \rightarrow Z$
DØ Z	1800.0	0.003	91.19	$p+pbar \rightarrow Z$
E288	27.4	0.033-0.110	5-9	$p+Cu \rightarrow \mu^+\mu^-+X$
E605	38.8	0.033-0.054 0.073-0.22	7-9 10.5-18	$p+Cu \rightarrow \mu^+\mu^-+X$

Table 4.1: Experiments included in global fits with some properties for the data used in the fits.

4.2.1 R209

The R209 experiment was based at the CERN Intersecting Storage Rings, (ISR), a proton-proton collider. The total $\sqrt{s} = 62$ GeV data set contains 7827 events with an integrated luminosity of $1.12 \times 10^{38} \text{ cm}^{-2}$. The R209 data also contains an overall normalization error of 10%.

Only a subset of R209's total data sample was actually used in fitting. The $\sqrt{s} = 62$ GeV data, and not the $\sqrt{s} = 44$ GeV data, were chosen for inclusion in the fits because the lower energy data have much lower statistics. Of this data set, the two bins with photon mass ranges of $5 \text{ GeV} \leq Q \leq 8 \text{ GeV}$ and $8 \text{ GeV} \leq Q \leq 11 \text{ GeV}$ were included. Since only the non-perturbative region was of interest, only the data points with $p_T \leq 1.8 \text{ GeV}$ were used.



To compare the cross sections of LEGACY directly to the published data, the LEGACY cross sections had to be transformed into the same form as the data, $\frac{\partial\sigma}{\partial p_T^2}$.

The steps taken to make the transformation are as follows:

1. Numerically integrate over rapidity to convert $\frac{\partial\sigma}{\partial p_T \partial y \partial Q^2}$ into $\frac{\partial\sigma}{\partial p_T \partial Q^2}$.
2. Divide by $2p_T$ to place the cross section into the form $\frac{\partial\sigma}{\partial p_T^2 \partial Q^2}$.
3. Separately integrate over the range of each mass bin to remove the dependence on Q^2 .

Each mass bin was integrated by having several identical grids with different photon masses covering the range of the mass bin. A numerical integration was then performed for each $\frac{\partial\sigma}{\partial p_T^2 \partial Q^2}(p_T, g_1, g_2, \dots)$. For example, for the integration over the 5-8 GeV mass bin there were identical grids produced using photon mass values of 5.0, 5.5, 6.0, 6.5, 7.0, 7.5, and 8.0 GeV. $\frac{\partial\sigma}{\partial p_T^2 \partial Q^2}(p_T, g_1, g_2, \dots)$ values for each of these masses were then used in a numerical integration of Q^2 to obtain $\frac{\partial\sigma}{\partial p_T^2}(p_T, g_1, g_2, \dots)$ values.

4.2.2 CDF

The CDF Z data come from the first collider detector at Fermilab located in the Tevatron ring. There are actually two data sets used in the fitting. One data set was taken from the 1988-89 accelerator run, (Run 0). The second data set was from the more recent 1992-1995 (Run 1) accelerator running. The older data set, with an integrated luminosity of 4.05 pb^{-1} , has many fewer events than the more recent results from CDF and DØ. This earlier data set has 290 events with $p_T \leq 23 \text{ GeV}$, the p_T range used in the fits. The more recent data set has an integrated luminosity of 110 pb^{-1} .

Since the data were published in the form $\frac{\partial\sigma}{\partial p_T}$, it was relatively simple to transform the LEGACY cross section into this form. The Q^2 dependence disappears since it is a constant, namely the square of the Z mass. The only necessary step was to numerically integrate over rapidity.

4.2.3 E288

E288 was a fixed target experiment located at Fermilab. The data which were used from this experiment came from a 400 GeV proton beam impacting a copper target and producing virtual photons which convert into dimuon pairs. From the published data, a subset was chosen for inclusion into the fitting. In most cases, the data from 5 to 9 GeV in photon mass were fit, though in some instances data from the higher mass bins (9-14 GeV) were also included. These higher mass data have much larger fractional errors than the low mass data and so did not effect the fitting as significantly. In order to confine the fitting to the non-perturbative regime, only the seven lowest p_T bins ($p_T \leq 1.4$ GeV) were included. The overall normalization error for the data is listed at 25%.

In order to match the data, the following relation was used to convert the LEGACY cross sections into invariant cross sections:

$$E \frac{d^3\sigma}{dp^3} = \frac{1}{2\pi p_T} \frac{d\sigma}{dp_T dy}. \quad (1.17)$$

With this relation, the following steps were performed to make the transformation:

1. Divide the grid cross section by $2\pi p_T$.
2. Numerically integrate over Q^2 .

4.2.4 E605

The E605 experiment, like E288 was a fixed target detector located at Fermilab, though the E605 experiment took its data at a later time. Again like E288, the data consist of dimuon pairs produced from a proton beam colliding with a copper target. In this case, however, the proton beam energy was 800 GeV. The data set included in the fits covered the mass ranges of 7.0-9.0 GeV and additionally 10.5-18.0 GeV in some cases. In order to stay within the non-perturbative regime, the seven p_T bins below 1.4

GeV were used. These data points had an overall normalization uncertainty of 15% and a point-to-point systematic error of 10% in addition to the statistical errors. The Jacobian transformation used for E605 is identical to the transformation used for E288 because the E605 data were also published as invariant cross sections.

4.3 Choice of Non-Perturbative Functions

Because there is as yet little theoretical basis for the form of the non-perturbative function, fits were made with several functions. One of the functions chosen was the DWS parameterization (Equation 1.30). Fits using this parameterization will hereafter be referred to as “2 parameter fits.” The function from the LY parameterization (Equation 1.31) was also used in fitting. Still a third function, given in the equation below, was also tried in some fits,

$$\text{Gauss 1:} \quad -g_1 b^2 - g_2 b^2 \ln\left(\frac{Q}{2Q_0}\right) - g_1 g_3 b^2 \ln(100x_a x_b). \quad (4.1)$$

This new parameterization is similar to the LY function, but it yields a pure Gaussian shape in terms of the b parameter.

Another purely Gaussian parameterization was also tried,

$$\text{Gauss 2:} \quad -g_1 b^2 - g_2 b^2 \ln\left(\frac{Q}{2Q_0}\right) - g_1 g_3 b^2 (x_a + x_b). \quad (4.2)$$

However this function was found not to match the data well in initial fits and so was discarded.

100%

90%

80%

70%

60%

50%

40%

30%

20%

10%

0%

100%

90%

80%

70%

60%

50%

40%

30%

20%

10%

0%

100%

90%

80%

70%

60%

50%

40%

30%

20%

10%

0%

4.4 Preliminary Fits

The numerous fits which were performed are described in chronological order in this section and in the following two sections. A table summarizing all of the fits in this chapter, Table 4.12, is given on pages 87-89. This section describes the results of global fitting to data predating Run 1 Tevatron Z results. A portion of this work has been accepted for publication [37] and is reprinted in Appendix C.

4.4.1 Duplication of Original LY Fitting

Before the $D\bar{D}$ data became available, studies were done to isolate the effects of such things as the PDF used and normalization uncertainties from other experiments. The first of these fits, labeled Fit A, was a duplication of the Ladinsky Yuan fit [24], with the LY parameterization (Equation 1.31). This was done primarily as a double check on the latest version of LEGACY as well as the fitting code. The fit involved data from the R209 experiment ($5 \text{ GeV} \leq Q \leq 8 \text{ GeV}$), the CDF Z Run 0 data, and the E288 experiment ($6 \text{ GeV} \leq Q \leq 8 \text{ GeV}$). The original LY fit actually consisted of two steps. The first step was a fit to g_2 using the R209 and CDF Z data. Then, with the R209 and E288 data, a fit was performed for g_1 and g_3 with g_2 fixed at the value from the first step. The three parameters were not simultaneously fit at the time because of limitations in computing power and also because it was thought that the higher statistics E288 data would cause the important data at smaller τ to be neglected. These fits were done using the CTEQ2M PDF [38] to calculate cross sections. Equation 4.3 lists the fit values from the original LY fit.

$$g_1 = 0.11^{+0.04}_{-0.03}, g_2 = 0.58^{+0.1}_{-0.2}, g_3 = -1.5^{+0.1}_{-0.1} \quad (4.3)$$

1.1.1.1.1

1.1.1.1.1

1.1.1.1.1

1.1.1.1.1

1.1.1.1.1

1.1.1.1.1

1.1.1.1.1

It was later found that a FORTRAN error in the description of the neutron quark density in the original LEGACY resulted in an incorrect published value of g_1 and g_3 . This error affected only calculations for fixed heavy target experiments so that the g_2 value should not have been affected. Equation 4.4 shows the value from refitting. This refitting resulted in a value of g_2 which is consistent with the original LY fit.

$$\text{Fit A:} \quad g_1 = 0.05, g_2 = 0.57, g_3 = 0.83 \quad (4.4)$$

The next fit, Fit B, was identical to the previous fit with the exception that CTEQ3M [39] was used to calculate the cross sections. Comparing the results of this fit to that of the previous fit gives a measure of the effect of two particular PDF's. Equation 4.5 shows the values obtained with CTEQ3M. It can be seen that there is about a one to two sigma difference in g_2 and a significant change in g_3 . This lends credence to the assertion that it is only valid to use non-perturbative fit values in a calculation with the PDF used to obtain those fit values.

In order to more easily compare fits to each other, all subsequent fits were done using CTEQ3M.

$$\text{Fit B (LY function):} \quad g_1 = 0.08, g_2 = 0.47, g_3 = 1.6 \quad (4.5)$$

As a test of the difference between parameterizations, the same fit was done with the Gauss 1 parameterization and that fit resulted in the values below. As expected, the g_2 value did not differ from the LY parameterization's value, however there is a significant difference in the g_3 values. The slight change in the g_1 values is due to the coupling between g_1 and g_3 .

$$\text{Fit B (Gauss 1):} \quad g_1 = 0.11, g_2 = 0.47, g_3 = 0.61 \quad (4.6)$$

Parameter	Value
g_1	0.15
g_2	0.40
g_3	-0.84
R209 Norm	0.99
E288 Norm	1.47

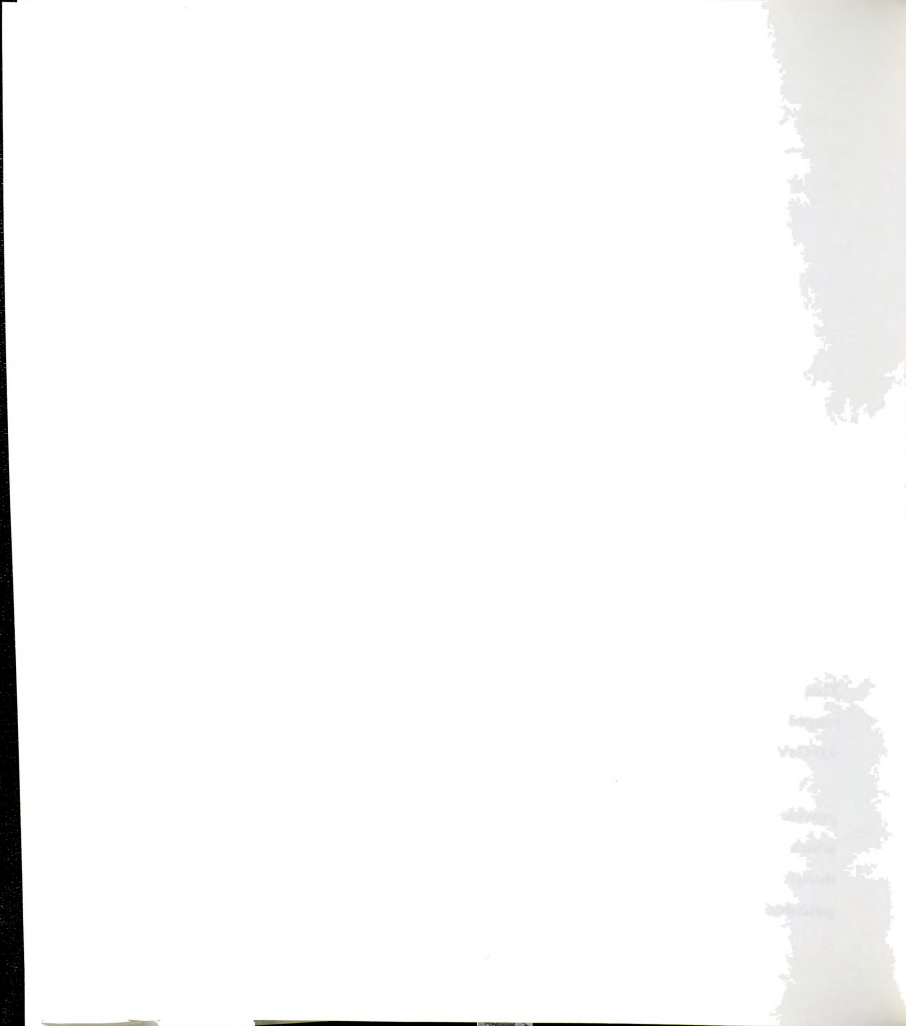
Table 4.2: Fit C values using experimental data from R209, E288, and CDF Z.

4.4.2 Simultaneous Fitting of All Parameters

The next issue confronted was in the mechanics of the fitting itself. Here, Fit B was repeated with the exception that all three g parameters were fit simultaneously. In addition, the normalizations for both the R209 and E288 data set were included as fit parameters due to the large uncertainty quoted in the published data. The values for Fit C are given in Table 4.2. Note that the fit to the E288 normalization is 47% away from the central value, which is well outside the 25% error range.

Data from E605 and additional E288 data were included in Fit D, the next fit. This was the only change from the Fit C data set. The E605 data included in the fit ranged in 7.0 to 9.0 GeV in boson mass. The E288 data was extended to include 5.0 to 9.0 GeV in boson mass. Fits were performed with the LY, DWS, and Gauss 1 functions.

From an examination of the χ^2 per degree of freedom, the Gauss 1 fit appears to provide a better fit than the other parameterizations. The Gauss 1 fit is also the only one which results in a normalization for E605 which is within the published error range, though all three fits resulted in normalizations for E288 which were outside of its published error range.



Parameter	LY Function	DWS Function	Gauss 1
g_1	0.16	0.18	0.21
g_2	0.34	0.27	0.47
g_3	-0.41	0.00	-0.51
R209 Norm	1.02	1.05	0.93
E288 Norm	1.39	1.29	1.31
E605 Norm	1.28	1.25	1.15
χ^2 /dof	2.18	2.18	1.65

Table 4.3: Values for Fit D for three parameterizations.

The next fit done used the LY function and added some higher mass E605 data to the data of the previous fit. Table 4.4 lists the range of each experiment's data included in Fit E. It was noticed that again the fit results in a normalization outside the given 25% error range for E288. Table 4.5 also shows that the fitted E605 normalization also ended up outside of the 15% error range of the published value.

Due to the inability to obtain fits which describe the data within the bounds published by the experiments, it was decided to test the behavior of the fits if E288 was removed in the next fit, Fit F. E288 was singled out because of the inability to produce a consistent fit to its normalization in Fits C, D, and E. There were also indications that the CTEQ collaboration had problems when including E288 in its global PDF fits [40]. Since E605 provides higher statistics data with the same process as E288 and a similar center of mass energy, there would be no loss to the diversity of the data set.

Experiment	P_T RANGE (GeV)	BOSON MASS RANGE (GeV)
R209	0.0-1.8	5.0-8.0
CDF Z	0.0-22.8	81.0
E288	0.0-1.4	5.0-9.0
E605	0.0-1.4	7.0-9.0, 10.5-18.0

Table 4.4: Data set of fit including extended E605 data set, Fit E.

Parameter	Value
g_1	0.17
g_2	0.30
g_3	-0.20
R209 Norm	1.04
E288 Norm	1.35
E605 Norm	1.30

Table 4.5: Fit results for Fit E.



Parameter	Value	Uncertainty
g_1	0.15	-0.03,+0.04
g_2	0.48	-0.05,+0.04
g_3	-0.58	-0.20,+0.26
R209 Norm	0.96	N/A
E605 Norm	1.14	N/A

Table 4.6: Fit for LY parameterization excluding E288, Fit F.

As well as discarding E288, data in the 8-11 GeV mass range from R209 was added. Only the 7-9 GeV mass range from E605 was included in the global data set. These steps were made with the purpose of balancing the amount of large and small τ data. In addition to the LY parameterization, fits were performed using the DWS and Gauss 1 parameterizations. However, fitting with the Gauss 1 parameterization using fine grids resulted in multiple minima of the same χ^2 rather than a single minimum. In other words, there were many values for the fit parameters which fit the data equally well. This suggests that the data set used was not adequate to differentiate among theory curves with different fit parameters and that additional data would serve to pick out a single minimum.

Parameter	Value	Uncertainty
g_1	0.24	-0.07,+0.08
g_2	0.34	-0.08,+0.07
g_3	0.00	N/A
R209 Norm	0.96	N/A
E605 Norm	1.06	N/A

Table 4.7: Fit for DWS parameterization excluding E288, Fit F.

With this new data set, the normalizations in Fit F now fall within the quoted experimental error ranges for both the LY and DWS parameterizations. For this fit, an analysis was also done in order to calculate the uncertainties on the g values. For the DWS parameterization, a contour at $1+\text{minimum } \chi^2$ was plotted versus g_1 and g_2 (Figure 4.1). The upper and lower uncertainty values for the g_i parameter were determined to be the upper and lower g_i extremes on the contour. The LY parameterization is more complicated because of the correlations among the three g parameters. It was decided that the uncertainties would be calculated by fixing each g parameter, one at a time, at its best fit value, and then producing a contour at $1+\text{minimum } \chi^2$ with the other two g parameters on the x and y axes. The uncertainty for those two parameters would then be determined exactly as was done with the 2 parameter fit. These contours are shown in Figure 4.2.

Though the fit did not include E288, a comparison was done to the data using the g values from Fit F of both parameterizations. In Figure 4.3 it can be seen that the calculation matches the data well. Also of note is that both parameterizations are indistinguishable in the plot.



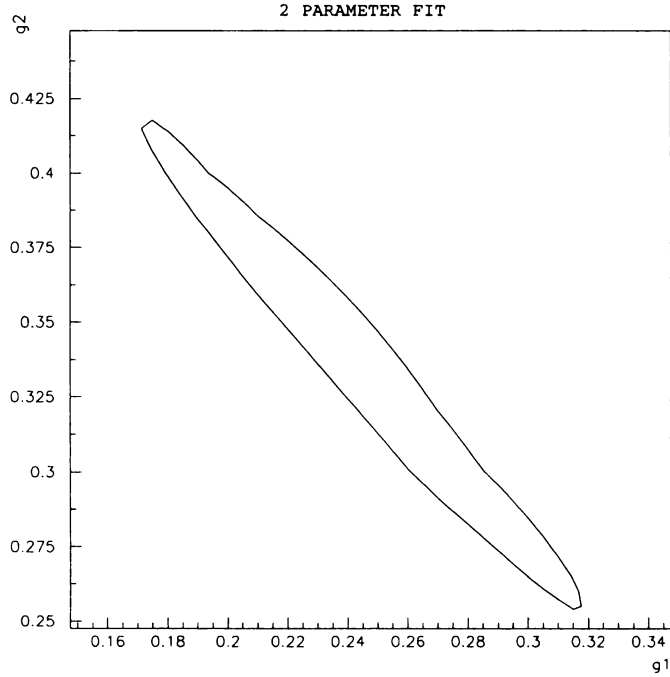
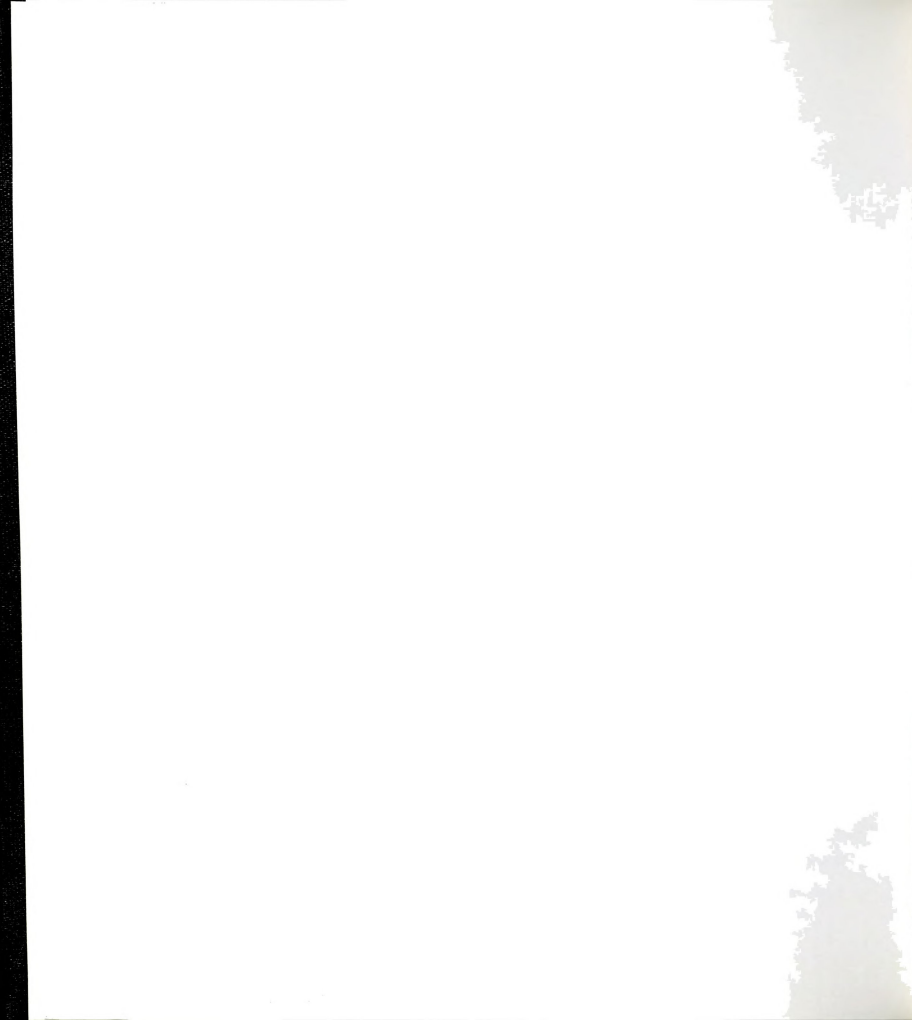


Figure 4.1: Contour of $\chi^2 + 1$ for 2 parameter fit, Fit F.

However, comparing p_T distributions derived from the LY parameterization to distributions made from the DWS parameterization for CDF Z reveals something interesting. Figure 4.3 shows the calculated fit distributions compared to the experimental data included in the fit. All the plots except the CDF plot show the two theory curves to be identical. For the CDF plot, there is a noticeable difference at the peak, suggesting that more precise Tevatron Z data would be able to differentiate between the two parameterizations.



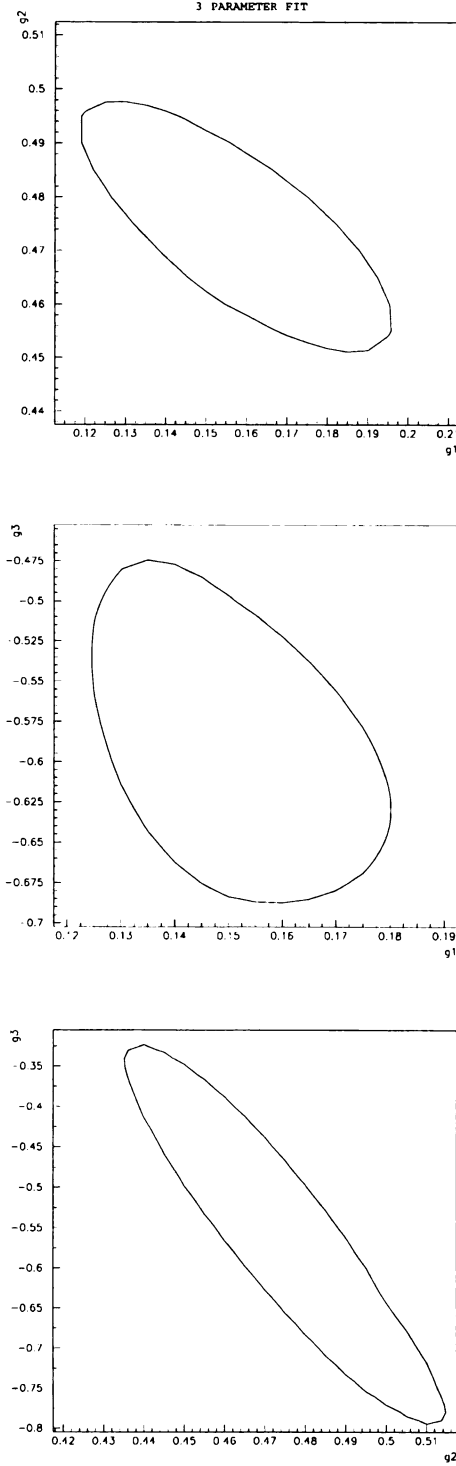


Figure 4.2: Contours for determining uncertainties for Fit F with the LY parameterization. These plots were made with fixed g_3 , g_2 , and g_1 respectively at their values at the minimum.



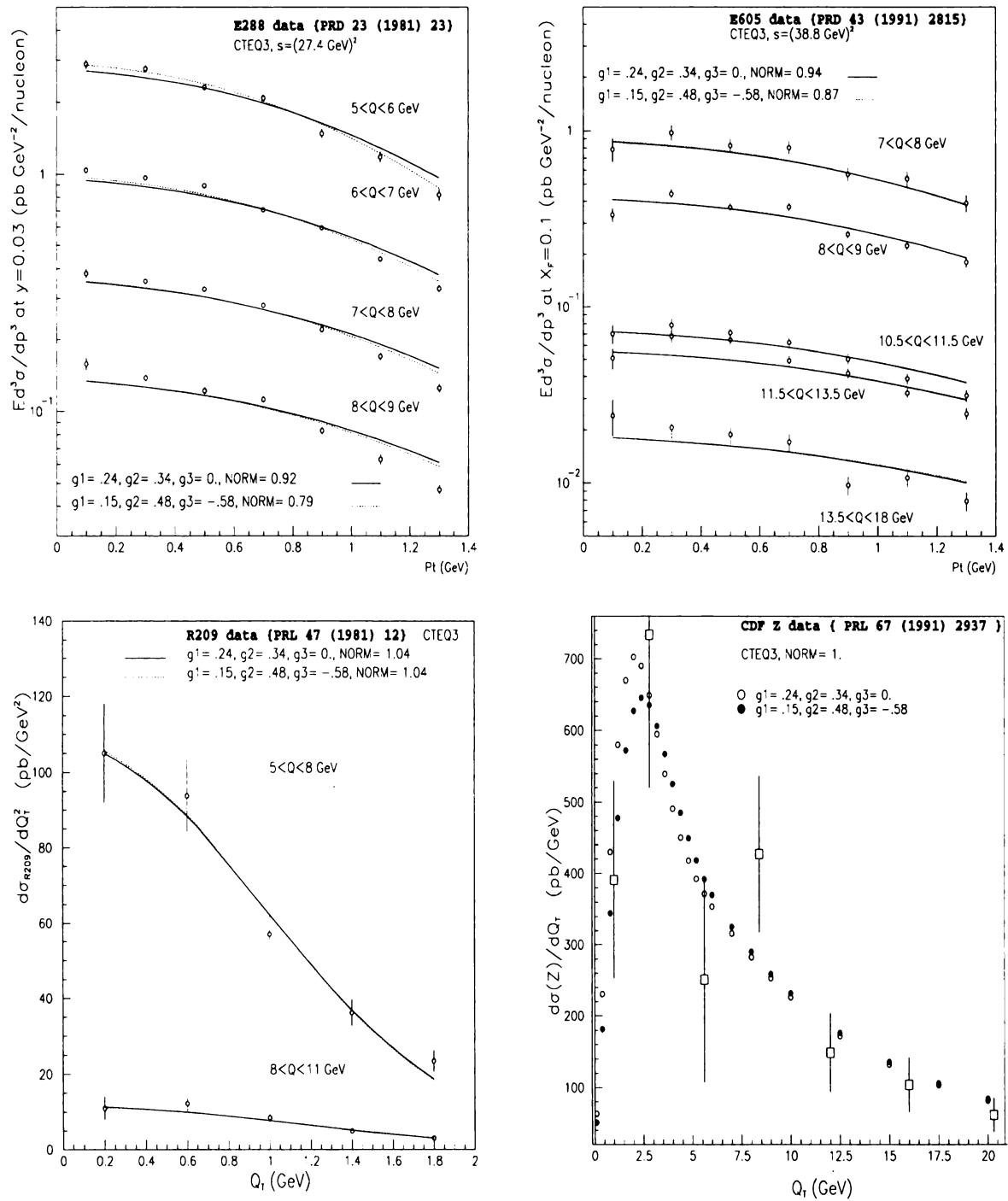
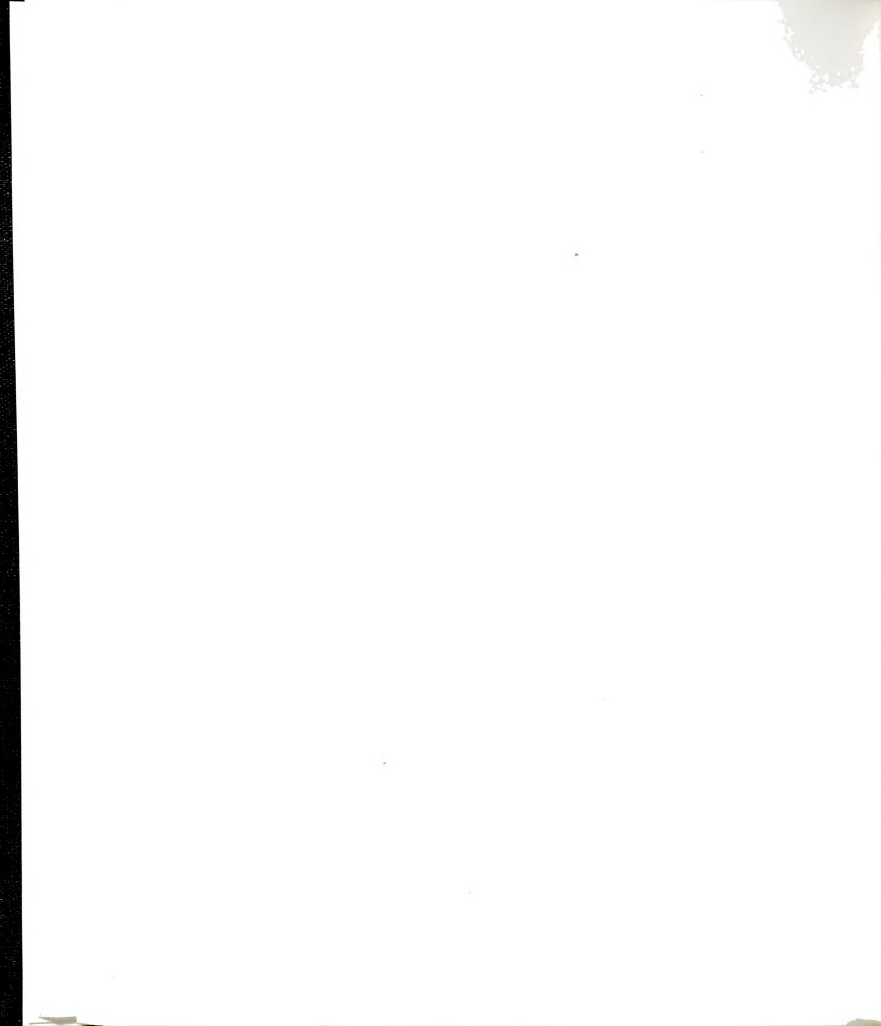


Figure 4.3: Plots of LY and DWS parameterization curves superimposed with data. Note that the NORM values given here are applied to the theoretical curves and are therefore reciprocals of the values given in Table 4.6 and Table 4.7.



Parameter	LY Function	DWS Function	Gauss 1	Gauss 3
g_1	0.05	0.03	0.05	0.05
g_2	0.72	0.76	0.80	0.80
g_3	-2.50	0.00	-2.50	-2.50
R209 Norm	0.93	0.92	0.89	0.89
CDF Run 1 Norm	0.88	0.89	0.89	0.90
D0 Z Norm	0.99	1.00	1.00	1.00
E605 Norm	1.05	0.88	0.94	0.94
χ^2 /dof	1.15	1.30	0.88	0.88

Table 4.8: Results for global fit including DØ and CDF Run 1 data, Fit G.

4.5 Inclusion of Tevatron Run 1 Z Data

At the beginning of year 2000 both the DØ and CDF collaborations made available new distributions of Zp_T data taken during Run 1 at Fermilab. Both data sets have high statistics which would counter balance the high statistics E605 data in any global fitting. The new CDF and DØ data were then added to the global set used in Fit F and fits were performed for the DWS, LY, and Gauss 1 parameterizations as well as a new parameterization, Gauss 3, described in subsection 4.5.3. The normalizations for both of these data sets were fit in all of the parameterizations. The fit values for all the parameterizations with this data set, Fit G, are given in Table 4.8.



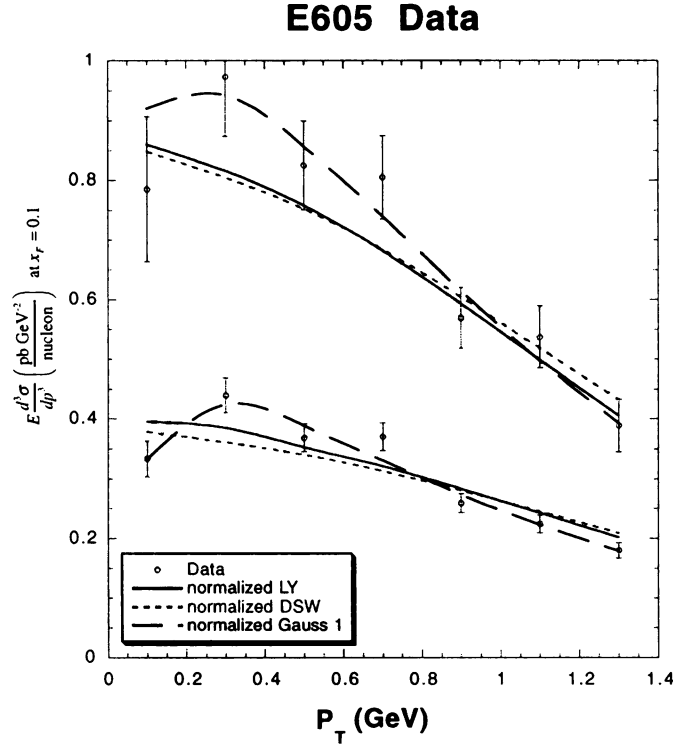


Figure 4.4: Gauss 1 fit distribution for E605.

4.5.1 Gauss 1 Fit

Fit G performed with the Gauss 1 parameterization was found to have a significantly lower χ^2 than both the LY parameterization and 2 parameter fits. Unfortunately this function had problems. First of all, it has the identical insensitivity to g_3 as the LY function fit (see below). Several minima were found which varied in g_3 from -2.0 to at least -3.0, the lower boundary of the grids. The minimum given in the table is for a g_3 of -2.5 because it is at the midpoint of the range in which minima were found. Also, the plot of the fit distribution versus the E605, Figure 4.4, data reveals that the distribution dips at low p_T . Perturbative QCD predicts that for an infinite boson mass, a $\frac{d\sigma}{dp_T^2}$ distribution should flatten out as p_T goes to 0 [11]. The judgement was made that the non-perturbative prediction should give the same behavior for finite mass values. Because of this theoretical prejudice and the g_3 insensitivity, this fit was discarded.

4.5.2 LY and DWS Parameterization Fits

Figure 4.5 shows the LY function fit and 2 parameter fit compared to the data. The plots of both of these fits match each other closely for all the experiments, the most noticeable exception being a difference in the peaks of the Tevatron Z plots. The g_1 value for both fits is very small, at or near the lower edge of the grid in g_1 . In fact, it was found that for the 2 parameter fit that a small, negative g_1 value was preferred by MINUIT. However, rather than a true minimum, there was a large set of g_2 values and negative g_1 values which gave equally good fits. In addition it was found that negative g_1 values caused a low p_T dip in the prediction curve for E605 like the ones seen for the Gauss 1 fit.

There were also some complications in fitting to the LY function. It was found that the lowest χ^2 occurs with g_3 values between -3.0 and -2.2. However, the χ^2 is very insensitive to the value of g_3 in this range. Many minima were found with nearly the same χ^2 , with g_3 values throughout the -3.0 to -2.2 range.

4.5.3 Gauss 3 Fit

After noticing that the fits for all three parameterizations result in a very small value for g_1 , it was thought that this could be a reason for the Fit G fits being insensitive to the g_3 value. With a small g_1 , the third term of the non-perturbative functions also becomes small. Therefore a large change in g_3 would be necessary to effect a change in the value of the non-perturbative function. It was decided to try a small variation on the Gauss 1 parameterization, so that g_1 would be eliminated from the third term:

$$\text{Gauss 3:} \quad -g_1 b^2 - g_2 b^2 \ln\left(\frac{Q}{2Q_0}\right) - g_3 b^2 \ln(100x_a x_b). \quad (4.7)$$

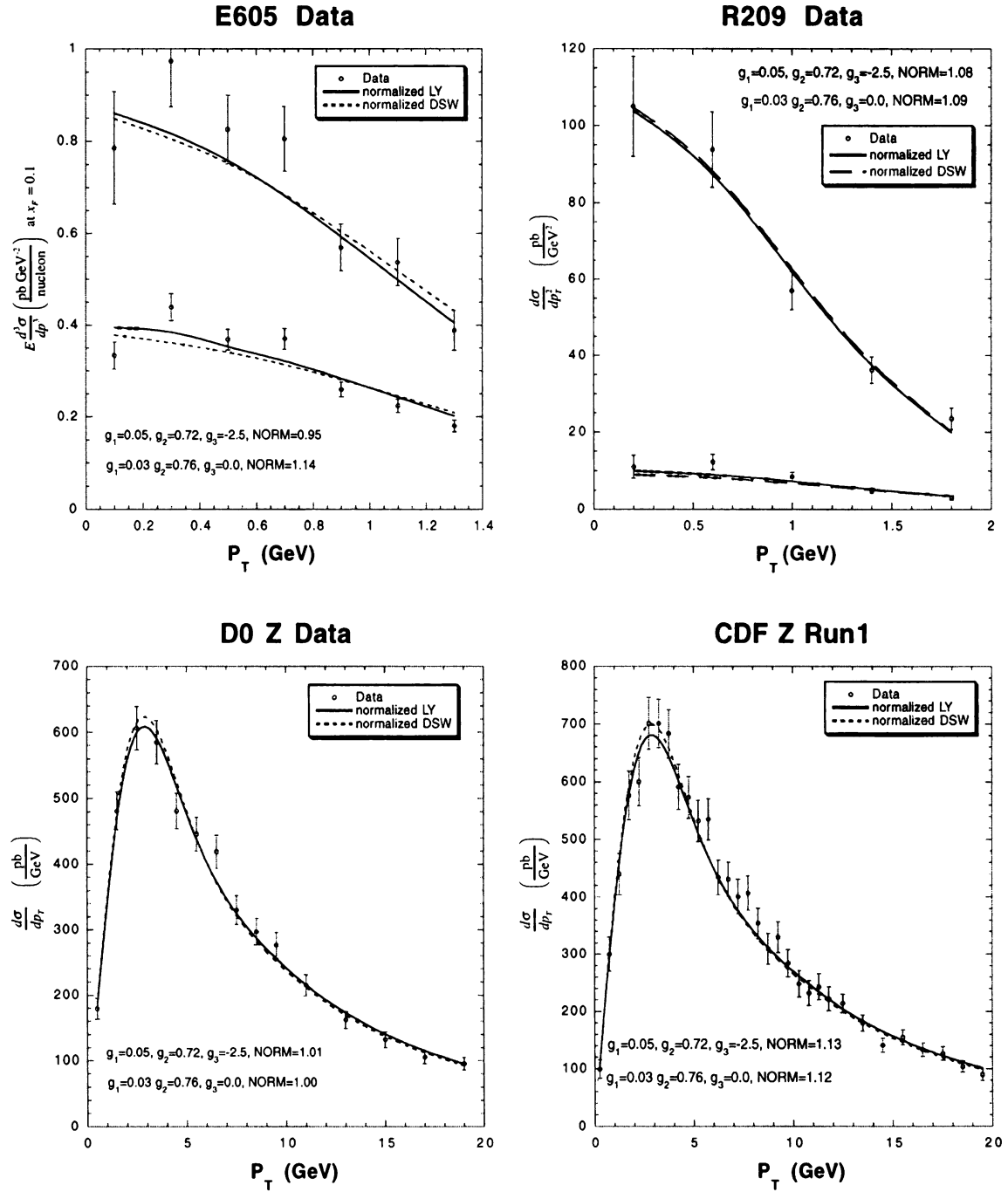


Figure 4.5: LY function and 2 parameter Fit G compared to each other. Note that the NORM values given here are applied to the theoretical curves and are therefore reciprocals of the values given in Table 4.8.



Unfortunately Fit G for this parameterization exhibited the same behavior as the Gauss 1 fit. It too found more than a single minimum between -2.0 and -3.0 in g_3 . The minimum included in the table is for a g_3 of -2.5 because it lies in the midpoint of the g_3 range of found minima. This fit also has the same dip at low p_T for the E605 curves observed for the Gauss 1 fit making this result undesirable.

4.6 Reintroduction of Drell-Yan Data

Eventually it was decided that the data set for Fit G was now overbalanced to the small τ data and that was possibly causing the insensitivity to g_3 and the very small g_1 . Therefore it was decided to first reintroduce the higher mass E605 data and finally data from E288 and examine the effects on the fits in steps.

4.6.1 Fitting with Higher Mass E605

The data set in Fit G already included the 7-8 GeV and 8-9 GeV E605 mass bins. In addition to the data used for Fit G, Fit H included three additional E605 mass bins, the 10.5-11.5, 11.5-13.5, and 13.5-18 GeV bins. Table 4.9 outlines the results for the different parameterizations.

The fit values for the DWS parameterization essentially do not change from Fit G to Fit H. Most notable is that this parameterization still retains the very small g_1 . The reduced χ^2 for this particular fit has increased from Fit G also. Examination of the fit for this function plotted against the data in Figure 4.6 reveals why its reduced χ^2 is larger.

This function does a poor job of fitting to the E605 data. The fit curves are outside the error bars for nearly all the data in the three highest mass bins. Also the fit curve for the second lowest mass bin shows the same type of low p_T dip as seen in the Gauss 1 Fit G result and so makes this fit undesirable for the same reasons.

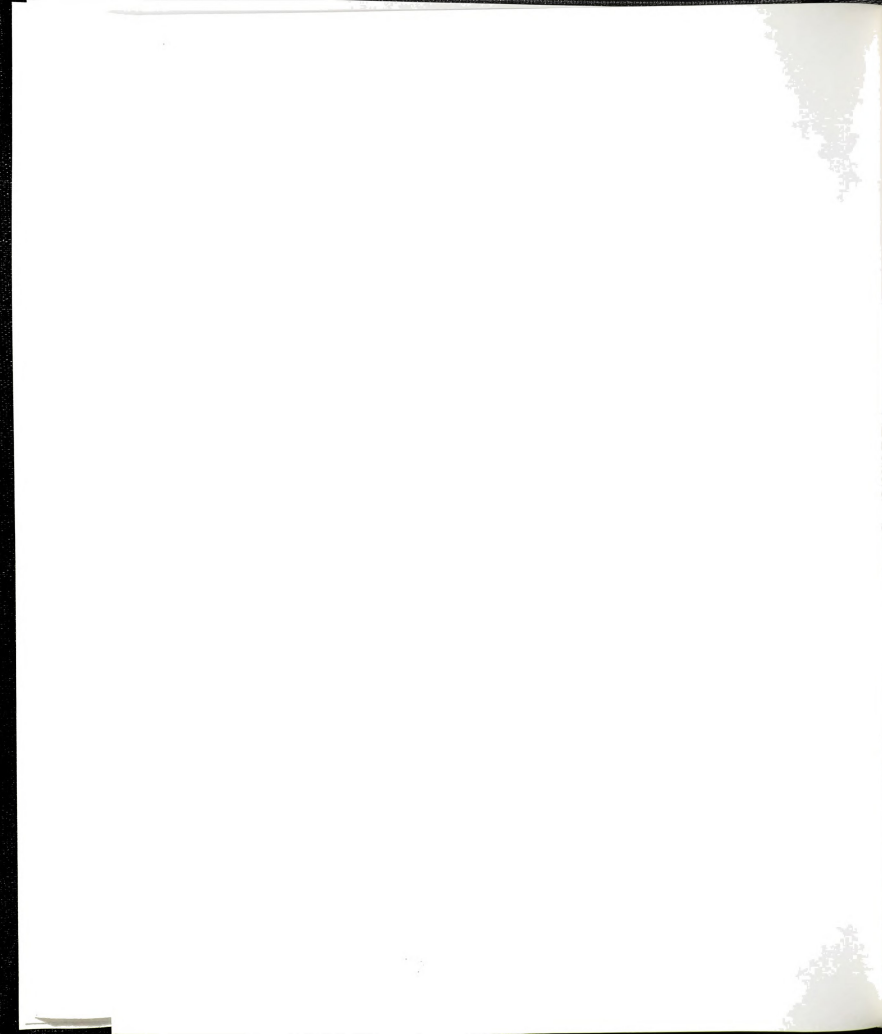
1000
1000
1000
1000
1000

1000
1000

Parameter	LY Function	DWS Function	Gauss 1
g_1	0.03	0.03	0.07
g_2	0.70	0.71	0.74
g_3	1.00	0.00	-2.00
R209 Norm	0.94	0.93	0.90
CDF Run 1 Norm	0.89	0.89	0.89
D0 Z Norm	1.00	1.00	1.00
E605 Norm	0.94	0.89	1.11
χ^2	180	194	101
χ^2 /dof	1.96	2.09	1.1

Table 4.9: Fit H results.

The fit for the LY function also has nearly identical values to Fit G numbers. There is however, a significant change for g_3 . Now, rather than a continuous range of equally acceptable g_3 values, this fit has only one best value for g_3 . Also the g_3 value is far from the -2.0 to -3.0 range of the previous fit. Like the fit to the DWS function, it also has a larger reduced χ^2 than its Fit G counterpart. The similarity between the two parameterizations continues in the plots. Fit curves for both of these functions are virtually identical for all the data.



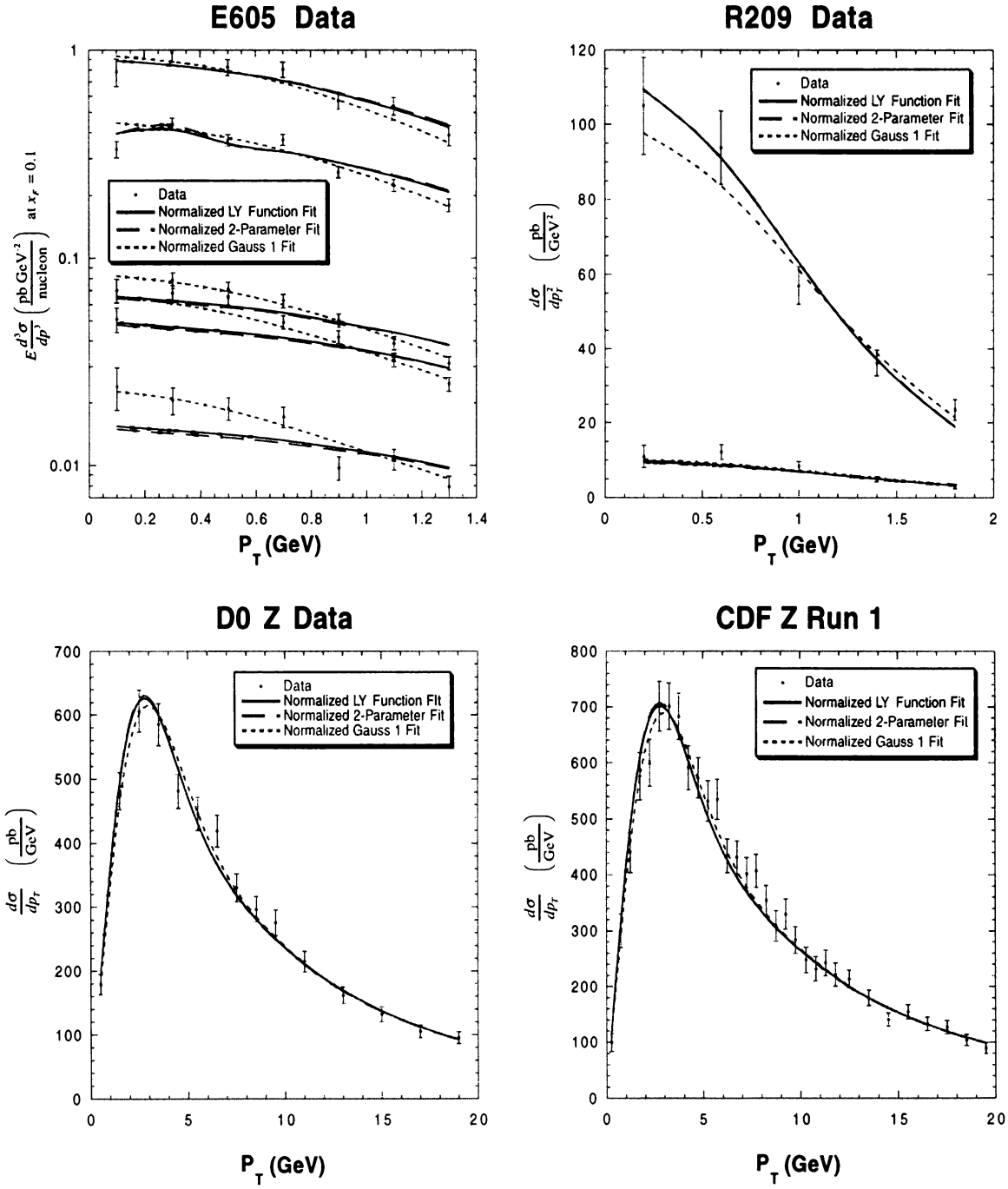


Figure 4.6: Plots of Fit H results compared to Data.



The fit to the Gauss 1 function also had its g_3 value fixed uniquely by the addition of the higher mass E605 data. However instead of mirroring the LY function values like it did in the previous fit, its g_3 value is very different. The reduced χ^2 for this function is the lowest of the three parameterizations also. The reason for this can be seen in Figure 4.6. This parameterization has the best match to the E605 data, especially the three higher mass bins. Notice that this fit doesn't have the low p_T dip as do the other two fits. There is not much of a difference in the Run 1 Tevatron Z plots except for some minor difference in peak height and position.

4.6.2 Bringing E288 Back into Fits

Fit I adds E288 data to the data set of the previous set of fits. Table 4.10 gives the data set used for this fit. Recall that E288 had to be taken out of earlier fits because of normalization problems as well as the overabundance of Drell-Yan data at the time. With the presence of the Run 1 Tevatron data it was felt that it was no longer necessary to fear Drell-Yan data dominating the fits and that the normalizations would be kept from floating too far from their nominal values. The results are given in Table 4.11.

The fit to the LY function has several things of interest. First, the g_1 value remains at a very small value like all previous fits which included Run 1 Z data. The g_2 value is somewhat smaller than the 0.7 value from the previous two fits and g_3 has taken a big shift in value from Fit H. Also notice that the E288 normalization is now only 3% outside its error. However, the reduced χ^2 is quite large indicating the prediction does not match the data well.

The 2 parameter fit to the DWS function bears similarities to the LY function fit. It too has the tiny g_1 value and the same g_2 . This fit also shows the E288 normalization is well behaved. Note that it has also the same large reduced χ^2 .

1000000000

1000000000

1000000000

1000000000

Experiment	P_T RANGE (GeV)	BOSON MASS RANGE (GeV)
R209	0.0-1.8	5.0-11.0
CDF Z (Run 0)	0.0-22.8	91.19
CDF Z (Run 1)	0.0-20.0	91.19
D0 Z	0.0-20.0	91.19
E288	0.0-1.4	5.0-9.0
E605	0.0-1.4	7.0-9.0, 10.5-18.0

Table 4.10: Data set for Fit I.

Parameter	LY Function	DWS Function	Gauss 1
g₁	0.02	0.016	0.21
g₂	0.55	0.54	0.68
g₃	-1.50	0.00	-0.60
R209 Norm	1.01	1.02	0.86
CDF Run 1 Norm	0.90	0.89	0.89
D0 Z Norm	1.01	1.01	1.00
E605 Norm	1.07	1.15	1.00
E288 Norm	1.28	1.23	1.19 •
χ^2	407	416	176
χ^2 /dof	3.42	3.47	1.48

Table 4.11: Fit I results.



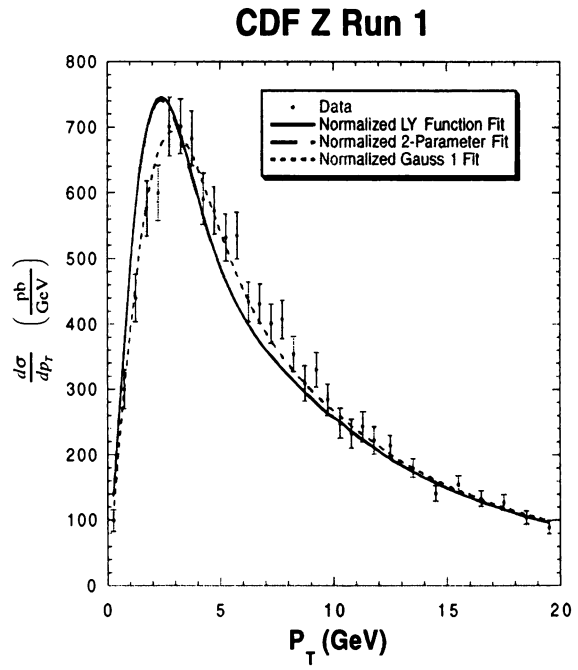
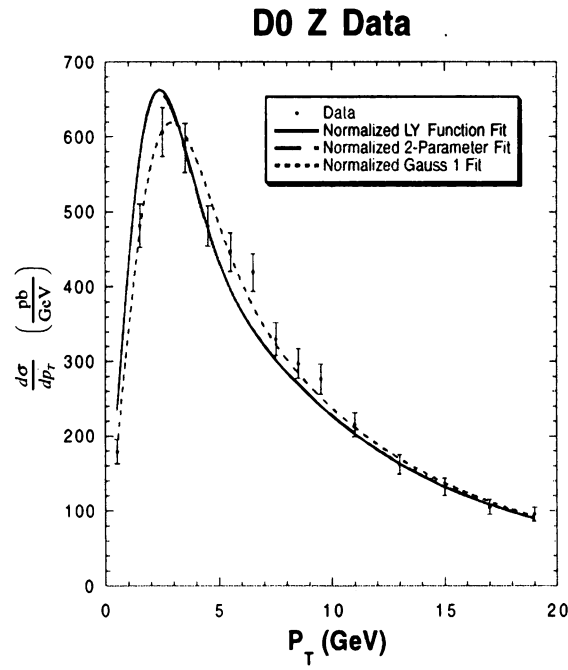
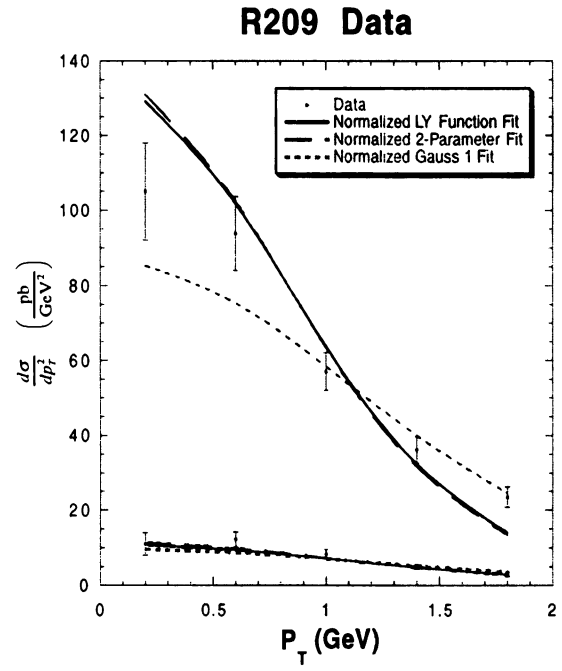
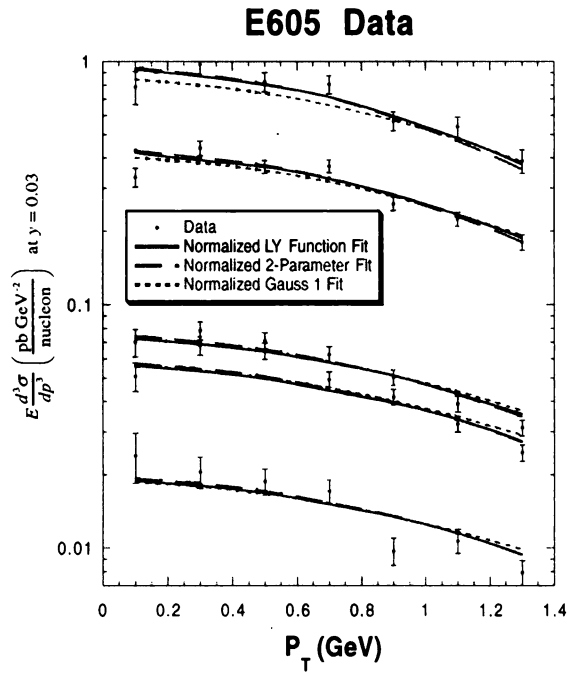
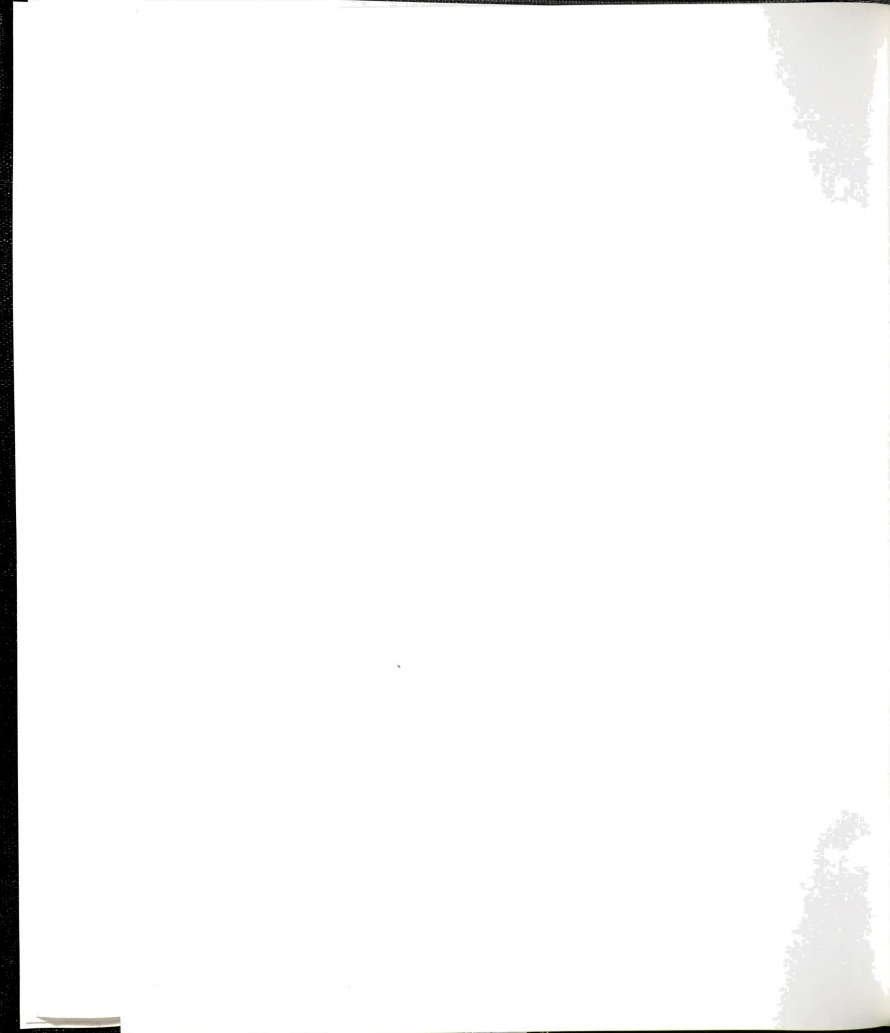


Figure 4.7: Fit I Plots compared to Data.



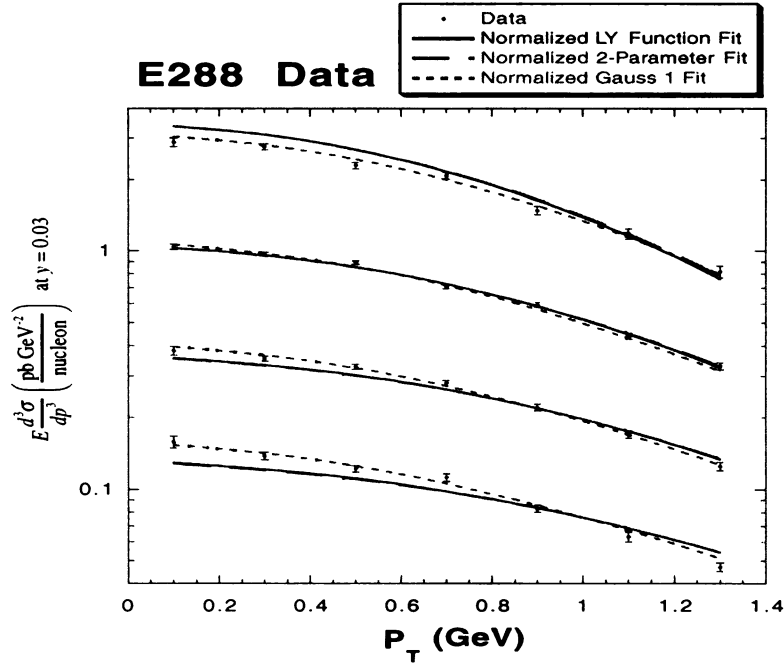


Figure 4.8: Fit I Plot of E288 compared to fit curves.

The Gauss 1 fit gives the most dramatic results here. For the first time since including the Run 1 Z data, there is a fit with a g_1 that is not nearly zero. Also the g_2 value is larger than the other two parameterizations for this fit. The big difference from the other parameterizations can be seen in the χ^2 and reduced χ^2 . It's reduced χ^2 is less than half the values for the other two functions.

This difference can best be seen from the plot comparisons to the data in Figure 4.7 and Figure 4.8. For the plots to the Run 1 Z data, both the LY and DWS functions fail to match the heights and positions of both peaks well. The Gauss 1 parameterization matches the peaks of the two experiments much better. It actually best matches the two Z p_T distributions over the whole p_T range in the fit. Looking at the E288 plot shows that the Gauss 1 fit does noticeably better than the other two fits. The three fits are indistinguishable when compared to E605, except for the lowest mass bin where there is a small difference with the Gauss 1 curve. The R209 plot shows a clear difference between Gauss 1 and the other two fits for the lowest mass bin. However the χ^2 contribution from this mass bin is about even for all the functions.



Fit	Function	Results	Data Set
A	LY	$g_1=0.05, g_2=0.57, g_3=0.83$	R209 $5<Q<8$; CDF Z Run 0; E288 $6<Q<8$
B	LY	$g_1=0.08, g_2=0.47, g_3=1.6$	R209 $5<Q<8$; CDF Z Run 0; E288 $6<Q<8$
	Gauss 1	$g_1=0.11, g_2=0.47, g_3=0.61$	
C	LY	$g_1=0.15, g_2=0.40, g_3=-0.84$ R209 Norm = 0.99 E288 Norm = 1.47	R209 $5<Q<8$; CDF Z Run 0; E288 $6<Q<8$
D	DWS	$g_1=0.18, g_2=0.27$ R209 Norm = 1.05 E288 Norm = 1.29 E605 Norm = 1.25	R209 $5<Q<8$; CDF Z Run 0; E288 $5<Q<9$; E605 $7<Q<9$
	LY	$g_1=0.16, g_2=0.34, g_3=-0.41$ R209 Norm = 1.02 E288 Norm = 1.39 E605 Norm = 1.28	
	Gauss 1	$g_1=0.21, g_2=0.47, g_3=-0.51$ R209 Norm = 0.93 E288 Norm = 1.31 E605 Norm = 1.15	
E	LY	$g_1=0.17, g_2=0.30, g_3=-0.20$ R209 Norm = 1.04 E288 Norm = 1.35 E605 Norm = 1.30	R209 $5<Q<8$; CDF Z Run 0; E288 $5<Q<9$; E605 $7<Q<9, 10.5<Q<18.0$
F	DWS	$g_1=0.24, g_2=0.34$ R209 Norm = 0.96 E605 Norm = 1.06	R209 $5<Q<11$; CDF Z Run 0; E605 $7<Q<9$
	LY	$g_1=0.15, g_2=0.48, g_3=-0.58$ R209 Norm = 0.96 E605 Norm = 1.14	

Table 4.12: Summary of fit results.

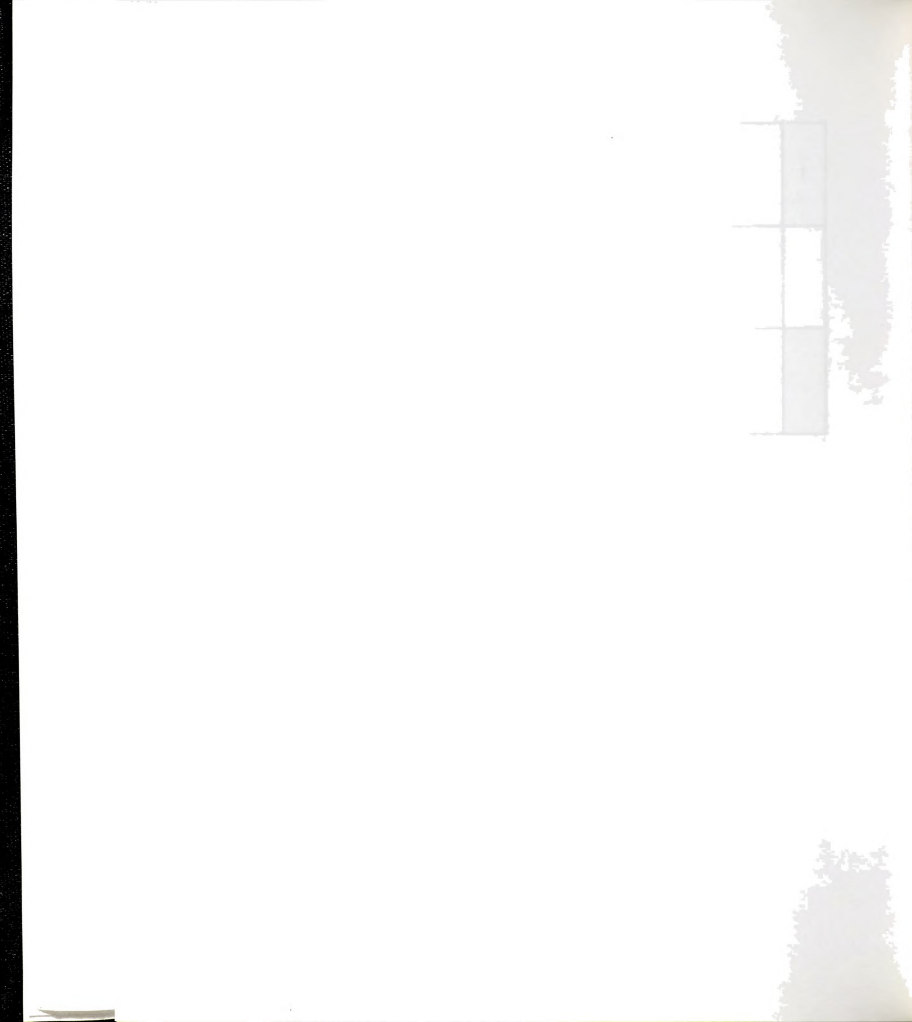
G	DWS	$g_1=0.03, g_2=0.76$ R209 Norm = 0.92 CDF Run 1 Norm = 0.89 D0 Z Run 1 Norm = 1.00 E605 Norm = 0.88	R209 $5<Q<11$; CDF Z Run 0 and Run 1; D0 Z Run 1; E605 $7<Q<9$
	LY	$g_1=0.05, g_2=0.72, g_3=-2.50$ R209 Norm = 0.93 CDF Run 1 Norm = 0.88 D0 Z Run 1 Norm = 0.99 E605 Norm = 1.05	
	Gauss 1	$g_1=0.05, g_2=0.80, g_3=-2.50$ R209 Norm = 0.89 CDF Run 1 Norm = 0.89 D0 Z Run 1 Norm = 1.00 E605 Norm = 0.94	
	Gauss 3	$g_1=0.05, g_2=0.80, g_3=-2.50$ R209 Norm = 0.89 CDF Run 1 Norm = 0.90 D0 Z Run 1 Norm = 1.00 E605 Norm = 0.94	
H	DWS	$g_1=0.03, g_2=0.71$ R209 Norm = 0.93 CDF Run 1 Norm = 0.89 D0 Z Run 1 Norm = 1.00 E605 Norm = 0.89	R209 $5<Q<11$; CDF Z Run 0 and Run 1; D0 Z Run 1; E605 $7<Q<9, 10.5<Q<18.0$
	LY	$g_1=0.03, g_2=0.70, g_3=1.00$ R209 Norm = 0.94 CDF Run 1 Norm = 0.89 D0 Z Run 1 Norm = 1.00 E605 Norm = 0.94	
	Gauss 1	$g_1=0.07, g_2=0.74, g_3=-2.00$ R209 Norm = 0.90 CDF Run 1 Norm = 0.89 D0 Z Run 1 Norm = 1.00 E605 Norm = 1.11	

Table 4.12: cont.



I	DWS	$g_1=0.02, g_2=0.54$ R209 Norm = 1.02 CDF Run 1 Norm = 0.89 D0 Z Run 1 Norm = 1.01 E288 Norm = 1.23 E605 Norm = 1.15	R209 $5 < Q < 11$; CDF Z Run 0 and Run 1; D0 Z Run 1; E288 $5 < Q < 9$; E605 $7 < Q < 9, 10.5 < Q < 18.0$
	LY	$g_1=0.02, g_2=0.55, g_3=-1.50$ R209 Norm = 1.01 CDF Run 1 Norm = 0.90 D0 Z Run 1 Norm = 1.01 E288 Norm = 1.28 E605 Norm = 1.07	
	Gauss 1	$g_1=0.21, g_2=0.68, g_3=-0.60$ R209 Norm = 0.86 CDF Run 1 Norm = 0.89 D0 Z Run 1 Norm = 1.00 E288 Norm = 1.19 E605 Norm = 1.00	

Table 4.12: cont.



Chapter 5

Conclusion

Based on the observations made in the previous chapter, the Fit I fit to the Gauss 1 parameterization is the recommended choice for further theoretical studies as well as well as for producing distributions to compare to experiments:

$$\text{Gauss 1:} \quad -g_1 b^2 - g_2 b^2 \ln\left(\frac{Q}{2Q_0}\right) - g_1 g_3 b^2 \ln(100x_a x_b), \quad (5.1)$$

$$\text{Fit I, Gauss 1:} \quad g_1 = 0.21_{-0.01}^{+0.01}, \quad g_2 = 0.68_{-0.02}^{+0.02}, \quad g_3 = -0.60_{-0.04}^{+0.05}. \quad (5.2)$$

The Fit I series of fits includes the most diverse set of data, as well as the most balanced set, including high statistics data at both ends of the τ range. The fit to the Gauss 1 function is singled out because it clearly fits the data best.

The errors in Equation 5.2 were calculated by a slightly different method than the one described on page 72 for Fit F. First, χ^2 values were calculated around the minimum in a range in all three g parameters to obtain, in essence, a three dimensional function, $\chi^2(g_1, g_2, g_3)$. Next, the surface area where this function equaled 1+minimum χ^2 was plotted in the three dimensional g parameter space, (Figure 5.1). The extremes in the coordinates for this surface on each axis was taken as the errors for the respective parameters.



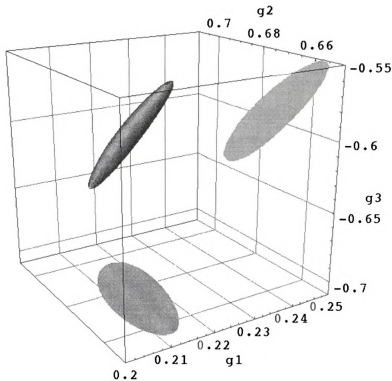


Figure 5.1: Uncertainty contour and two dimensional projections for the Fit I result with the Gauss 1 parameterization.

Recent work on obtaining errors for PDF parameters, [41], [42], and [43], points out that using $1 + \text{minimum } \chi^2$ as the confidence limit is idealistic in global fitting where experiments often make judgements on systematic uncertainties. When a more satisfactory method of obtaining uncertainties for PDF's is achieved, perhaps it can be adopted for use here in the future.

The result in (5.2) certainly doesn't mark the end of the study of low p_T , non-perturbative QCD. In the future, there will be even more data to include in fits. There are also more recent PDF's to use in the theory calculation and it will be interesting to see the effect of these different PDF's. Finally, additional theoretical work may give rise to



other parameterizations. In fact, it has been suggested [44] that perhaps the non-perturbative function should have a more explicit dependence on the x values as in the CSS formulation, and that the Gauss 1 function can be viewed as two terms, with the first term suggesting a first order expansion in x ,

$$-b^2 \left[g_1 (1 + g_3 \ln(100x_a x_b)) + g_2 \ln \left(\frac{Q}{2Q_0} \right) \right].$$

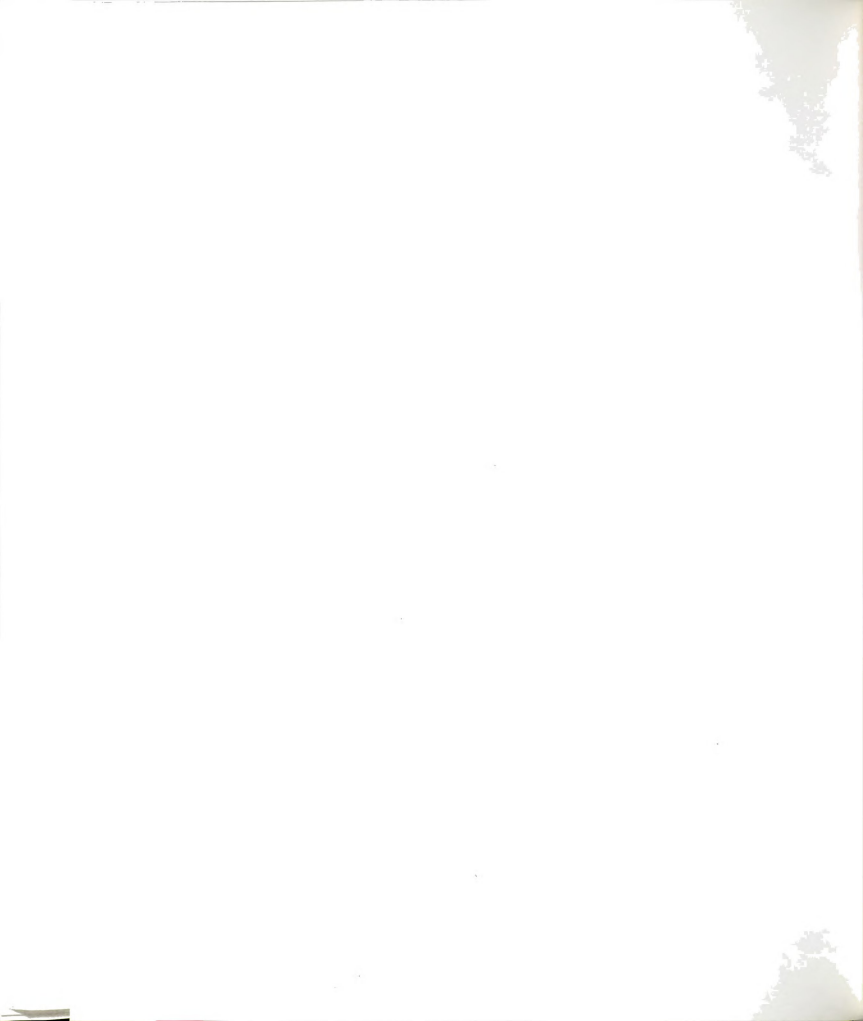
Appendix A

The Level 1 Trigger Monitor Program

A.1 Introduction

The level 1 Trigger Monitor Program, TRGMON [45], displays information on the programming and operational status of the DØ level 1 trigger. It is an important tool for assuring that the level 1 trigger is operating properly during data taking and that the trigger framework is programmed as expected. Along with the trigger framework, the current status is given for the specific triggers, the calorimeter trigger, and the global thresholds.

It was determined during Run 1a data taking that TRGMON did not provide enough functionality for those monitoring the level 1 trigger. Some of the data displayed by the program are average rates and percentages. These averages were computed over an integration time of approximately five seconds. The problem was that in some cases it is more important to know these average values over a longer time period, perhaps an entire run, rather than over the previous five seconds. Therefore, a new version of TRGMON was written which allowed for a user-chosen integration time rather than a fixed time.



A.2 Method of Information Gathering and Computing

The TRGMON program gets its information directly from the Trigger Control Computer (TCC). As the name implies, the TCC is what actually sets the parameters for the level 1 trigger through a program called COOR. The TCC at a fixed five second interval will request a set of data from the trigger framework. This set of data, called the First level Trigger Data Block, contains all the information on the current state of the level 1 trigger. How quickly the framework sends this data block is dependent on how much data the data acquisition system is handling at the time. Therefore, the TCC will not always have a new data block at precisely five seconds, and so integration times for rates and percentages computed from these blocks will only be five seconds on average. Once the TCC receives a new data block from the trigger framework, it will compute the difference in some scalars from the previous data block it received. These delta values are saved in a separate data block. After the level 1 data block is received by the TCC and the delta scalars values are calculated, then it is available to be sent to TRGMON.

In the original version of TRGMON, once the data were received it could calculate the necessary rates and percentages in the following way. Knowing the differences and the beam crossing rate, average rates and percentages were calculated by:

$$\text{rate (in Hz)} = \frac{\text{delta counts}}{\text{Beam crossing period} \cdot \text{delta beam crossings}} \quad (\text{A.1})$$

One example calculation is the global level 1 trigger firing rate. To calculate this rate, the current count of the number of level 1 firings is subtracted from the same count from the previous five seconds. This difference is then used to get the firing rate through Equation A.1.



A.3 Implementing User Defined Integration Times

A.3.1 Method Of Calculating Over Larger Integration Times

In order to allow longer integration times it was necessary to make a fundamental change in the information which was stored by TRGMON and how it was stored. Instead of having only the quantities for the current beam crossing and for the crossing five seconds prior to it, the information from the data blocks are stored in ring arrays. When a new scaler value is received, it is stored in a ring array and it is placed in the location of the oldest value of that scaler. The “delta counts” value used in Equation A.1 is now the subtraction of the oldest value in the ring array from the newest value.

A.3.2 User Interface

The user is allowed to choose an integration time from a range of five seconds to two hours. The integration time must be an integer multiple of the refresh rate, although the user could also choose this interval. These choices determine the sizes of the ring arrays.

A.3.3 Behavior Under Special Conditions

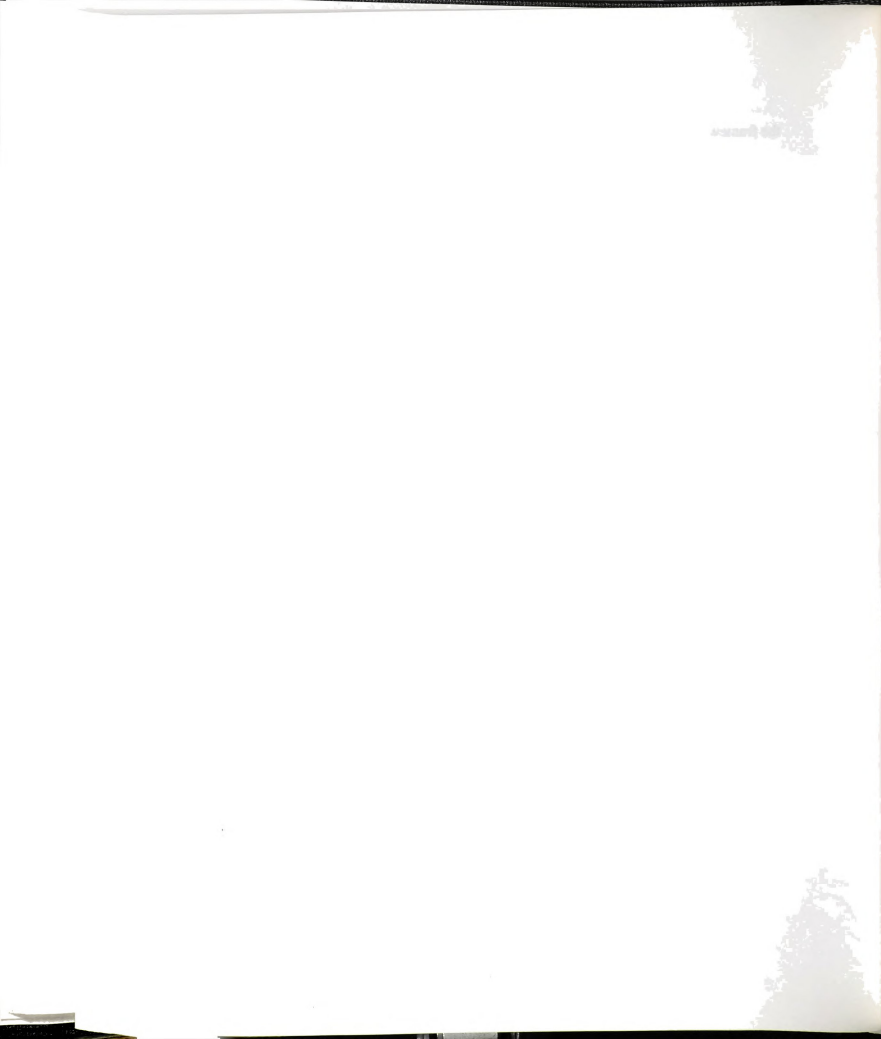
After a given set of values for the integration and refresh times are chosen, the displayed rates and percentages will not at first be calculated over the chosen integration time. There will first be a transitional stage where the ring arrays must become filled. The delta counts will still be calculated by the difference of the oldest value and the newest scaler value. Therefore as the ring arrays are in the process of becoming filled, the integration time will increase with each refresh. This transition state ends when the user-chosen integration time is reached.



Another special condition is when the TCC is not receiving new data blocks from the framework, but continues to receive data on the same beam crossing. In this case, when TRGMON is given these stale data blocks, the ring buffers will continue to be filled with the same scaler value. The result will be that the rates and percentages will degrade to zero with each refresh. TRGMON will however indicate in its display that the data blocks are stale.

A.4 Testing and Implementation of New TRGMON

Before the revised monitoring program could be used by the DØ shift crew, it had to be tested for accuracy and reliability. The program was first tested on a hardware simulator of the level 1 trigger located at MSU. After this, it was put into place on the DØ computer to monitor actual data taking runs. The revised TRGMON was being run in parallel with the older version at this point, with the older version still being used by DØ shift members. After finding the program to be working as designed, the revised TRGMON was then put in place and used on shifts for the remainder of Run 1.



Appendix B

The Z Calibration Detector

B.1 Introduction

During the latter part of Run 1a, studies were done [46] in order to compare the CDC tracks of muons to their tracks in the Muon Detector. It was found that for a muon the CDC track and the Muon Detector track did not lie along the same line. Specifically, the Muon Detector track, when extrapolated to the CDC, would be offset in z from the CDC track. Figure B.1 illustrates such a misalignment. Since the accuracy of the z position hits in the Muon Detector were determined independently [46], it was determined that there was an inaccuracy in the calculation of the z coordinate for the CDC hits. Since inaccurate z 's in the CDC hits would result in a track with an incorrect θ angle, this could have an effect on the accuracy of the determination of the z position of the interaction vertex. It would also lead to an inaccurate calculation of p_z and p_T for the particle which produced the track. Therefore it was proposed [47] that a simple detector be constructed to recalibrate the z coordinate for the CDC. The z Calibration Detector, (ZCD), was constructed and installed during a short off-line period for the DØ Detector.

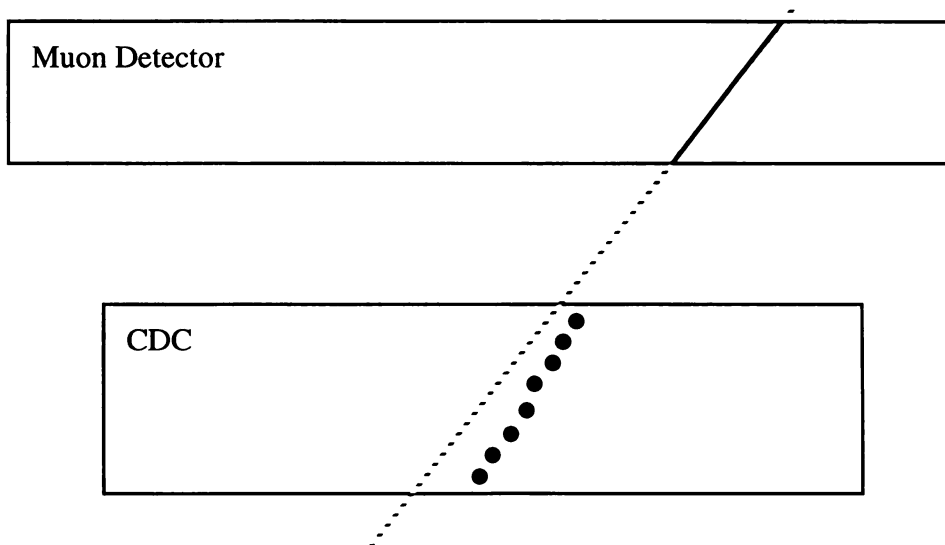


Figure B.1: A Muon Detector track extrapolated to the CDC does not align with the z positions of the delay line hits.

B.2 Design of Detector

It was necessary to keep the design simple because there was a limited time in which the DØ Detector would be off-line and outside the collision hall. The simple design consisted of scintillating fibers placed at precisely known positions in z just outside the CDC. Therefore when an energetic particle passed through a fiber, the particle's z position from the fiber could be compared with the z positions from the delay line hits. The scintillating fiber detector was made up of twenty separate modules, with each module containing eight scintillating fibers 2 mm in diameter and 5 in long. Each scintillating fiber was connected to a clear waveguide fiber which ran into a photomultiplier tube (PMT). There was one PMT for each module, so that on each module all eight clear fibers fed into the one PMT. Figure B.2 is a diagram of the layout of a module.



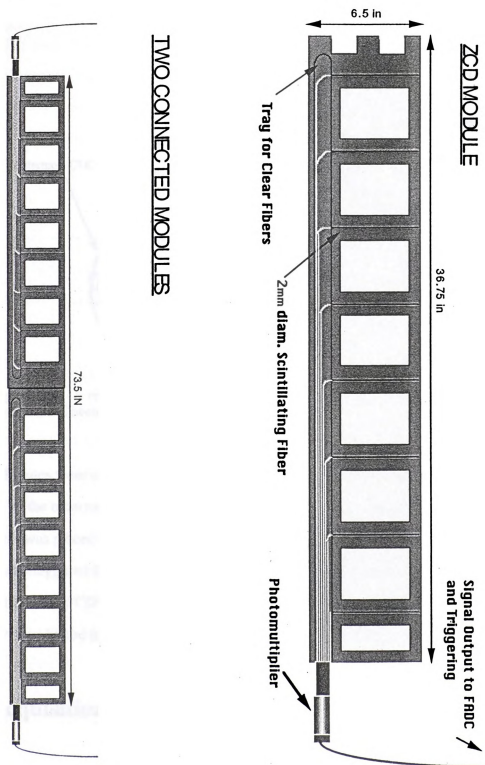


Figure B.2: Diagram of a ZCD module and two connecting modules.



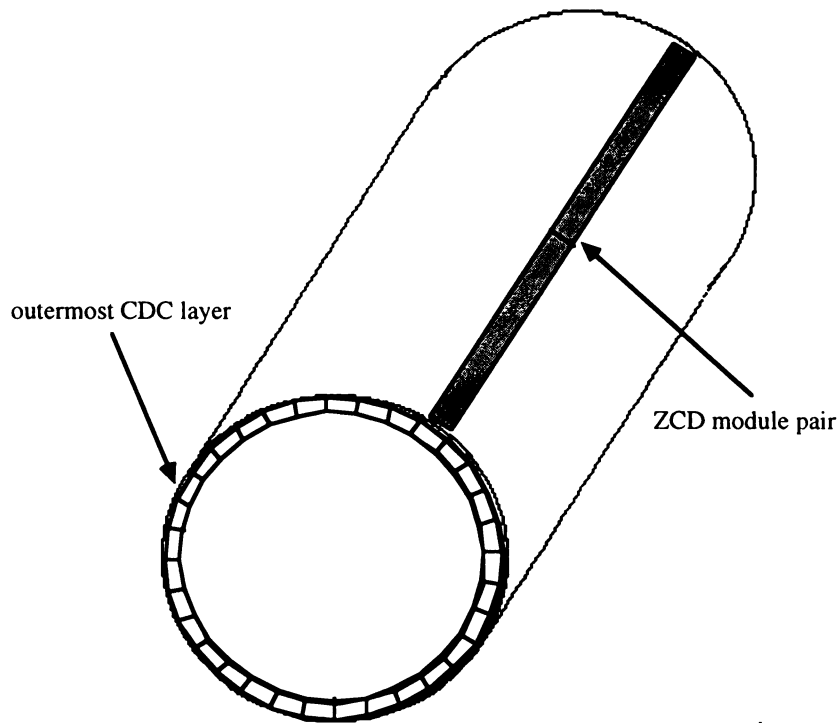
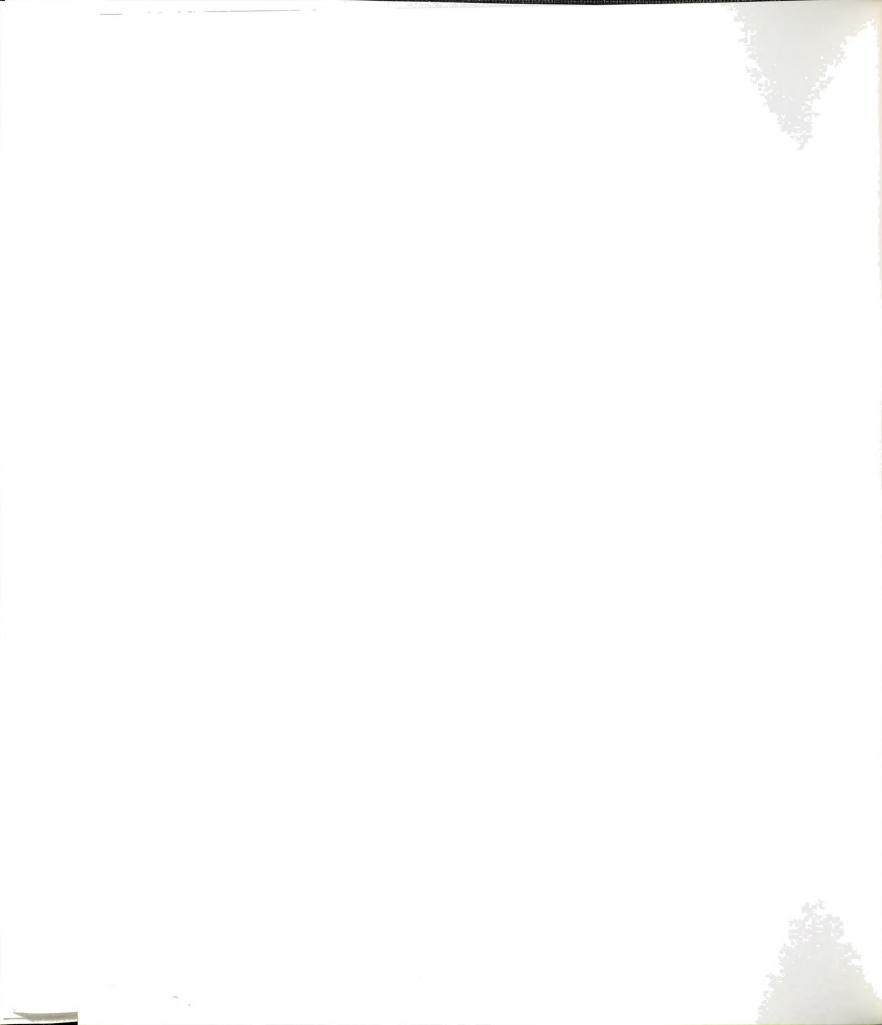


Figure B.3: A representation of the placement of one of the ZCD modules over a CDC sector.

Modules were connected in pairs and each module pair was placed to entirely cover one of the outermost CDC sectors as shown by Figure B.3. Even though each module pair was placed to cover only one CDC sector in the outermost layer, the CDC sectors were staggered in ϕ between layers so that each module pair covered two sectors in the first and third CDC layer. Figure B.4 shows an edge-on view of the CDC with the sectors covered by the ten module pairs.

B.3 Acquisition and Selection of Data

Before the calibration of the CDC could take place, the events to be used in the calibration process needed to be selected. The data were selected to include events which possessed the necessary characteristics required for calibration. It was also required that



these quantities could be measured accurately. These were the criteria that were used in selecting the data to be used in the calibration process:

- At least one ZCD module must have registered a hit for the event.
- Only one CDC track was allowed to intersect a ZCD module which registered a hit fiber. (The reason for this is that if two or more fibers were hit for a given module, there was no way to tell which fibers were hit because all of the fibers were read by one PMT.)
- The ϕ angle of the CDC track must have been within the ϕ range covered by the module which registered the hit. (This requirement weeded out nonradial tracks.)
- A CDC delay line hit must have been read out from both sides of the delay line.

B.4 Calibration Method

Once the data set was selected, the same calibration process was used for each event in the data set. The first step in the calibration process was to locate the CDC track intersecting the module with a hit and extrapolate the track out to the radial distance of the ZCD fibers. The z position for which the extrapolation reached the radial distance of the fibers was designated Z_{ext} . The fiber which came closest to the extrapolated track was then the fiber which the particle hit and one could then compare the well-measured position of the fiber, Z_{fiber} , to Z_{ext} to see how far off the CDC track was. An example of such an extrapolation is shown by Figure B.5.



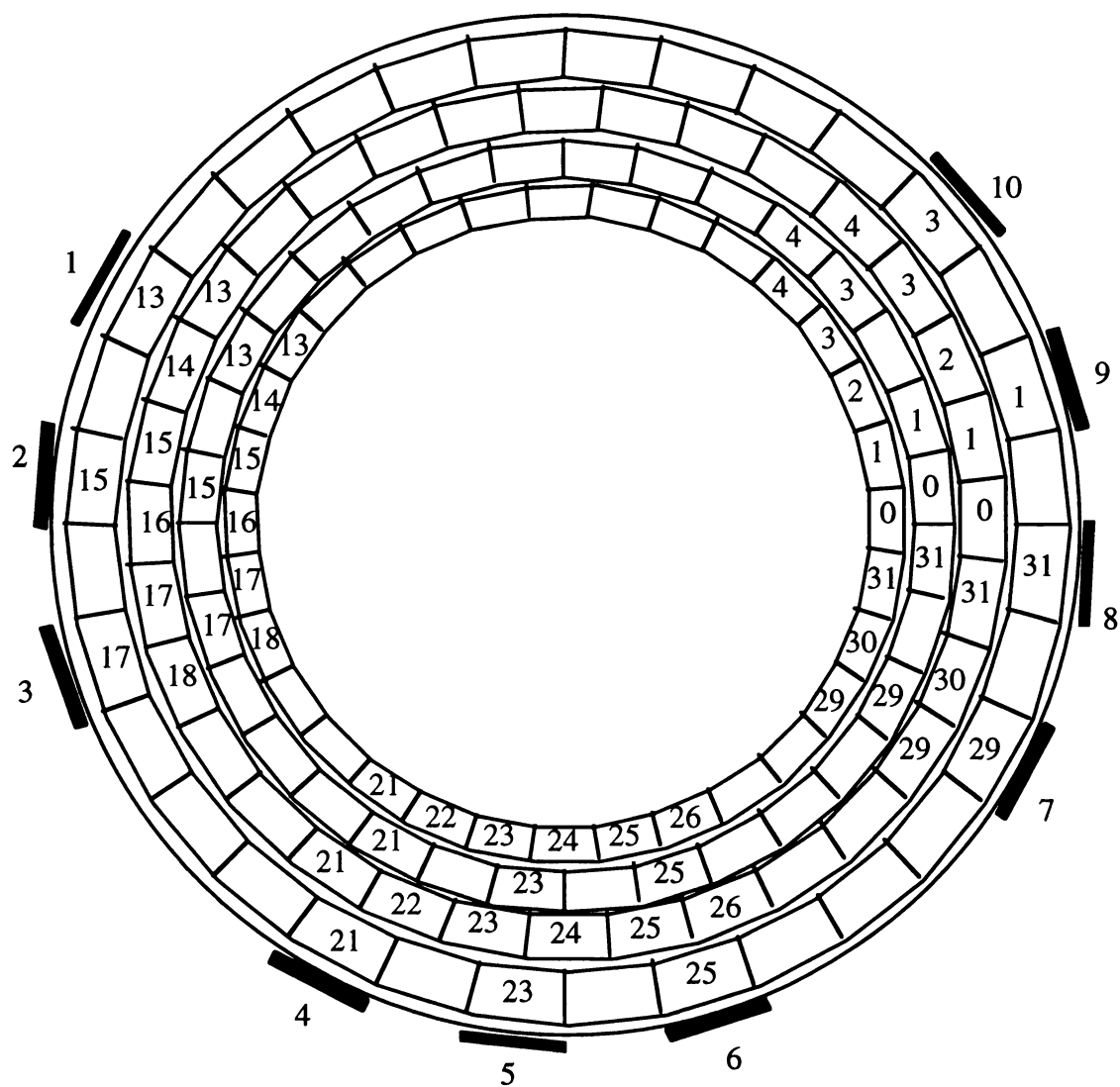


Figure B.4: Placement of the ZCD module pairs in relation to the CDC sectors. The numbering of the module pairs is shown as well as the CDC sectors covered by the ZCD.



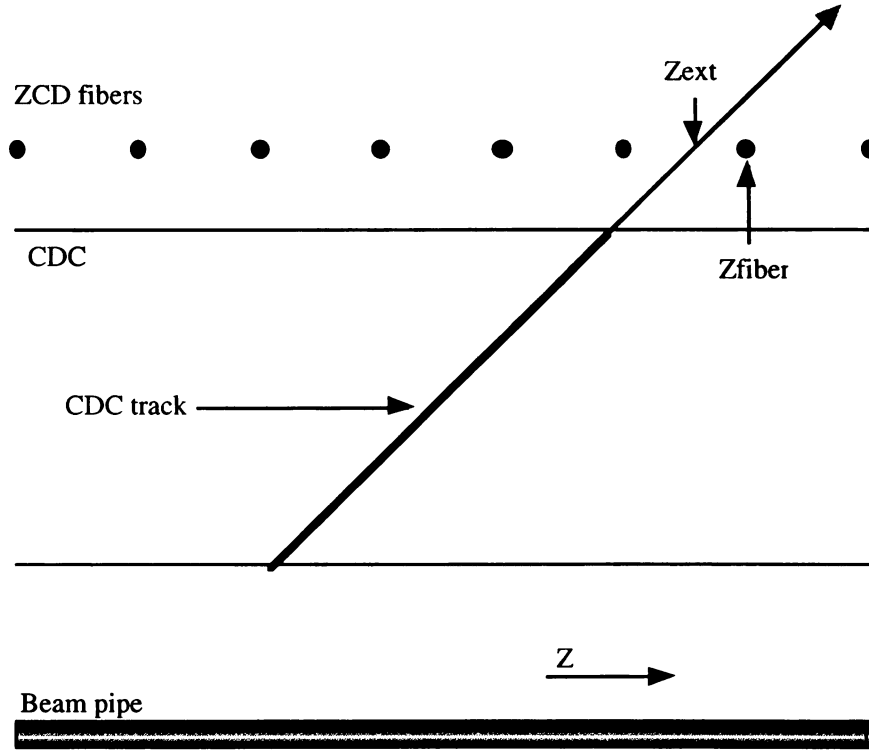


Figure B.5: Extrapolation of CDC track out to the ZCD module to obtain Z_{ext}

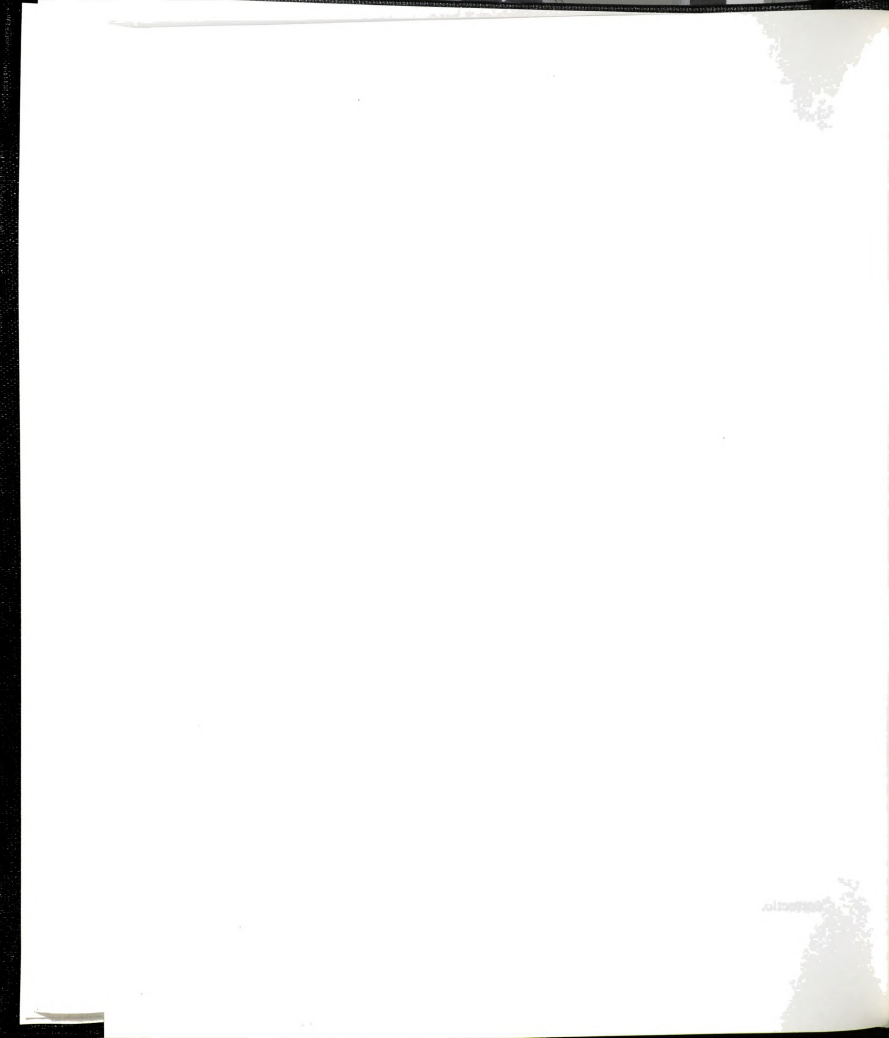
For each fiber in the ZCD, a distribution of ΔZ was plotted,

$$\Delta Z = Z_{fiber} - Z_{ext}. \quad (B.1)$$

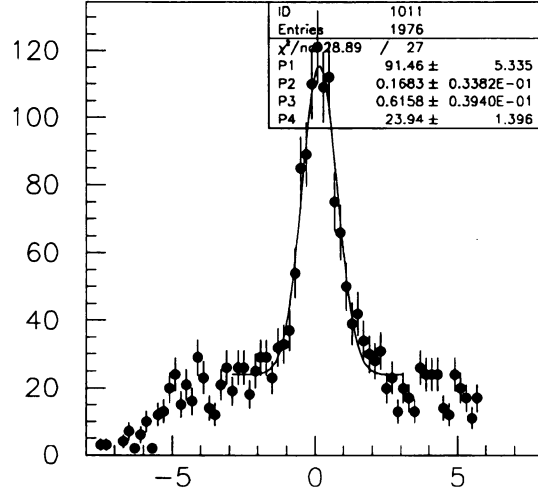
Each of these plots were then fit to a Gaussian distribution added to a constant.

Examples of such fits are depicted in Figure B.6. The mean ΔZ of the fitted function, $\overline{\Delta Z}$, was used as the average offset between Z_{fiber} and Z_{ext} for the fiber. One could then obtain the average extrapolated position of a CDC track hitting a certain fiber, Z_{ext} , by adding $\overline{\Delta Z}$ to Z_{fiber} .

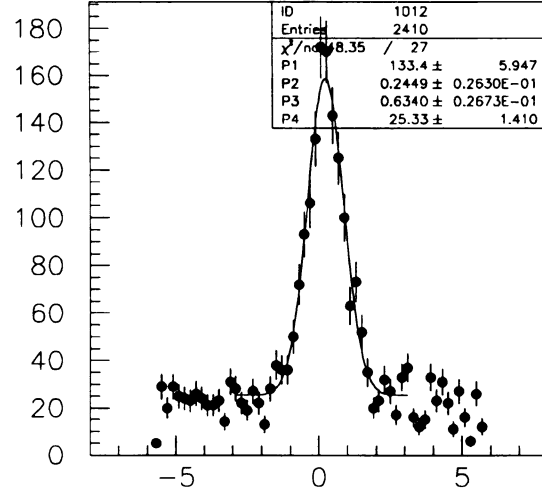
Once $\overline{\Delta Z}$ and Z_{ext} were obtained for each fiber, then plots were made of Z_{fiber} vs. $\overline{\Delta Z}$ and Z_{fiber} vs. Z_{ext} for each module and module pair. Each of these distributions were fit to a line. The slopes and intercepts of these fitted lines were then used as the corrections to be applied to CDC hits. Some of these fits are shown in Figure B.7.



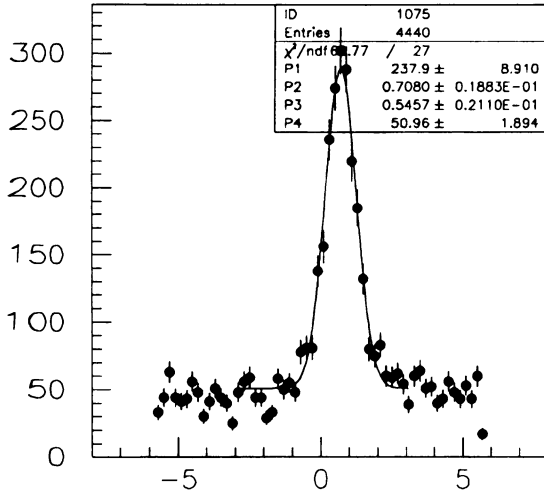
DZ BETWEEN DELAY LINE 8 AND ZCD FIBER, DL8.HST(New dr correct)



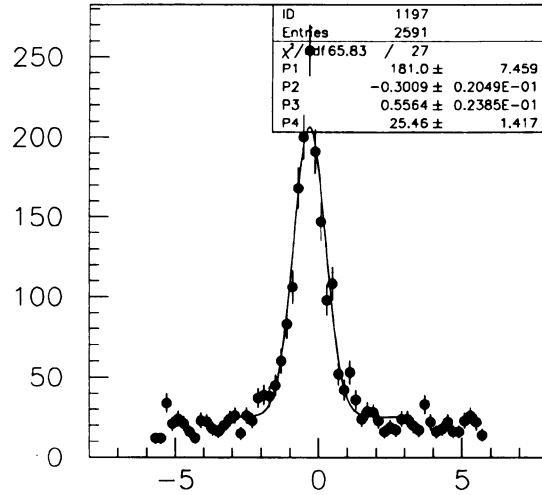
DELT Z OF MOD 1 FIBER 1



DELT Z OF MOD 1 FIBER 2

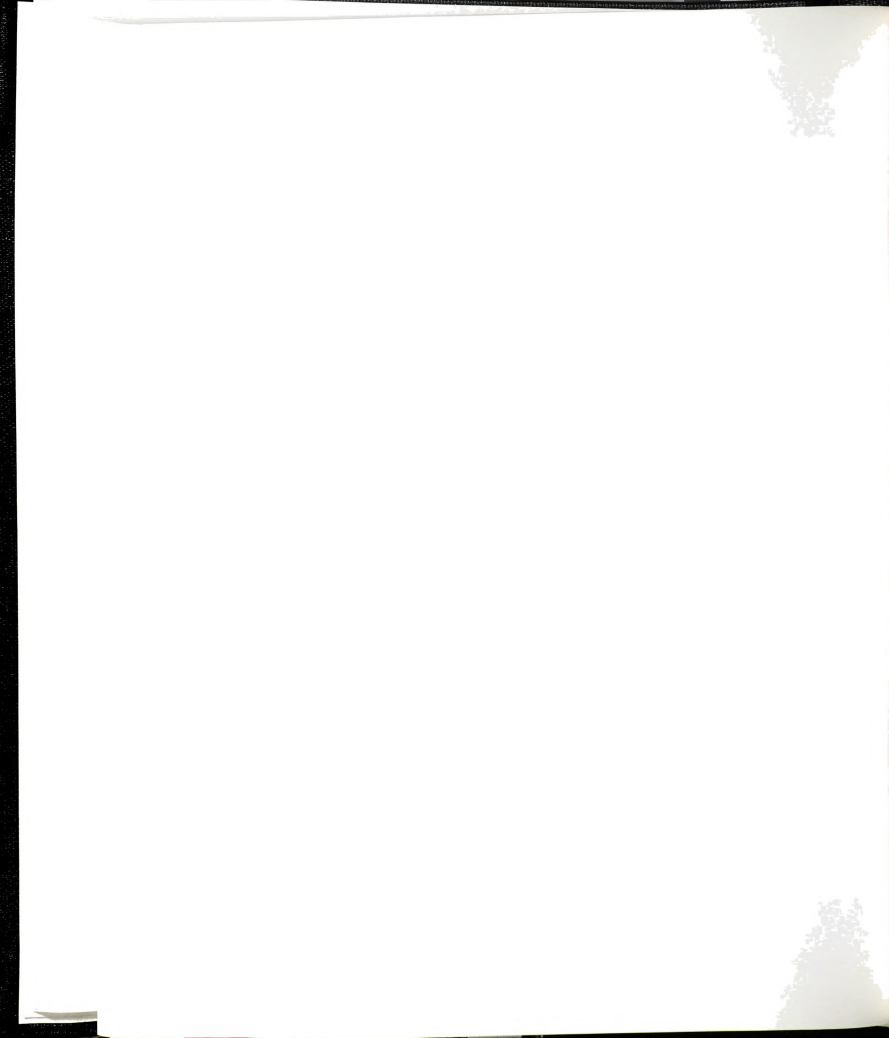


DELT Z OF MOD 7 FIBER 5



DELT Z OF MOD 19 FIBER 7

Figure B.6: Typical Fits to ΔZ for four fibers.



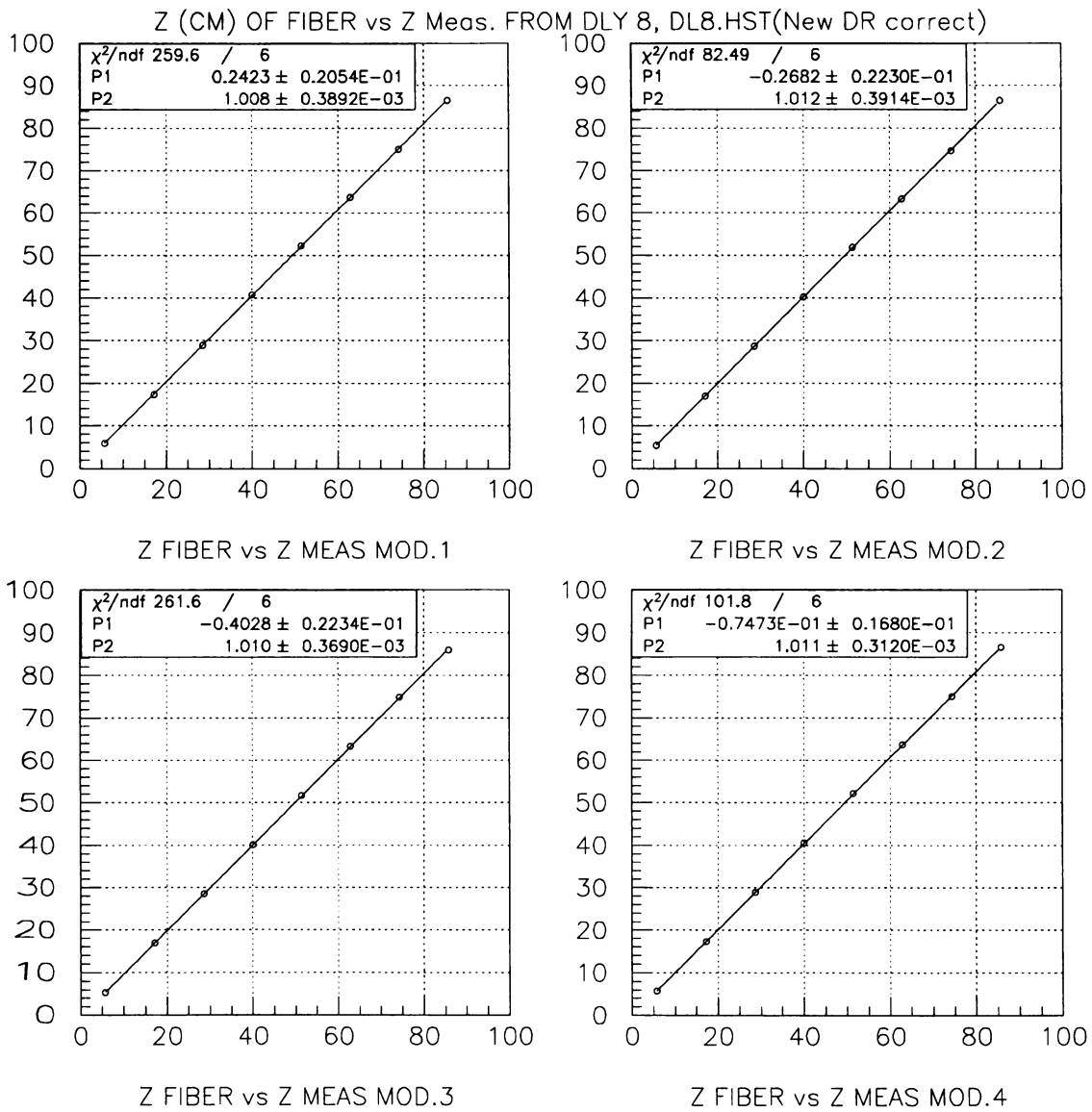


Figure B.7: Examples of linear fits to Z_{fiber} vs. Z_{ext} for modules 1-4.

B.5 Results

The values for these corrections are shown in the following tables as originally listed in [48]. The tables list the values from fits to the data of module pairs rather than individual modules. Therefore, under column i , data from module i and module $i+10$ were used in the fit. The seven delay lines with “No Data” gave us little or no hit information and it is suspected that the problem lies with the delay lines themselves rather than with the ZCD. Also, no data for module pair 10 is listed because it did not produce enough data for reliable statistics.

The mean value for the slope is $1.011 \pm .0022$ which can result in a difference of as much as 1.5 cm for the delay line hit positions. This average slope was included with other CDC recalibration studies which used the Muon Detector to obtain an average correction to the CDC [49].



Delay Line	Module Pair								
	1	2	3	4	5	6	7	8	9
DL1	1.0139	1.0122	1.0103	1.0093	1.0090	1.0104	1.0118	1.0108	1.0137
DL1-L	1.0127	1.0119	1.0099	1.0114	1.0074	No Data	1.0121	1.0146	1.0136
DL2	1.0095	1.0094	1.0082	1.0072	1.0046	1.0076	1.0104	1.0091	1.0097
DL2-L	1.0104	1.0103	1.0079	1.0081	1.0051	No Data	1.0078	1.0079	1.0110
DL3	1.0129	1.0120	1.0112	1.0097	1.0101	1.0119	1.0133	1.0139	1.0140
DL4	1.0099	1.0101	1.0093	1.0081	1.0056	1.0100	1.0104	1.0101	1.0114
DL5	1.0138	1.0126	No Data	1.0093	1.0081	1.0113	1.0132	1.0117	1.0151
DL5-L	1.0133	1.0118	1.0117	1.0130	1.0096	No Data	1.0120	No Data	1.0146
DL6	1.0126	1.0098	1.0091	1.0070	1.0057	1.0097	1.0106	1.0097	1.0109
DL6-L	1.0108	1.0095	1.0090	No Data	1.0065	No Data	1.0092	1.0096	1.0106
DL7	1.0144	1.0128	1.0121	1.0105	1.0098	1.0122	1.0129	1.0139	1.0152
DL8	1.0113	1.0111	1.0088	1.0090	1.0087	1.0104	1.0105	1.0105	1.0119

Table B.1: Slopes from linear fits to Z_{fiber} vs Z_{ext} distributions of module pairs.



Delay Line	Module Pair								
	1	2	3	4	5	6	7	8	9
DL1	-0.021	-0.181	-0.179	0.069	0.098	0.047	0.187	-0.175	0.162
DL1-L	0.014	-0.017	-0.219	0.096	0.186	No Data	0.133	0.112	0.130
DL2	0.110	-0.215	-0.316	0.050	-0.047	-0.022	-0.385	0.162	0.245
DL2-L	-0.038	-0.512	-0.396	-0.051	0.054	No Data	-0.149	-0.157	0.180
DL3	-0.008	-0.244	-0.290	0.060	0.133	0.083	-0.109	-0.304	0.076
DL4	-0.115	-0.779	-0.565	0.010	-0.221	-0.148	-0.007	-0.108	0.233
DL5	0.205	-0.125	No Data	0.186	0.106	-0.084	-0.413	0.031	0.320
DL5-L	0.141	-0.015	-0.388	0.037	0.244	No Data	0.101	No Data	-0.038
DL6	0.279	-0.104	-0.042	0.113	-0.020	-0.053	-0.406	-0.342	0.224
DL6-L	-0.022	-0.293	-0.183	No Data	0.165	No Data	-0.420	-0.235	-0.043
DL7	-0.107	-0.082	-0.144	0.082	0.141	0.178	0.007	0.226	0.284
DL8	0.061	-0.250	-0.330	0.014	-0.009	0.032	0.056	-0.222	0.046

Table B.2: Intercepts from linear fits to Z_{fiber} vs Z_{ext} distributions of module pairs.

Appendix C

Reprint of Preliminary Fits Paper

F. Landry, R. Brock, G. Ladinsky, and C.-P. Yuan, *Phys. Rev.* **D63** 013004 (2001).

New fits for the non-perturbative parameters in the CSS resummation formalism

F. Landry, R. Brock, G. Ladinsky, and C.-P. Yuan

Department of Physics and Astronomy, Michigan State University, East Lansing, Michigan 48824

(Received 25 May 1999; published 5 December 2000)

We update the non-perturbative function of the Collins-Soper-Sterman (CSS) resummation formalism which resums the large logarithmic terms originating from multiple soft gluon emission in hadron collisions. Two functional forms in impact parameter (b) space are considered, one with a pure Gaussian form with two parameters and another with an additional linear term. The results for the two parameter fit are found to be $g_1 = 0.24^{+0.08}_{-0.07} \text{ GeV}^2$ and $g_2 = 0.34^{+0.07}_{-0.08} \text{ GeV}^2$. The results for the three parameter fit are $g_1 = 0.15^{+0.04}_{-0.03} \text{ GeV}^2$, $g_2 = 0.48^{+0.04}_{-0.05} \text{ GeV}^2$, and $g_3 = -0.58^{+0.26}_{-0.20} \text{ GeV}^{-1}$. We also discuss the potential of the full Fermilab Tevatron run 1 Z boson data for further testing of the universality of the non-perturbative function within the context of Drell-Yan production.

DOI: 10.1103/PhysRevD.63.013004

PACS number(s): 12.15.Ji, 12.60.Cn, 13.20.-v, 13.35.-r

I. INTRODUCTION

It is a prediction of the theory of quantum chromodynamics (QCD) that at hadron colliders the production of Drell-Yan pairs or weak gauge bosons (W^\pm and Z) will generally be accompanied by gluon radiation. Therefore, in order to test QCD theory or the electroweak properties of vector bosons, it is necessary to include the effects of multiple gluon emission. At the Fermilab Tevatron (a $p\bar{p}$ collider), we expect about 2×10^6 W^\pm and 6×10^5 Z bosons produced at $\sqrt{S} = 1.8 \text{ TeV}$, per 100 pb^{-1} of luminosity. This large sample of data is useful (i) for QCD studies (with either single or multiple scales), (ii) as a tool for precision measurements of the W boson mass and width, and (iii) as a probe for new physics (e.g., Z'). Achievement of these physics goals requires accurate predictions for the distributions of the rapidity and the transverse momentum of W^\pm/Z bosons and of their decay products.

Consider the production process $h_1 h_2 \rightarrow VX$. Denote Q_T and Q to be the transverse momentum and the invariant mass of the vector boson V , respectively. When $Q_T \sim Q$, there is only one hard scale and a fixed-order perturbation calculation is reliable. When $Q_T \ll Q$, there are two hard scales and the convergence of the conventional perturbative expansion is impaired. Hence, it is necessary to apply the technique of QCD resummation to combine the singular terms in each order of perturbative calculation, which yields

$$\begin{aligned} \frac{d\sigma}{dQ_T^2} \sim \frac{1}{Q_T^2} \{ & \alpha_s(L+1) + \alpha_s^2(L^3+L^2) + \alpha_s^3(L^5+L^4) \\ & + \alpha_s^4(L^7+L^6) + \dots + \alpha_s^2(L+1) + \alpha_s^3(L^3+L^2) \\ & + \alpha_s^4(L^5+L^4) + \dots + \alpha_s^3(L+1) + \alpha_s^4(L^3+L^2) \\ & + \dots \}, \end{aligned} \quad (1)$$

where α_s is the strong coupling constant, L denotes $\ln(Q^2/Q_T^2)$ and the explicit coefficients multiplying the logs are suppressed.

Resummation of large logarithms yields a Sudakov form factor [1,2] and cures divergences as $Q_T \rightarrow 0$. This resuma-

tion was pioneered by Dokshitzer, D'yakonov and Troyan (DDT) who performed an analysis in Q_T space which led to a leading-log resummation formalism [1]. Later, Parisi-Petronzio showed [2] that for large Q the $Q_T \rightarrow 0$ region can be calculated perturbatively by imposing the condition of transverse momentum conservation:

$$\delta^{(2)}\left(\sum_{i=1}^n \vec{k}_{T_i} - \vec{q}_T\right) = \int \frac{d^2b}{4\pi^2} e^{i\vec{q}_T \cdot \vec{b}} \prod_{i=1}^n e^{i\vec{k}_{T_i} \cdot \vec{b}}, \quad (2)$$

in b -space (b is the impact parameter, which is the Fourier conjugate of Q_T). Their improved formalism also sums some subleading-logs. They showed that as $Q \rightarrow \infty$, events at $Q_T \sim 0$ may be obtained asymptotically by the emission of at least two gluons whose transverse momenta are not small and add to approximately zero. The intercept at $Q_T = 0$ is predicted to be [2]

$$\left. \frac{d\sigma}{dQ_T^2} \right|_{Q_T \rightarrow 0} \sim \sigma_0 \left(\frac{\Lambda_{\text{QCD}}^2}{Q^2} \right)^{\eta_0}, \quad (3)$$

where $\eta_0 = A \ln[1 + 1/A]$ with $A = 12C_F/(33 - 2n_f)$, and $\eta_0 \approx 0.6$ for $n_f = 4$ and $C_F = 4/3$. Collins and Soper extended [3] this work in b -space and applied the properties of the renormalization group invariance to create a formalism that resums all the large log terms to all orders in α_s .

Although various formalisms for resumming large $\ln(Q^2/Q_T^2)$ terms have been proposed in the literature [4,5], we will concentrate in this paper on the formalism given by Collins, Soper and Sterman (CSS) [6], which has been applied to studies of the production of single [7-10] and double [11] weak gauge bosons as well as Higgs bosons [12] at hadron colliders.

II. COLLINS-SOPER-STERMAN RESUMMATION FORMALISM

In the CSS resummation formalism, the cross section is written in the form

$$\frac{d\sigma(h_1 h_2 \rightarrow VX)}{dQ^2 dQ_T^2 dy} = \frac{1}{(2\pi)^2} \int d^2b e^{i\vec{Q}_T \cdot \vec{b}} \bar{W}(b, Q, x_1, x_2) + Y(Q_T, Q, x_1, x_2), \quad (4)$$

where y is the rapidity of the vector boson V , and the parton momentum fractions are defined as $x_1 = e^y Q / \sqrt{S}$ and $x_2 = e^{-y} Q / \sqrt{S}$ with \sqrt{S} as the center-of-mass (c.m.) energy of the hadrons h_1 and h_2 . In Eq. (4), Y is the regular piece which can be obtained by subtracting the singular terms from the exact fixed-order result. The quantity \bar{W} satisfies a renormalization group equation with the solution of the form

$$\bar{W}(Q, b, x_1, x_2) = e^{-S(Q, b, C_1, C_2)} \bar{W}\left(\frac{C_1}{C_2 b}, b, x_1, x_2\right). \quad (5)$$

Here the Sudakov exponent is defined as

$$S(Q, b, C_1, C_2) = \int_{C_1^2/b^2}^{C_2^2 Q^2} \frac{d\bar{\mu}^2}{\bar{\mu}^2} \left[A(\alpha_s(\bar{\mu}), C_1) \ln\left(\frac{C_2^2 Q^2}{\bar{\mu}^2}\right) + B(\alpha_s(\bar{\mu}), C_1, C_2) \right], \quad (6)$$

and the x_1 and x_2 dependence of \bar{W} factorizes as

$$\bar{W}\left(\frac{C_1}{C_2 b}, b, x_1, x_2\right) = \sum_j e_j^2 C_{jh_1}\left(\frac{C_1}{C_2 b}, b, x_1\right) C_{jh_2}\left(\frac{C_1}{C_2 b}, b, x_2\right). \quad (7)$$

Here, C_{jh} is a convolution of the parton distribution function (f_{ah}) with calculable Wilson coefficient functions (C_{ja}), which are defined through

$$C_{jh}(Q, b, x) = \sum_a \int_x^1 \frac{d\xi}{\xi} C_{ja}\left(\frac{x}{\xi}, b, \mu = \frac{C_3}{b}, Q\right) \times f_{ah}\left(\xi, \mu = \frac{C_3}{b}\right). \quad (8)$$

The sum on the index a is over incoming partons, j denotes the quark flavors with (electroweak) charge e_j , and the factorization scale μ is fixed to be C_3/b . A few comments about this formalism:

- (a) The A , B and C functions can be calculated order-by-order in α_s .
- (b) A special choice can be made for the renormalization constants C_i so that the contributions obtained from the expansion in α_s of the CSS resummed calculation agree with those from the fixed-order calculation. This is the canonical choice. It has $C_1 = C_3 = 2e^{-\gamma_E} b_0$ and $C_2 = C_1/b_0 = 1$, where γ_E is Euler's constant.
- (c) b is integrated from 0 to ∞ . For $b \gg 1/\Lambda_{QCD}$, the perturbative calculation is no longer reliable. In order to ac-

count for non-perturbative contributions from the large b region this formalism includes an additional multiplicative factor which contains measurable parameters.

We refer the readers to Ref. [9] for a more detailed discussion on how to apply the CSS resummation formalism to the phenomenology of hadron collider physics.

A. The non-perturbative function

As noted in the previous section, it is necessary to include an additional factor, usually referred to as the "non-perturbative function," in the CSS resummation formalism in order to incorporate some long distance physics not accounted for by the perturbative derivation. Collins and Soper postulated [6]

$$\bar{W}_{j\bar{k}}(b) = \bar{W}_{j\bar{k}}(b_*) \bar{W}_{j\bar{k}}^{NP}(b), \quad (9)$$

with

$$b_* = \frac{b}{\sqrt{1 + (b/b_{max})^2}}, \quad (10)$$

so that b never exceeds b_{max} and $\bar{W}_{j\bar{k}}(b_*)$ can be reliably calculated in perturbation theory. (In numerical calculations, b_{max} is typically set to be of the order of 1 GeV^{-1} .) Based upon a renormalization group analysis, they found that the non-perturbative function can be generally written as

$$\bar{W}_{j\bar{k}}^{NP}(b, Q, Q_0, x_1, x_2) = \exp \left[-F_1(b) \ln\left(\frac{Q^2}{Q_0^2}\right) - F_{j/h_1}(x_1, b) - F_{\bar{k}/h_2}(x_2, b) \right], \quad (11)$$

where F_1 , F_{j/h_1} and $F_{\bar{k}/h_2}$ must be extracted from data with the constraint that

$$\bar{W}_{j\bar{k}}^{NP}(b=0) = 1.$$

Furthermore, the F_1 term only depends on Q , while F_{j/h_1} and $F_{\bar{k}/h_2}$ in general depend on x_1 or x_2 , and their values can depend on the flavor of the initial state partons (j and \bar{k} in this case). Later, in Ref. [13], it was shown that the $F_1(b) \ln(Q^2/Q_0^2)$ dependence is also suggested by infrared renormalon contributions to the Q_T distribution.

B. Testing the universality of $\bar{W}_{j\bar{k}}^{NP}$

The CSS resummation formalism suggests that the non-perturbative function should be universal.¹ Its role is analogous to that of the parton distribution function (PDF) in any

¹Here we mean "universal" within the context of Drell-Yan processes, although it may apply in general to other reactions having the same initial or final state particles as in the Drell-Yan process.

fixed order perturbative calculation, as its value must be determined from data. The first attempt to determine such a universal non-perturbative function was made by Davies, Webber and Stirling (DWS) [14] in 1985 who fit data available at that time to the resummed piece (the $\bar{W}_{j\bar{k}}$ term) using the Duke and Owens parton distribution functions [15]. Subsequently, the DWS results were combined with a next-to-leading order (NLO) calculation [16] by Arnold and Kauffman [7] in 1991 to provide the first complete CSS prediction relevant to hadron collider Drell-Yan data. In 1994, Ladinisky and Yuan (LY) [17] observed that the prediction of the DWS set of $\bar{W}_{j\bar{k}}^{NP}$ deviates from R209 data ($p+p \rightarrow \mu^+\mu^- + X$ at $\sqrt{S}=62$ GeV) using the CTEQ2M PDF [18]. In order to incorporate possible $\ln(\tau)$ dependence, LY postulated a model for the non-perturbative term, which was different from that of DWS, as

$$\bar{W}_{j\bar{k}}^{NP}(b, Q, Q_0, x_1, x_2) = \exp \left[-g_1 b^2 - g_2 b^2 \ln \left(\frac{Q}{2Q_0} \right) - g_3 b \ln(100x_1 x_2) \right], \quad (12)$$

where $x_1 x_2 = \tau$. A “two-stage fit” of the R209, Collider Detector at Fermilab (CDF) Z (4 pb⁻¹ data) and E288 ($p + \text{Cu}$) data gave [17]

$$g_1 = 0.11_{-0.03}^{+0.04} \text{ GeV}^2, \quad g_2 = 0.58_{-0.2}^{+0.1} \text{ GeV}^2, \\ g_3 = -1.5_{-0.1}^{+0.1} \text{ GeV}^{-1},$$

for $Q_0 = 1.6$ GeV and $b_{\text{max}} = 0.5 \text{ GeV}^{-1}$.² The purpose of the project described here is twofold: First, we update fits for the non-perturbative parameters using modern, high-statistics samples of low energy Drell-Yan data and second we incorporate a fitting technique which will track the full error matrix for all fitted parameters. In a subsequent report we will update these results for the full Tevatron run I datasets [19]. Our results are given in the following sections.

III. FITTING PROCEDURE

A. Choice of the parametrization form

At the present time, the non-perturbative functions in the CSS resummation formalism cannot be derived from QCD theory, so a variety of functional forms should be studied. The only necessary condition is that $\bar{W}_{j\bar{k}}^{NP}(b=0)=1$. For simplicity, we consider only two typical functional forms for $\bar{W}_{j\bar{k}}^{NP}(b, Q, Q_0, x_1, x_2)$ in b space: (i) 2-parameter pure Gaussian form [DWS form],

$$\exp \left[-g_1 - g_2 \ln \left(\frac{Q}{2Q_0} \right) \right] b^2 \quad (13)$$

²A FORTRAN coding error in calculating the parton densities of the neutron led to an incorrect value for g_3 .

TABLE I. Drell-Yan data used in this analysis. Here, δN is the published normalization uncertainty for each experiment. The CDF data were from Tevatron collider run 0 of 4 pb⁻¹.

Experiment	Ref.	Reaction	\sqrt{S} GeV	$\langle \sqrt{\tau} \rangle$	δN
R209	[23]	$p+p \rightarrow \mu^+\mu^- + X$	62	~ 0.1	10%
E605	[24]	$p+\text{Cu} \rightarrow \mu^+\mu^- + X$	38.8	~ 0.2	15%
CDF-Z	[25]	$p+\bar{p} \rightarrow Z + X$	1800	~ 0.05	—
E288	[26]	$p+\text{Cu} \rightarrow \mu^+\mu^- + X$	27.4	~ 0.2	25%

and (ii) a 3-parameter form [LY form],

$$\exp \left[\left[-g_1 - g_2 \ln \left(\frac{Q}{2Q_0} \right) \right] b^2 - [g_3 \ln(100x_1 x_2)] b \right], \quad (14)$$

with a logarithmic x -dependent third term which is linear in b . The $\ln(100x_1 x_2)$ term is equivalent to $\ln(\tau/\tau_0)$ for $\sqrt{\tau_0} = 0.1$.

Both forms assume no flavor dependence for simplicity. In addition to fitting for the non-perturbative parameters, g_1 , g_2 , and g_3 , the overall normalizations were allowed to float for some fits. One can also study another pure Gaussian form with similar x dependence such as

$$\exp \left[-g_1 - g_2 \ln \left(\frac{Q}{2Q_0} \right) - g_3 \ln(100x_1 x_2) \right] b^2.$$

However, we find that current data are not yet precise enough to clearly separate the g_2 and g_3 parameters within this functional form and so it will not be discussed further in this paper. We also tested a few additional functions which did not incorporate additional parameters, but did not find any clear advantage to them when fitting the current Drell-Yan data. However, as to be shown later, the run 1 W/Z data at the Tevatron are expected to determine the g_2 coefficient with good accuracy, and these data can be combined with the low energy Drell-Yan data to further test various scenarios for x dependence and ultimately, universality.

B. Choice of the data sets

In order to determine the non-perturbative functions discussed above, we need to choose experimental data sets for which the contribution to the non-perturbative piece dominates the transverse momentum distributions. This suggests using low energy fixed target or collider data in which the transverse momentum (Q_T) of the Drell-Yan pair is much less than its invariant mass (Q). Because the CSS resummation formalism better describes data in which the Drell-Yan pairs are produced in the central rapidity region (as defined in the center-of-mass frame of the initial state hadrons) we shall concentrate on data with those properties. Based upon the above criteria we chose to consider data shown in Table I. We have also examined the E772 data [20], from the process $p+H^2 \rightarrow \mu^+\mu^- + X$ at $\sqrt{S}=56.6$ GeV, and found that it was not compatible in our fits with the above data, and it is

not included in this study.³ Except where noted, all of the fits to $g_{1,2,3}$ were done using the CTEQ3M PDF [22] fits.

C. Primary fits

As to be shown later, the E288 data have the smallest errors, and would be expected to dominate the result of a global fit. That is indeed the case. When including the E288 data in a global fit, we found that the resulting fit required the NORM⁴ to be too large (as compared to the experimental systematic error) for either the E288 or the E605 data. Furthermore, the shape of the R209 data cannot be well described by the theory prediction based on such a fit.

1. Fits $A_{2,3}$

As explained above, a straightforward global fit (that is, one which includes all of the available data) does not give a satisfactory χ^2 due to the large systematic uncertainties. We therefore employed a different strategy for the global fit based on the statistical quality of the data. We included the first two mass bins ($7 < Q < 8$ GeV and $8 < Q < 9$ GeV) of the E605 data, all but the highest mass bin of the R209 results, and all of the early CDF-Z boson data in an initial global fit, referred to here as Fit $A_{2,3}$ (see Figs. 1, 2, and 3). In total, 31 data points were considered. We allowed the normalization of the R209 and E605 data to float within their overall systematic normalization errors, while fixing the normalization of the CDF-Z data to unity. (The point-to-point systematic error of 10% for the E605 data has also been included in the error bars of the data points shown in Fig. 3.) In addition to the normalization factor for each experiment, the fitted parameters of our global fit include the coefficients $g_{1,2}$ and $g_{1,2,3}$ for the 2-parameter and 3-parameter fits, respectively. We found that, for $Q_0 = 1.6$ GeV and $b_{max} = 1/(2 \text{ GeV})$, both the 2-parameter and the 3-parameter forms give good fits, with χ^2 per degree of freedom about equal to 1.4.⁵ The best fitted central values for Fit A_2 are: $g_1 = 0.24 \text{ GeV}^2$, $g_2 = 0.34 \text{ GeV}^2$. While the central values for Fit A_3 are $g_1 = 0.15 \text{ GeV}^2$, $g_2 = 0.48 \text{ GeV}^2$, $g_3 = -0.58 \text{ GeV}^{-1}$. The fitted values for the R209 NORM are 1.04 for both Fits A_2 and A_3 .

2. Uncertainties in the fits

We have also studied the uncertainties of the fitted g parameters. For the 2-parameter fit, the 1σ error in the χ^2 plot (with an approximately elliptical contour) gives $-0.07 < \delta g_1 < 0.08 \text{ GeV}^2$ and $-0.08 < \delta g_2 < 0.07 \text{ GeV}^2$. This is shown in Fig. 4. For the 3-parameter fit, the situation is more

³Using the fitted g values to be given below, the theory prediction for the E772 experiment is typically a factor of 2 smaller than the data. Similarly, CTEQ fitting of PDF parameters are not well fit with these data [21].

⁴Here, and in subsequent discussions, the quantity NORM is the fitted normalization factor which is applied to the prediction curves in all that follow: the data are uncorrected.

⁵We scan the values of g_1 and g_2 between 0 and 1, and g_3 between -2 and 3 .

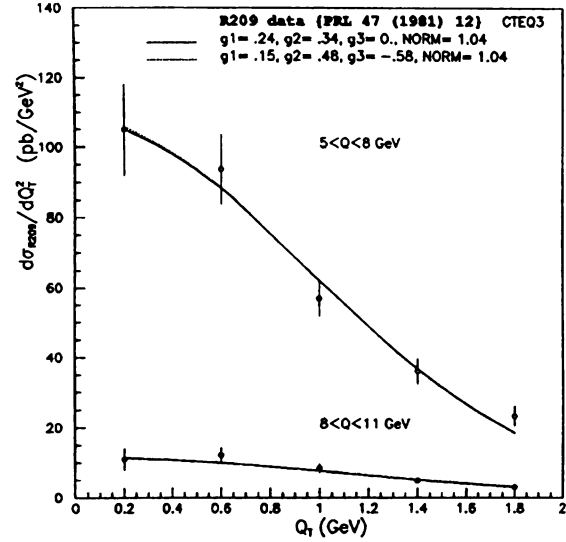


FIG. 1. R209 data, from $p + p \rightarrow \mu^+ \mu^- + X$ at $\sqrt{s} = 62$ GeV, with an overall systematic normalization error of 10%. The curves are the results of Fits A_2 and A_3 and are multiplied by the value of NORM, as shown in the figure and described in the text.

complicated, as the fitted values of g 's are highly correlated as shown in Fig. 5. In order to estimate the uncertainties of the fitted g values, we fix the value (at its best fit value) of g 's, one at a time, and examine the uncertainties of the other two, in a way similar to studying the 2-parameter fit result. We found that

$$g_1 \text{ fixed: } -0.05 < \delta g_2 < +0.04 \text{ GeV}^2,$$

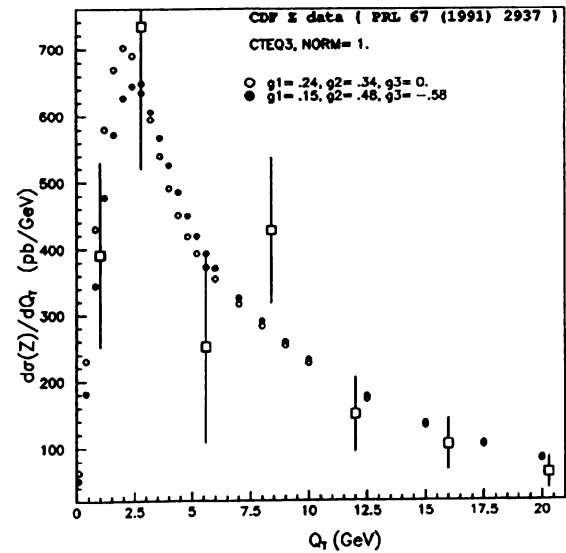


FIG. 2. Comparison of 4 pb^{-1} CDF-Z data at the Tevatron with two different theory model predictions. The dots correspond to the results of Fits A_2 and A_3 .

1000
1000
1000

1000
1000
1000

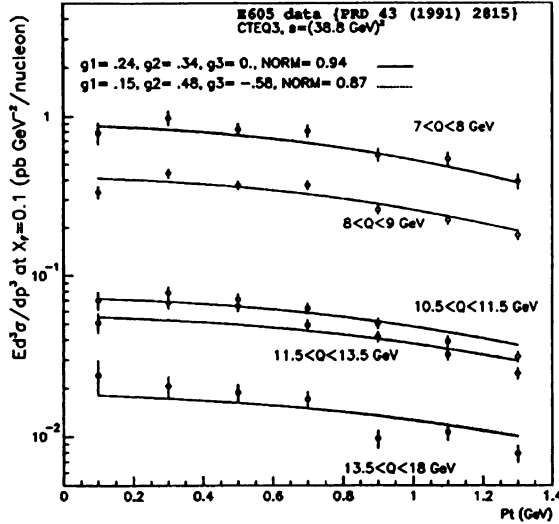


FIG. 3. E605 data, from $p + \text{Cu} \rightarrow \mu^+ \mu^- + X$ at $\sqrt{s} = 38.8$ GeV, with an overall systematic normalization error of 15%. The curves are the results of Fits A_2 and A_3 and are multiplied by the value of NORM, as shown in the figure and described in the text.

$$-0.20 < \delta g_3 < +0.26 \text{ GeV}^{-1};$$

$$g_2 \text{ fixed: } -0.03 < \delta g_1 < +0.03 \text{ GeV}^2,$$

$$-0.11 < \delta g_3 < +0.11 \text{ GeV}^{-1};$$

$$g_3 \text{ fixed: } -0.02 < \delta g_1 < +0.04 \text{ GeV}^2,$$

$$-0.03 < \delta g_2 < +0.02 \text{ GeV}^2;$$

constitute a conservative set of uncertainty ranges. With an appreciation for the complexity discussed above, we characterize the uncertainties of the fitted g 's in the 3-parameter form conservatively by their maximal deviations among all of the fixed parameter choices just described. Therefore, the best fitted g values are:

$$\text{Fit } A_2: g_1 = 0.24_{-0.07}^{+0.08} \text{ GeV}^2, \quad g_2 = 0.34_{-0.08}^{+0.07} \text{ GeV}^2;$$

$$\text{Fit } A_3: g_1 = 0.15_{-0.03}^{+0.04} \text{ GeV}^2, \quad g_2 = 0.48_{-0.05}^{+0.04} \text{ GeV}^2,$$

$$g_3 = -0.58_{-0.20}^{+0.26} \text{ GeV}^{-1};$$

for the 2 and 3 parameter fits, respectively. In summary, fits A_2 and A_3 constitute the main results of this paper. The g_1 and g_2 parameter spaces of the above two fits do not strongly overlap because the g parameters are found to be highly correlated.

3. Cross checks

Given these values of g 's and the fitted normalization factors for the E605 data, we can calculate the two different predictions for the other three high mass bins not used in Fits

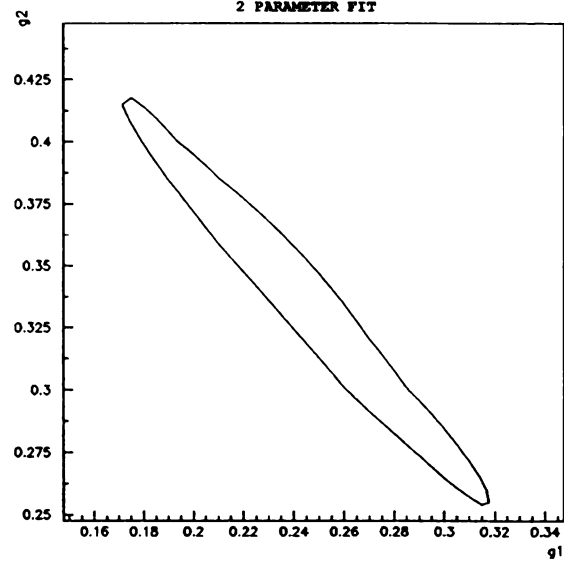


FIG. 4. The error ellipse on the g_1 and g_2 plane from which the errors of the 2-parameter fit A_2 were interpreted.

$A_{2,3}$, and the results are also shown in Fig. 3. In order to compare with the E288 data, we created Fits $N_{2,3}$ in which we fix the g 's to those obtained from Fits $A_{2,3}$ and fit for NORM from the E288 data alone. Figure 6 shows the resulting fits are acceptable, with values of NORM close to the quoted 25%, namely, NORM=0.92 and 0.79 for Fits $N_{2,3}$, respectively. It is encouraging that the quality of the fit for the E288 results is very similar to that for the E605 data and that the normalizations are now acceptably within the range quoted by the experiment. Hence, we conclude that the fitted values of g 's reasonably describe the wide-ranging, complete set of data, as discussed above.

We note that although the CDF-Z data, as shown in Fig. 2, contain only 7 data points with large statistical uncertainties, they prove to be very useful in determining the value of g_2 . To test this observation, we performed an additional fit, L_2 . Following the method suggested in [17], we set g_3 to be zero and fit the g_1 and g_2 parameters using the R209 and CDF-Z data alone. (Note that for the R209 data, the typical value of $\sqrt{\tau}$ is of the order 0.1, which motivates the choice of $\sqrt{\tau_0} = 0.1$ in the LY form. Effectively, the g_3 contribution to the R209 data can be ignored.) We found that the best fit⁶ gives $g_2 = 0.47 \text{ GeV}^2$, which is in good agreement with the result of the global Fit A_3 discussed above. Hence, we conclude that the CDF-Z data already play an important role in constraining the g_2 parameter, which can be further improved with large Z data samples from run 1 of the Tevatron collider experiments. We shall defer its discussion to the next section.

⁶Also, $g_1 = 0.18 \text{ GeV}^2$.

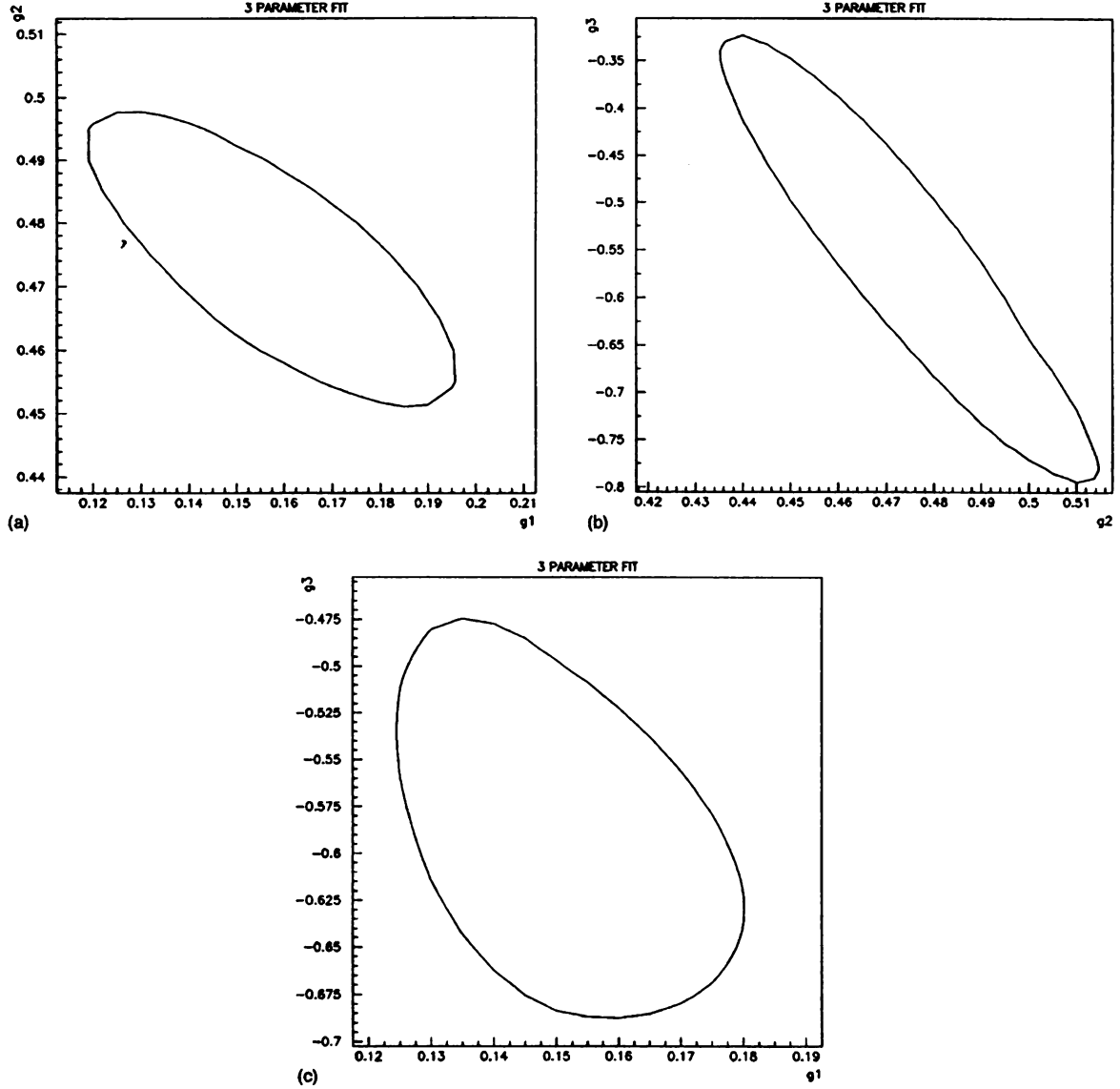


FIG. 5. The error ellipse projections from which the errors of the 3-parameter fit A_3 were interpreted. (a) g_1 and g_2 plane, (b) g_2 and g_3 plane, and (c) g_1 and g_3 plane.

IV. RUN 1 W AND Z BOSON DATA AT THE TEVATRON

The run 1 W and Z boson data at the Tevatron can be useful as a test of universality and the x dependence of the non-perturbative function $\bar{W}_{jk}^{NP}(b, Q, Q_0, x_1, x_2)$. This is clearly demonstrated in Fig. 2, where we give the predictions for the two different global fits (2-parameter and 3-parameter fits) obtained in the previous section using the CTEQ3M PDF parametrizations. (The CTEQ4M PDF [27] gives similar results.) With the large Z boson data sets anticipated from Tevatron run 1 (1a and 1b), it should be possible to distinguish these two example models.

As shown in Ref. [9], for $Q_T > 10$ GeV the non-perturbative function has little effect on the Q_T distribution, although in principle it affects the whole Q_T range (up to $Q_T \sim Q$). In order to study the resolving power of the full Tevatron run 1 Z boson data in determining the non-perturbative function, we have performed a “toy global fit,” Fit F_3 as follows. First, we generate a set of fake run 1 Z boson data (assuming 5,500 reconstructed Z bosons in 24 Q_T bins between $Q_T = 0$ and 20 GeV/c) using the original LY fit results ($g_1 = 0.11$ GeV², $g_2 = 0.58$ GeV² and $g_3 = -1.5$ GeV⁻¹). Then, we combine these fake-Z boson data with the R209 and E605 Drell-Yan data as discussed above to per-

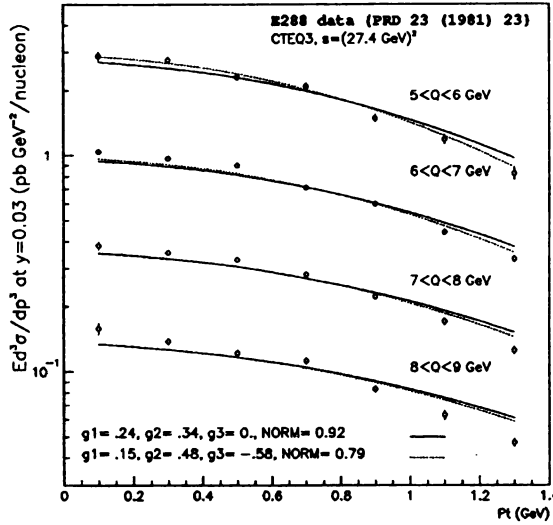


FIG. 6. E288 data, from $p + \text{Cu} \rightarrow \mu^+ \mu^- + X$ at $\sqrt{s} = 27.4$ GeV, with an overall systematic normalization error of 25%. The curves are the results of Fits N_2 and N_3 and are multiplied by the value of NORM, as shown in the figure and described in the text.

form a global fit. The 3-parameter form results in

$$\text{Fit } F_3: g_1 = 0.10^{+0.02}_{-0.02} \text{ GeV}^2, \quad g_2 = 0.57^{+0.01}_{-0.02} \text{ GeV}^2, \\ g_3 = -0.98^{+0.15}_{-0.17} \text{ GeV}^{-1},$$

with a χ^2 per degree of freedom of approximately 1.3.⁷ These fitted values for the g 's agree perfectly with those used to generate the fake-Z data except for the value of g_3 , which is smaller by a factor of 2. It is interesting to note that this result agrees within 2σ with that of Fit A_3 , using only the current low energy data, although the uncertainties on g 's are smaller by a factor of 2.

We have also performed the same fit for the 2-parameter form and obtained an equally good fit with

$$\text{Fit } F_2: g_1 = 0.04^{+0.03}_{-0.03} \text{ GeV}^2, \quad g_2 = 0.63^{+0.04}_{-0.03} \text{ GeV}^2.$$

While the new g_2 value (0.63 GeV^2) obtained in Fit F_2 is very different from that of A_2 (0.34 GeV^2) given in the previous section, it is actually in good agreement with the g_2 value (0.57 GeV^2) obtained from Fit A_3 . This implies that the run 1 Z boson data, when combined with the low energy Drell-Yan data, can be extremely useful in determining the parameter g_2 . In Figs. 7–10, we compare the two theory predictions (derived from $F_{2,3}$) with the R209, fake-Z, E605, and E288 data. As shown, they both agree well with all of the data.

⁷This amounts to a shift in the prediction for the mass and the width of the W boson by about 5 MeV and 10 MeV, respectively [28].

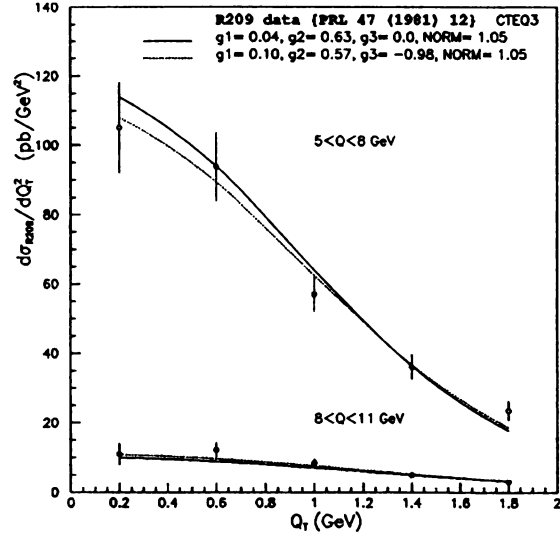


FIG. 7. Comparison of R209 data with two different theory model predictions obtained from the "toy global fit." The curves are the results of Fits F_2 and F_3 and are multiplied by the value of NORM, as shown in the figure and described in the text.

Before closing this section, we would like to comment on the result of a single parameter study of the fake Z data, Fit S_1 . Given the large sample of run 1 Z data, one can consider fitting the non-perturbative function with only one, Q -independent, non-perturbative parameter. With this in mind, we fitted the fake Z data with the non-perturbative function

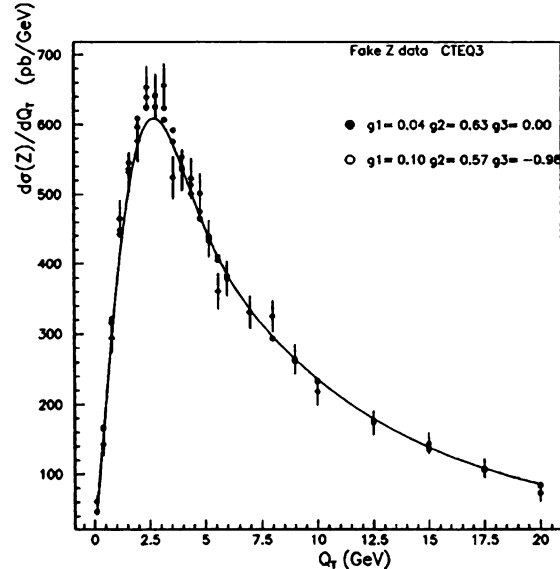


FIG. 8. Comparison of "fake Z" data (solid curve) with two different theory model predictions (dots) obtained from the "toy global fits" F_2 and F_3 .

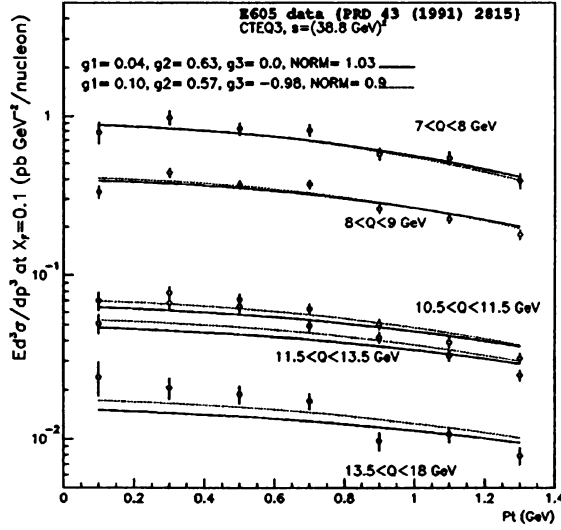


FIG. 9. Comparison of E605 data with two different theory model predictions obtained from the “toy global fit.” The curves are the results of Fits F_2 and F_3 and are multiplied by the value of NORM, as shown in the figure and described in the text.

$$\bar{W}_{jk}^{NP}(b, Q, Q_0, x_1, x_2) = \exp[-\bar{g}_1 b^2], \quad (15)$$

and found that

$$\text{Fit } S_1: \bar{g}_1 = 2.1_{-0.08}^{+0.09} \text{ GeV}^2,$$

which gives a good description of the Q_T distribution of the “fake-Z” data. It is easy to see that this fitted value agrees

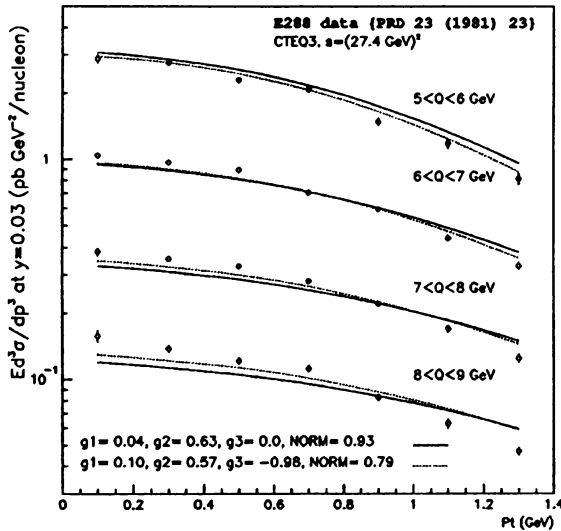


FIG. 10. Comparison of E288 data with two different theory model predictions obtained from the “toy global fit.” The curves are the results of Fits F_2 and F_3 and are multiplied by the value of NORM, as shown in the figure and described in the text.

with that of the 2-parameter fit just by considering the coefficient of b^2 in first two terms of Eq. (14). For the results of F_2 with the value of the Z boson mass, $M_Z = 91.187 \text{ GeV}/c^2$, we obtain $0.04 + 0.63 \ln(M_Z/2Q_0) = 2.14$, which is essentially the same as the coefficient of b^2 in S_1 . One interesting question is whether the result of this one-parameter fit alone can be used to also describe the Q_T distribution of the W^\pm boson produced at the Tevatron (at the same energy). A quantitative estimate can be easily obtained by noting again that the difference between $0.04 + 0.63 \ln(M_Z/2Q_0) = 2.14$ and $0.04 + 0.63 \ln(M_W/2Q_0) = 2.06$ with the W-boson mass $M_W = 80.3 \text{ GeV}/c^2$, is 0.08, which are essentially the same, given the uncertainty of 0.09 GeV^2 from S_1 . We conclude that it is indeed a good approximation to use the one-parameter fit result from fitting Z boson data in order to predict the Q_T distribution of the W^\pm boson using the CSS resummation formalism. On the other hand, a single parameter without Q dependence (i.e. the parameter \bar{g}_1 alone) does not give a reasonable global fit to all of the Drell-Yan data discussed above. For instance, for the R209 data, the 2-parameter fit gives $0.04 + 0.63 \ln(8/2Q_0) = 0.6$ for the coefficient of Eq. (13), which is not consistent with the value of \bar{g}_1 from S_1 . Hence, we conclude that in order to test the universality of the non-perturbative function of the CSS formalism, one must consider its functional form with Q (and x) dependence.

V. CONCLUSIONS

The effects of QCD gluon resummation are important in many precision measurements. In order to make predictions using the CSS resummation formalism for the Q_T distributions of vector bosons at hadron colliders, it is necessary to include contributions from the phenomenological non-perturbative functions inherent to the formalism. In this paper, we have extended previous results by making use of 2-parameter and the 3-parameter fits to modern, low energy Drell-Yan data. We found that both parametrizations result in good fits. In particular our results are

$$\text{Fit } A_2: g_1 = 0.24_{-0.07}^{+0.08} \text{ GeV}^2, \quad g_2 = 0.34_{-0.08}^{+0.07} \text{ GeV}^2.$$

$$\text{Fit } A_3: g_1 = 0.15_{-0.03}^{+0.04} \text{ GeV}^2, \quad g_2 = 0.48_{-0.05}^{+0.04} \text{ GeV}^2,$$

$$g_3 = -0.58_{-0.20}^{+0.26} \text{ GeV}^{-1}.$$

Each functional form predicts measurably different Q_T distributions for Z bosons produced at the Fermilab Tevatron. We showed that the full Tevatron run 1 Z boson data can potentially distinguish these two different models. Table II summarizes all of the fits described in this paper.

In particular, using the results from a toy global fit, we concluded that the large sample of the run 1 Z data can help to determine the value of g_2 , which is the coefficient of the $\ln(Q/2Q_0)$ term. Work to incorporate the full run I data is in progress [19]. Given these new data, one can hope to study the x dependence of the non-perturbative function in more detail. We also confirmed that it is reasonable to use a single non-perturbative parameter \bar{g}_1 to fit Z boson data, and use

TABLE II. Summary of the results of all fits described in this paper. The last column denotes the figure numbers in which the results are displayed.

Fit	Contents	Label	Results	Figure
$A_{2,3}$	full 2 and 3 parameter global fit	A_2	$g_1 = 0.24^{+0.08}_{-0.07} \text{ GeV}^2$	1,2,3,4,5
			$g_2 = 0.34^{+0.07}_{-0.08} \text{ GeV}^2$	
		A_3	$g_1 = 0.15^{+0.04}_{-0.03} \text{ GeV}^2$	
			$g_2 = 0.48^{+0.04}_{-0.05} \text{ GeV}^2$	
L_2	$g_3 = 0$ R209 plus CDF	L_2	$g_3 = -0.58^{+0.26}_{-0.20} \text{ GeV}^{-1}$	
			$g_1 = 0.18 \text{ GeV}^2$	
$N_{2,3}$	fix g 's to $A_{2,3}$ fit NORM from E288	N_2	$g_2 = 0.47 \text{ GeV}^2$	6
		N_3	NORM=0.92	
$F_{2,3}$	g 's from LY to generate fake Z data plus R209 and E605	F_2	NORM=0.79	7,8,9,10
			$g_1 = 0.04^{+0.03}_{-0.03} \text{ GeV}^2$	
			$g_2 = 0.63^{+0.04}_{-0.03} \text{ GeV}^2$	
		F_3	$g_1 = 0.10^{+0.02}_{-0.02} \text{ GeV}^2$	
S_1	fake Z data	S_1	$g_2 = 0.57^{+0.01}_{-0.02} \text{ GeV}^2$	
			$g_3 = -0.98^{+0.15}_{-0.17} \text{ GeV}^{-1}$	
			$\bar{g}_1 = 2.1^{+0.09}_{-0.08} \text{ GeV}^2$	

that result to study the Q_T distribution of the W^\pm boson for $Q_T < 10 \text{ GeV}$. Recently this point has been made in the context of a momentum-space fit [5] using a single parameter. Such an approach might indeed alleviate the computational overhead required in order to generate complete $y - Q_T$ grids of simulated W bosons necessary for M_W analyses. However, if one is interested in testing the universality property of the CSS resummation formalism or making predictions about W and Z boson production at future colliders, such as the CERN

Large Hadron Collider, then one must include the Q (and, possibly, x) dependent term in the non-perturbative function.

ACKNOWLEDGMENTS

We thank C. Balázs, D. Casey, J. Collins, W.-K. Tung and the CTEQ Collaboration for useful discussions. This work was supported in part by National Science Foundation grants PHY-9514180 and PHY-9802564.

- [1] Y.L. Dokshitzer, D.I. Diakonov, and S.I. Troian, Phys. Lett. **79B**, 269 (1978); Phys. Rep. **58**, 269 (1980).
- [2] G. Parisi and R. Petronzio, Nucl. Phys. **B154**, 427 (1979).
- [3] J. Collins and D. Soper, Nucl. Phys. **B193**, 381 (1981); **B213**, 545(E) (1983); **B197**, 446 (1982).
- [4] R.K. Ellis, G. Martinelli, and R. Petronzio, Phys. Lett. **104B**, 45 (1981); Nucl. Phys. **B211**, 106 (1983); G. Altarelli, R.K. Ellis, M. Greco, and G. Martinelli, *ibid.* **B246**, 12 (1984).
- [5] R.K. Ellis and S. Veseli, Nucl. Phys. **B511**, 649 (1998).
- [6] J. Collins, D. Soper, and G. Sterman, Nucl. Phys. **B250**, 199 (1985).
- [7] P.B. Arnold and R.P. Kauffman, Nucl. Phys. **B349**, 381 (1991).
- [8] C. Balázs, J.W. Qiu, and C.-P. Yuan, Phys. Lett. B **355**, 548 (1995).
- [9] C. Balázs and C.-P. Yuan, Phys. Rev. D **56**, 5558 (1997), and the references therein.
- [10] R.K. Ellis, D.A. Ross, and S. Veseli, Nucl. Phys. **B503**, 309 (1997).
- [11] C. Balázs, E.L. Berger, S. Mrenna, and C.-P. Yuan, Phys. Rev. D **57**, 6934 (1998); C. Balázs and C.-P. Yuan, *ibid.* **59**, 114007 (1999).
- [12] S. Catani, E. D'Emilio, and L. Trentadue, Phys. Lett. B **211**, 335 (1988); I. Hinchliffe and S.F. Novaes, Phys. Rev. D **38**, 3475 (1988); R.P. Kauffman, *ibid.* **44**, 1415 (1991); C.-P. Yuan, Phys. Lett. B **283**, 395 (1992).
- [13] G.P. Korchemsky and G. Sterman, Nucl. Phys. **B437**, 415 (1995).
- [14] C. Davies, B. Webber, and W. Stirling, Nucl. Phys. **B256**, 413 (1985).
- [15] D.W. Duke and J.F. Owens, Phys. Rev. D **30**, 49 (1984).
- [16] P. Arnold and M.H. Reno, Nucl. Phys. **B319**, 37 (1989); **B330**, 284(E) (1990); P. Arnold, R.K. Ellis, and M.H. Reno, Phys. Rev. D **40**, 912 (1989).
- [17] G.A. Ladinsky and C.-P. Yuan, Phys. Rev. D **50**, 4239 (1994). These fits were not a full, three parameter global fit for the non-perturbative parameters. Rather, they were the result of successive fits in which some parameters were held constant for particular sets of data considered.
- [18] J. Botts, J. Huston, H. Lai, J. Morfin, J. Owens, J. Qiu, W.-K. Tung, and H. Weerts, Michigan State University Report No. MSUTH-93/17.
- [19] F. Landry, Ph.D. thesis (in preparation).
- [20] P.L. McGaughey *et al.*, Phys. Rev. D **50**, 3038 (1994).
- [21] W.-K. Tung (private communication).
- [22] H.L. Lai, J. Botts, J. Huston, J.G. Morfin, J.F. Owens, J.W. Qiu, W.K. Tung, and H. Weerts, Phys. Rev. D **51**, 4763 (1995).



- [23] J. Paradiso, Ph.D. thesis, Massachusetts Institute of Technology, 1981; D. Antreasyan *et al.*, Phys. Rev. Lett. 47, 12 (1981).
- [24] G. Moreno *et al.*, Phys. Rev. D 43, 2815 (1991).
- [25] F. Abe *et al.*, Phys. Rev. Lett. 67, 2937 (1991); J.S.T. Ng, Ph.D. thesis, 1991, Harvard University Report No. HUHEPL-12.
- [26] A.S. Ito *et al.*, Phys. Rev. D 23, 604 (1981).
- [27] H.L. Lai, J. Huston, S. Kuhlmann, F. Olness, J. Owens, D. Soper, W.K. Tung, and H. Weerts, Phys. Rev. D 55, 1280 (1997).
- [28] E. Flattum, Ph.D. thesis, Michigan State University, 1996; and presentation to the Precision Measurements Subgroup of the Fermilab QCD and Weak Bosons Workshop, 1999; B. Ashmanskas, presentation to the Precision Measurements Subgroup of the Fermilab QCD and Weak Bosons Workshop, 1999.



BIBLIOGRAPHY



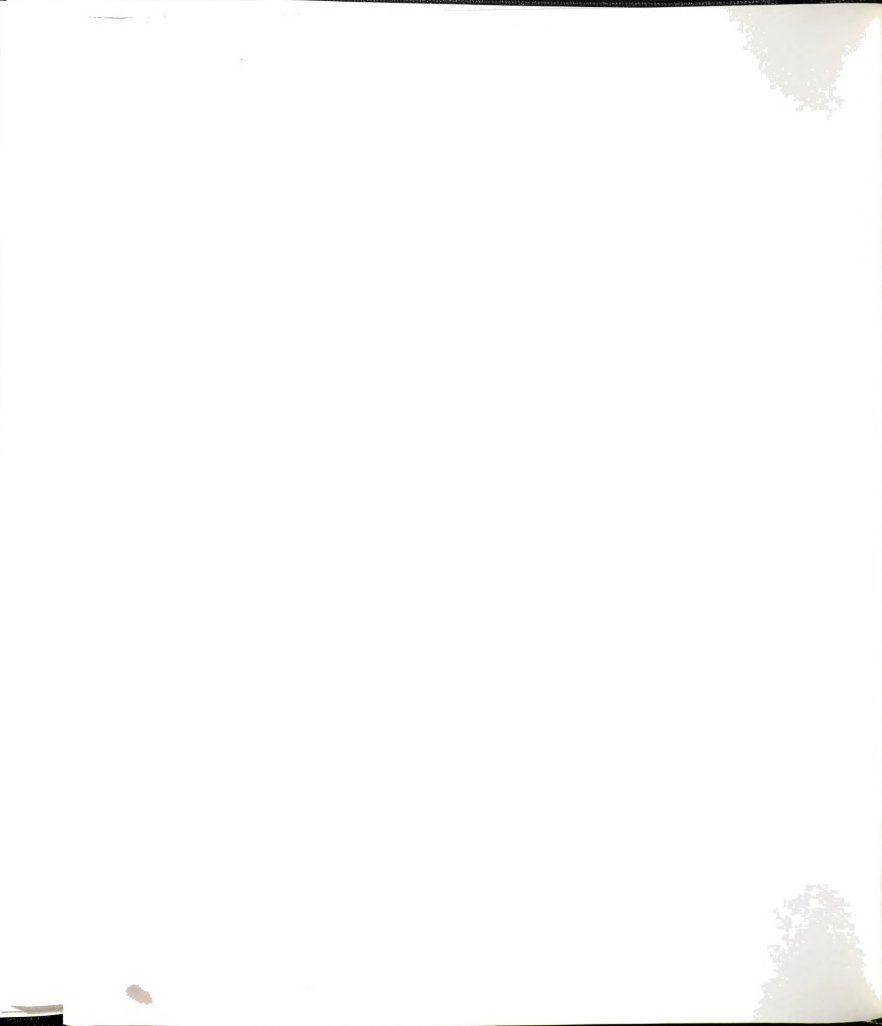
BIBLIOGRAPHY

- [1] C. Caso et al, The European Physical Journal **C3** 1 (1998); [Online] Available <http://pdg.lbl.gov/>.
- [2] S. Weinberg, *Phys. Rev. Lett.* **19** 1264 (1967); S.L. Glashow, *Nucl. Phys.* **22** 579 (1968); A. Salam, in *Elementary Particle Theory*, ed. by N. Svartholm (Almqvist and Wiksell, Sweden, 1968), p. 367; S.L. Glashow, J. Illiopoulos and L. Maiani, *Phys. Rev.* **D2** 1285 (1970).
- [3] G. Arnison et al., *Phys. Lett.* **B122** 103 (1983).
- [4] G. Arnison et al., *Phys. Lett.* **B126** 398 (1983).
- [5] R. Brock, Lecture given August 1999 at MSU.
- [6] R. Brock, Lecture given in 1997 at CTEQ QCD Summer School.
- [7] R. D. Field, *Applications of Perturbative QCD*, Addison-Wesley, 1989.
- [8] S. D. Drell and T. M. Yan, *Phys. Rev. Lett.* **25** 316 (1970).
- [9] B. Pope, *The observation of muon pairs in high energy hadron collisions*, Nevis Laboratories, Columbia Univ., Physics Dept., 1970.
- [10] Y.I. Dokshitser, D.I. D'Yakonov and S.I. Troyan, *Phys. Lett.* **79B** 269 (1978); *Phys. Rep.* **58** 269 (1980).
- [11] G. Parisi, R. Petronzio, *Nucl. Phys.* **B154** 427 (1979).
- [12] J. Collins and D. Soper, *Nucl. Phys.* **B193** 381 (1981); Erratum: **B213** 545 (1983); **B197** 446 (1982); J. Collins, D. Soper, and G. Sterman, *Nucl. Phys.* **B250** 199 (1985).
- [13] R. K. Ellis, G. Martinelli, and R. Petronzio, *Phys. Lett.* **104B** 45 (1981); *Nucl. Phys.* **B211** 106 (1983); G. Altarelli, R. K. Ellis, M. Greco, and G. Martinelli, *ibid.* **B246** 12 (1984).
- [14] R. K. Ellis and S. Veseli, *Nucl. Phys.* **B511** 649 (1998).
- [15] P. B. Arnold and R. P. Kauffman, *Nucl. Phys.* **B349** 381 (1991).
- [16] C. Balázs, J. W. Qiu, and C.-P. Yuan, *Phys. Lett.* **B355** 548 (1995).



- [17] C. Balázs and C.-P. Yuan, *Phys. Rev.* **D56** 5558 (1997).
- [18] R. K. Ellis, D. A. Ross, and S. Veseli, *Nucl. Phys.* **B503** 309 (1997).
- [19] C. Balázs, E. L. Berger, S. Mrenna, and C.-P. Yuan, *Phys. Rev.* **D57** 6934 (1998); C. Balázs and C.-P. Yuan, *ibid.* **59** 114007 (1999).
- [20] S. Catani, E. D’Emilio, and L. Trentadue, *Phys. Lett.* **B211** 335 (1988); I. Hinchliffe and S.F. Novaes, *Phys. Rev.* **D38** 3475 (1988); R.P. Kauffman, *ibid.* **44** 1415 (1991); C.-P. Yuan, *Phys. Lett.* **B283** 395 (1992).
- [21] C. Davies and W. J. Stirling, *Nucl. Phys.* **B244** 337 (1984); C. Davies, B. Webber, and W. J. Stirling, *Nucl. Phys.* **B256** 413 (1985).
- [22] D.W. Duke and J. F. Owens, *Phys. Rev.* **D30** 49 (1984).
- [23] P. Arnold and M. H. Reno, *Nucl. Phys.* **B319** 37 (1989); **B330** 284(E) (1990); P. Arnold, R. K. Ellis, and M. H. Reno, *Phys. Rev.* **D40** 912 (1989).
- [24] G. A. Ladinsky and C.-P. Yuan, *Phys. Rev.* **D50** 4239 (1994).
- [25] [Online] Available http://www.fnal.gov/pub/accel_tour.html; [Online] Available <http://cosmo.fnal.gov/organizationalchart/mcginnis/misc/uw600/default.htm>; [Online] Available <http://www-bd.fnal.gov/public/index.html>.
- [26] S. Abachi et al., *Nucl. Inst. Meth.* **A338** 185-253 (1994).
- [27] D. Casey, Ph.D. thesis, University of Rochester, unpublished (1997).
- [28] E. Flattum, Ph.D. thesis, Michigan State University, unpublished (1996).
- [29] I. Adam, Ph.D. thesis, Columbia University, unpublished (1997).
- [30] MINUIT, Application Software Group, Computing and Networks Division, CERN, Geneva, Switzerland.
- [31] DIVDIF, Application Software Group, Computing and Networks Division, CERN, Geneva, Switzerland.
- [32] J. Paradiso, Ph.D. thesis, Massachusetts Institute of Technology, unpublished (1981); D. Antreasyan, et al., *Phys. Rev. Lett.* **47** 12 (1981).
- [33] J. S. T. Ng, Ph.D. thesis, Harvard University, unpublished (1991); F. Abe, et al., *Phys. Rev. Lett.* **67** 2937 (1991).
- [34] T. Affolder, et al., *Phys. Rev. Lett.* **84** 845-850 (2000).
- [35] A. S. Ito, et al., *Phys. Rev.* **D23** 604 (1981).
- [36] G. Moreno, Ph.D. thesis, CINVESTAV, Mexico, unpublished (1989); G. Moreno, et al., *Phys. Rev.* **D43** 2815 (1991).

- [37] F. Landry, R. Brock, G. Ladinsky, and C.-P. Yuan, *Phys. Rev.* **D63** 013004 (2001).
- [38] J. Botts, et al., Michigan State University Report No. MSUTH-93/17.
- [39] H.L. Lai, et al., *Phys. Rev.* **D51**, 4763 (1995).
- [40] C.-P. Yuan, private communication.
- [41] D. Soper and J. Collins, "Issues in the Determination of Parton Distribution Functions," CTEQ Note 94/01, hep-ph/9411214.
- [42] J. Pumplin, D. R. Stump, and W. K. Tung, "Multivariate Fitting and the Error Matrix in Global Analysis of Data," Michigan State University Report No. MSU-HEP-07100, CERN Report No. CERN-TH/2000-249.
- [43] R. Brock, et al., "Uncertainties of Parton Distribution Functions and Their Implications on Physical Predictions," Contribution to Proceedings of Fermilab Workshop on QCD and Weak Boson Physics at the Tevatron: Run II and Beyond, Fermilab, 1999.
- [44] R. Brock, private communication.
- [45] P. Laurens and S. Kloczek, "The Level 1 Trigger Monitor Program," DØ internal document.
- [46] H. Johari, et al., "Muon Chamber Alignment," DØ Internal Note #2279.
- [47] S. Feher, et al., "Z Calibration Detector Proposal," DØ Internal Note #2667.
- [48] H. Mao, et al., "ZCD Data Analysis and CDC Z Bias Correction," DØ Internal Note #3140.
- [49] S. Feher, et al., "Axial Calibration of the DØ Central Drift Chamber," DØ Internal Note #3234.





MICHIGAN STATE UNIVERSITY LIBRARIES



3 1293 02125 9183